Title

Estimation and incorporation of organ-specific biomechanical information into radiotherapy treatment planning

Author

Hasse, Katelyn

Publication Date

2018

UNIVERSITY OF CALIFORNIA

Los Angeles

Estimation and incorporation of organ-specific biomechanical information into radiotherapy treatment planning

A dissertation submitted in partial satisfaction of the
requirements for the degree Doctor of Philosophy
in Biomedical Physics

by

Katelyn Elizabeth Hasse

2018

ABSTRACT OF THE DISSERTATION

Estimation and incorporation of organ-specific biomechanical information into radiotherapy treatment planning

by

Katelyn Elizabeth Hasse
Doctor of Philosophy in Biomedical Physics
University of California, Los Angeles, 2018
Professor Daniel Abraham Low, Chair

Radiotherapy is used to treat many cancers of the lung, liver, breast, and other anatomies. The goal of radiotherapy is to deliver high radiation doses to the target while sparing adjacent organs at risk. Accurate target definition is fundamental to ensuring a good outcome. Currently, only geometrical and anatomical information are acquired for purposes of target definition in radiotherapy treatment planning. Functional imaging techniques can provide additional biological information about tumors and the surrounding organs that is often complementary to the information provided by anatomic imaging. While useful, common functional imaging modalities are not generally employed within the radiotherapy workflow, which inhibits their integration into radiotherapy treatment planning.

Tissue biomechanical properties, such as elasticity, have been correlated to underlying tissue function. Towards this goal, a reliable elasticity estimation methodology, or elastography

approach, was formulated for obtaining organ-specific tissue elasticity using images acquired within the current radiotherapy workflow. The feasibility and accuracy of this methodology was verified for breast, liver, and lung anatomies. Patient-specific elasticity distributions were estimated for lung and liver cancer radiotherapy patients, and functional correlation avoidance treatment plans were retrospectively developed. Brief descriptions of the major contributions are given below.

Using biomechanical, high-resolution breast geometry obtained from CT scans, a systematic assessment was performed to determine the feasibility of the elasticity estimation using clinically relevant displacement distributions. To simulate gravity induced breast deformation and mimic the chest-wall/breast tissue interface, the breast geometry was anchored at its base and allowed to deform between prone and supine patient positions. A forward iterative approach was used to solve the inverse elasticity problem. The feasibility and potential of the fast reconstruction of breast tissue elasticity using supine/prone patient postures was proven using these virtual phantom simulations.

The breast elastography methodology was extended to enable the performance of lung elastography using the internal breathing-induced deformation. For a systematic analysis, a physics-based virtual lung phantom with CT source geometry and a heterogeneous voxel-to-voxel elasticity distribution was employed. Our results showed that the elastography approach estimated the elasticity with 92% of voxels converging within 0.5 mm of the ground-truth displacement and 1 kPa of the ground-truth elasticity. This approach was extended to estimate and validate the elasticity distributions of 15 5DCT patient lung datasets and 11 patient 4DMR liver datasets. Overall, the results suggest that the lung elasticity can be measured with approximately 90%

convergence using routinely-acquired clinical 4D scans, indicating the potential for a lung and liver elastography implementation within the radiotherapy clinical workflow.

Dose is a limiting factor for many imaging studies. As such, the feasibility of performing elastography using simulated lower dose CT scans was investigated. The results suggest that the original tube current-time product of 40 mAs scans can be reduced to 20 mAs without affecting the reliability of the elastography results. The relationship between elasticity and lung tissue function was investigated using 13 4DCT patients with known GOLD 2017 COPD status. Elasticity distributions proved to be an effective spatial indicator of lung pathophysiology and displayed the potential be translated into a binary indicator for diagnostic staging purposes. Finally, elastography results were used to retrospectively derive functional contours for 7 lung SBRT patients for treatment planning purposes. For consistency, both clinical and functional lung avoidance VMAT SBRT treatment plans were developed. The functional avoidance plans were able to successfully spare functional lung regions while maintaining target coverage and meeting all normal tissue constraints, suggesting that incorporating functional information into SBRT planning may facilitate improved patient outcome after radiotherapy.

The works presented here provide a way to use conventional imaging to perform elastography within the radiotherapy workflow. The focus of this work concentrated on the lung anatomy but have been preliminarily expanded to the breast and liver. In our future investigation, the tools provided here can be extended to other anatomical sites and can provide a foundation for performing elastography and obtaining functional information for treatment planning purposes within the clinical radiotherapy workflow.

The dissertation of Katelyn Hasse is approved by:

Peng Hu

Michael McNitt-Gray

Ke Sheng

Daniel Abraham Low, Chair

University of California, Los Angeles

2018

To Ryan, Megan, Adam, Mom, and Dad

TABLE OF CONTENTS

---

[1] A version of of this chapter has been published as a manuscript in Medical Physics
[2] A version of this chapter has been published as a manuscripte in Biomedical Physics and Engineering Express
[3] This chapter is currently being prepared for submission to Medical Physics
[4] A version of this chapter has been submitted for review to Biomedical Physics and Engineering Express
[5] A version of this chapter has been submitted for review to The British Journal of Radiology
[6] This chapter is currently being prepared for submission to The British Journal of Radiology

LIST OF TABLES

LIST OF FIGURES

ACKNOWLEDGEMENTS

I would first like to thank my advisor, Dr. Anand Santhanam. His innovativeness and enthusiasm inspired me daily. I am very grateful for his guidance and patience throughout this process and look forward to the continuation of our work together.

I would also like to thank my committee, Dr. Daniel Low, Dr. Ke Sheng, Dr. Peng Hu, and Dr. Michael McNitt-Gray, for sharing their valuable expertise and time with me. I am fortunate to have been able to collaborate with and learn from each of you. A further thank you to Dr. McNitt-Gray and Reth Im for their passion, support, and leadership for our graduate program. The PBM group at UCLA is truly unique in the way it fosters student growth and learning in such a caring environment and I am blessed to have been a part of it.

I would like to thank my lab mates, Jack and Yugang. Without their initial pioneering work, my project would not have been possible. I would also like to thank the BMP/PBM crew for their friendship and collaboration.

I would like to thank my family, near and far, for their support. I would especially like to thank my parents, Sue and Jim, for all of their encouragement. My mom inspired me to pursue medical physics and continues to be the best example of strength, humility and patience. My dad encourages me to always be generous and never give up, and believes in me more than I believe in myself. I would like to thank my siblings, Megan and Adam, for occasionally visiting, always making me laugh, and keeping me grounded. I’m deeply grateful to Mr. Klapheke for motivating me to set big goals and for instilling in me the perseverance it takes to reach them. I would like to

thank my ninja fight club and martial arts instructors for the stress relief, puns, laughter, teamwork, and support during even the toughest obstacles.

Finally, I would like to thank Ryan, for his love, patience, and emotional and technical support. I wouldn't have made it a day without him.

VITA

EDUCATION

M.S.	University of California—Los Angeles, Biomedical Physics	2017
B.S.	University of Tennessee—Knoxville, Honors Nuclear Engineering, Minor in Mathematics	2013

AWARDS

UCLA Biomedical Physics Research Colloquium, Best Poster Presentation	2015
National Science Foundation Graduate Research Fellowship	2015-2018
UCLA Dean's Scholar Award Fellowship Recipient	2013-2014

PEER-REVIEWED PUBLICATIONS

Hasse, K., O'Connell, D., Neylon, J., Min, Y., Cao, M., Low, D.A., and Anand P. Santhanam. "Incoroporating lung tissue elasticity information into function preserving lung SBRT treatment planning." *The British Journal of Radiology*. Manuscript in preparation (May 2018).

Hasse, K., Hsieh, S., O'Connell, D., Neylon, J., Min, Y., Low, D.A., and Anand P. Santhanam. "Systematic feasibility analysis of performing elastography analysis using low dose CT lung image pairs." *Medical Physics*. Manuscript in preparation (May 2018).

Hasse, K., O'Connell, D., Neylon, J., Min, Y., Low, D.A., and Anand P. Santhanam. "Towards characterizing patient-specific lung elasticity as an imaging biomarker for assessment of functional lung regions." *The British Journal of Radiology.* Manuscript submitted for publication (March 2018).

Hasse, K., Han, F., Neylon, J., Hu, P., Yang, Y., and Anand P. Santhanam. "Estimation and validation of patient-specific liver elasticity distributions derived from 4DMR." *Biomedical Physics and Engineering Express.* Manuscript submitted for publication (March 2018).

Hasse, K., O'Connell, D., Min, Y., Neylon, J., Low, D.A., and A. P. Santhanam. "Estimation and validation of patient-specific high-resolution lung elasticity derived from 4DCT." Medical Physics. 45(2): 666-677. (2018).

Hasse, K., Neylon, J., and Anand P. Santhanam. "Feasibility and quantitative analysis of a biomechanical model-guided lung elastography for radiotherapy." Biomedical Physics and Engineering Express. 3(2): p. 025006. (2017).

Neylon, J., **Hasse, K**., Sheng, K., and Anand P. Santhanam. "Modeling and simulation of tumor-influenced high resolution real-time physics-based breast models for model-guided robotic interventions.” Proc. SPIE 9786, Medical Imaging 2016: Image-Guided Procedures, Robotic Interventions, and Modeling, 97860X. (2016);

Hasse, K., Neylon, J., Sheng, K., and Anand P. Santhanam. " Systematic feasibility analysis of a quantitative elasticity estimation for breast anatomy using supine/prone patient postures." Medical Physics 43.3. (2016);

SELECTED CONFERENCE PRESENTATIONS

“Characterizing and validating patient-specific high resolution lung elasticity from 4DCT imaging,” 59th AAPM Annual Meeting, 2017 (Denver, CO).

“Characterizing patient-specific lung elasticity from 4DCT for improving lung radiotherapy,” Physics and Biology in Medicine Research Colloquium, 2017 (Los Angeles, CA).

“Feasibility and quantitative analysis of 4DCT-based high precision lung elastography,” 58th AAPM Annual Meeting, 2016 (Washington, D.C.).

“Systematic Feasibility Analysis of a Quantitative Elasticity Estimation for Breast Anatomy Using Supine/prone Model Postures," 57th AAPM Annual Meeting, 2015. (Anaheim, CA).

“Systematic feasibility analysis of a quantitative elasticity estimation for breast anatomy using supine/prone model postures,” Physics and Biology in Medicine Research Colloquium, 2015. (Los Angeles, CA).

CHAPTER 1: INTRODUCTION TO THE DISSERTATION

1.1 Motivation

Radiation therapy is the treatment of choice for many cancers, including locally advanced stages of non-small cell lung cancer, liver metastases, and early stage breast cancer. Currently, radiotherapy treatment planning is based on anatomical imaging with a goal of treating the tumor while avoiding the normal tissue [1]. This assumes a homogenous radiation dose-response of normal tissue; however, it may not be the case that all normal tissues respond to radiotherapy the same. This work concentrations on introducing functional and biomechanical information into the treatment planning process to further expand the utility and effectiveness of radiotherapy while increasing patient quality of life.

1.1.1 Functional information has the potential to be useful in radiotherapy.

In current radiotherapy treatment planning, the potential risks of normal tissue irradiation are estimated based on the assumption of spatially uniform tissue function for a given organ [2]. However, patients referred to radiation therapy present with considerable spatial variations in a given organ's function; furthermore, both the lung and liver anatomies are known to have spatially heterogeneous function distributions and parallel functional behaviors [2]. Peers have demonstrated that functional treatment planning can be used to preferentially avoid normal tissue complications, since normal tissue function is not always reflected by anatomical imaging [3]. While clinical data and outcomes remain unknown, functional parameters such as perfusion and metabolism have been shown to correlate to better toxicity outcomes [4]. Specifically for the lungs, incorporating functional information such as ventilation and perfusion into treatment planning can reduce dose to highly functional regions. Radiotherapy that selectively avoids irradiating high-functioning lung regions may reduce pulmonary toxicity and improve patient quality of life.

Functional information has the potential to inform the radiotherapy process by highlighting functional changes during treatment and characterizing the extent of cancer and co-morbidities. Our underlying hypothesis is that it would be clinically beneficial to spare as much functioning normal tissue as possible during radiotherapy while ensuring adequate target coverage. This requires knowledge of the spatial-functional distributions for the anatomies in question.

1.2 Background

1.2.1 Current functional imaging techniques

Functional imaging techniques have been developed to portray biological characteristics of tissue. For tumors, they can visualize important hallmarks of cancer such as blood perfusion, oxygenation, and energy metabolism. For normal tissues, functional imaging techniques can provide maps of function that can be used to preferentially guide the deposition of radiation to parts of an organ where baseline function is reduced or absent [3]. Several functional imaging techniques, including pulmonary function tests using spirometry, single photon emission CT (SPECT), and xenon CT ventilation imaging, have been investigated to evaluate and describe overall lung function [5, 6]. These imaging techniques generally represent either ventilation or perfusion maps of the lung [7, 8].

For the liver, dynamic contrast enhanced computed tomography (DCE-CT), diffusion weighted magnetic resonance imaging (DW-MRI), single photon emission CT (SPECT), and positron emission tomography (PET)/CT have all shown promise for imaging liver metabolism and function [3]. All of these methods have illustrated the spatial heterogeneity of liver function, which is critical information for liver radiotherapy planning. Specifically, dynamic contrast enhanced MRI (DCE-MRI) quantitative parameters have been correlated with response rate and time to progression of colorectal metastases [9, 10].

Most of the lung and liver functional imaging techniques mentioned here are not used routinely due to increased radiation burden, adverse contrast reaction, long scan time, and high cost. Moreover, these techniques would be difficult to implement into the radiotherapy workflow because of the additional equipment required. Therefore, the goal of this work is to acquire functional information using imaging data that is already employed within the radiotherapy workflow.

1.2.2 Diseases that affect tissue function also affect biomechanical properties

Cancer is a disease that alters normal tissue structure and function, creating a tumor microenvironment that plays a crucial role in the pathophysiology of the disease [11]. It is believed that normal tissue stroma respond analogously to the cellular processes that accompany wound repair in an effort to repair damage due to carcinoma cell invasion [12]. Research further suggests that increasing tumor aggressiveness is accompanied by increasing collage accumulation in local histologically benign tissue [13]. For example, breast and prostate cancers are characterized by elevated collage deposition [14, 15]. The increase in collage deposition leads to an increase in tissue stiffness; therefore, quantitative stiffness estimates may prove to be an effective biomarker for assessing tumor grade and identifying more aggressive cancers. Furthermore, peers have demonstrated that diagnostic discrimination of tissue malignancy may be possible using tissue elasticity as a metric [16, 17].

Tumor formation and degeneration may cause inflammation and fibrosis within stromal cells, which can substantially alter the elasticity of the tumor and surrounding tissues. The elastic modulus of lung tissue is known to change under the influence of non-carcinogenic pathologic processes such as inflammation and neoplasm as well [18]. For the lung, function is closely related to the mechanical properties of parenchyma; diseases of the lung that alter lung function often do so by altering the amounts of elastin and collagen, and hence the elasticity, of parenchymal tissue [19]. Chronic obstructive pulmonary disease (COPD), a progressive lung disease, is characterized by damaged parenchymal with altered mechanical properties and ventilation profiles. For example, the destruction of collagen and elastin fibers in emphysematous lung tissue decreases the strength and elastic recoil of the tissue, reducing the elastic modulus. Since changes in tissue stiffness have been well correlated with abnormal pathological processes, we hypothesize that imaging parameters related to tissue elasticity may provide an effective biomarker for differentiating functional regions of tissue.

1.2.3 Elastography techniques

Elastography is a non-invasive imaging technique for quantifying the local elasticity distribution in soft tissues [20, 21]. Elastography techniques can typically be described in three steps: deforming the tissue of interest, imaging the subsequent deformation, and calculating the corresponding mechanical properties [20, 22, 23]. Elastography is customarily performed with ultrasound (US) or MR.

For the breast, elastography imaging techniques have been previously investigated by peers for differentiating benign from malignant disease, possibly reducing the overall number of breast biopsies [24-26]. Popular breast elastography imaging techniques include shear wave elastography, where the speed of a shear wave throughout tissue provides a quantitative measure of lesion stiffness, and freehand elastography, where a handheld transducer is used to axially compress the tissue a few millimeters [17]. Both US- and MR-based implementations of these techniques have been shown as feasible ways to identify and characterize cancerous tumors in breast tissues, as malignant lesions exhibit considerably higher elasticity than the surrounding tissue [11, 18, 19]. Elastography techniques may also be able to quantify and characterize radiotherapy-associated changes in breast tissue, predicting the severe hardening and shrinkage that influence quality of life after breast radiotherapy [27].

The complexity of the lung anatomy, particularly the air in the lungs, renders conventional elastography techniques difficult to implement [28, 29]. Advanced techniques, such as magnetic resonance elastography (MRE) using hyperpolarized gases and optical coherence elastography using magnetic nanoparticles have been investigated to overcome the complications of the lung [30, 31]. Lung elastography has many potential radiotherapy clinical benefits, including the ability to discriminate between healthy and diseased tissue, visualize lung tissue changes, and detect pathological changes within the lungs. Furthermore, knowledge of material properties of lung tissue may lead to methodologies that correctly predict outcome and response to radiation therapy, calculate mechanical deformation of surrounding tissue caused by tumor growth, and predict tissue movement during radiation therapy treatments [32-34].

MRE has also been investigated for hepatocellular carcinoma patients. MRE uses synchronized cyclic shear wave displacement, encoded into the phase of the MR signal, to derive the elastic properties of tissue [35-38]. Recent MRE results have found that liver stiffness in patients with radiation-induced liver disease was significantly higher in patients without radiation-induced liver disease, illustrating the complicated and potentially useful association between liver stiffness and hepatic pathophysiology [39, 40].

Despite its usefulness and proven diagnostic accuracy [41, 42], elastography has not yet been systematically investigated within the radiotherapy context.

1.2.4 Opportunities for elastography within a radiotherapy context

For radiotherapy, elastography may improve the ability to visualize disease progression within the lungs and liver. Elastography is sensitive to tumor cell necrosis, edema, and fibrosis. Tissue elasticity is affected by radiation therapy, and it is plausible that elastography may be used to monitor tumor response and normal tissue toxicity [34].

Within the context of radiotherapy, additional imaging modalities such as US and MR, which are typically used for elastography, raise the need to precisely register the new images with the treatment planning images, which has not yet been systematically addressed. The MR machinery and hyperpolarized noble gases commonly required for other elastography techniques are very rarely found within a radiotherapy suite. There is a key knowledge gap in developing elastography methods using imaging modalities that are already in use within the clinical radiotherapy workflow.

Common lung radiotherapy imaging protocols require the acquisition of 4DCT images for treatment planning to account for lung tumor motion [43]. One focus of this dissertation was to formulate a methodology to perform lung elastography using only the deformation information that is available from the 4DCT data acquired during radiotherapy treatment planning. 4DCT-based elastography will provide “free functional information”. Such “free functional information” can lead to improved treatment plans that spare the normal functioning lung tissues, reducing normal lung toxicity.

Liver elastography is typically performed with MRE [44]. However, MRE techniques are not standard of care for patients undergoing SBRT for liver tumors and require highly specialized equipment. To obtain functional elasticity information with the liver radiotherapy setup, a secondary focus of this dissertation was to perform 4DMR-based liver elastography using the images acquired from 0.35 T ViewRay machines used for liver SBRT. To our knowledge, elastography has not yet been performed using the 4D methodologies currently found within the radiotherapy treatment planning workflow for the lung and the liver.

1.3 Specific Aims

The ultimate goal of this dissertation is to facilitate the incorporation of functional elasticity information into a radiotherapy treatment planning workflow. To accomplish this, the following specific aims focused on developing key methodologies for obtaining and utilizing reliable patient-specific tissue elasticity from imaging and deformation data acquired routinely within the lung, liver, and breast radiotherapy workflows.

Specific Aim 1 (SA1): Perform systematic studies using virtual deformable anatomical phantoms and a biomechanical model to assess the feasibility of obtaining tissue elasticity information from deformation data.

Specific Aim 2 (SA2): Utilize biomechanical model and deformation vector fields to obtain tissue elasticity information from 4D imaging.

Specific Aim 3 (SA3): Incorporate functional and biomechanical information into treatment planning.

Broader implications: The specific aims addressed in this dissertation provide a solution for obtaining functional information using images and deformation information acquired within the radiotherapy workflow for breast, lung, and liver anatomies. Ultimately, these works offer a therapeutic tool that can be used to reduce functional tissue toxicity for the lung, liver, and breast anatomies.

1.4 Overview

Chapters 2 through 8 consist of edited manuscripts produced from the core projects of this dissertation that have been published, are under review, or are being prepared for submission. Each chapter contains a thorough introductory section that discusses the motivation for the project and prior work in the field; thus, the background material for each project was not included in this chapter.

SA1 is addressed in Chapters 2 and 3. An algorithm for estimating elasticity distributions from the gravity-induced deformation of a virtual breast phantom is developed in Chapter 2. In Chapter 3, the elasticity estimation methodology is extended to the internal deformation of virtual lung phantoms, along with details of the challenges faced for the more complex anatomy. SA2 is addressed in Chapters 4, 5 and 6. In Chapter 4, the validated elasticity estimation methodology is applied to patient 4DCT data to estimate patient-specific elasticity distributions. Whether elastography results can be reliably obtained for low dose CT applications is explored in Chapter 5. The elasticity estimation methodology is applied to patient 4DMR liver datasets in Chapter 6. Chapters 7 and 8 address SA3. In Chapter 7, the elasticity distribution is related to clinically relevant functional information, and in Chapter 8 , the elasticity distributions are retrospectively utilized to achieve functional avoidance treatment planning. The conclusions of the dissertation are presented in Chapter 9, and further avenues of interest for each project are also discussed.

CHAPTER 2: PERFORM SYSTEMATIC STUDIES USING VIRTUAL ANATOMICAL PHANTOMS AND A BIOMECHANICAL MODEL TO ASSESS THE FEASIBILITY OF OBTAINING TISSUE ELASTICITY INFORMATION FROM GRAVITY-INDUCED DEFORMATION DATA.

Systematic feasibility analysis of a quantitative elasticity estimation for breast anatomy using supine/prone patient postures

A version of this chapter has been published as a manuscript: Med Phys, Vol. 43, No. 3, 2016. doi: 10.1118/1.4941745

2.1 Introduction

Breast cancer is the most commonly diagnosed cancer for women in the United States, with about 1 in 8 U.S. women developing invasive breast cancer over the course of her lifetime [1]. The general approach to early stage breast cancer treatment usually involves a lumpectomy, followed by post-operative radiotherapy, which significantly reduces the risk of cancer recurrence. Post-operative breast radiotherapy can be challenging because of the deformable nature of the breast tissue. Day-to-day changes in breast anatomy and positioning present an obstacle when trying to attain an ideal and repeatable patient set-up. It has been previously documented that the breast alignment can vary by more than 5 mm in any dimension from one day to another without the use of immobilization devices [45]. Existing immobilization devices designed for rigid anatomies are not suitable for fixing the breast position. Engineering novel immobilization devices for precise and reproducible breast set up requires modeling of the breast deformation for given forces applied to the breast surface [3]. Therefore, the first step in engineering such immobilization devices is a systematic development of subject-specific biomechanical breast models.

High-resolution biomechanical physics-based models have been used to develop patient-specific representations of deforming anatomy [4]. Sophisticated biomechanical models can simulate deformations and physiological changes in different anatomies, creating a dynamic physical atlas [5]. Patient-specific biomechanical breast models are necessary in order to use material properties of soft tissue to correctly predict outcomes and response to radiation therapy, calculate mechanical deformation of surrounding tissue caused by tumor growth, and accurately model tissue movement during radiation therapy treatments [6-8]. Biomechanical models of the breast have also been used to more precisely locate cancerous tissue and simulate breast shape during a variety of clinical applications [2]. Biomechanical models must take into consideration the laws governing the mechanical properties of tissue—elastography is a non-invasive way to image the physical distribution of these properties [9]. Knowing the distribution of elastic properties throughout soft tissue can lead to design and development of immobilization devices in addition to yielding valuable biomechanical information in a patient-specific manner.

A critical limitation in performing breast elastography within a radiotherapy setting is that the clinical breast radiotherapy protocols only involve prone and supine CT scans [46]. With additional MR and ultrasound imaging being unattainable within a clinical radiotherapy workflow, it is important to study the feasibility and accuracy of deriving breast tissue mechanical properties based on the two CT scans.

The focus of this study is to formulate a methodology for performing breast elastography with subject specific clinical supine/prone CT data, and to systematically validate and quantify the accuracy of this methodology. A linear elastic biomechanical model, which has been previously used for representing head and neck deformations [5], will be employed as a deformation model to represent the breast anatomy. Each mass element of the model denotes a single voxel from the supine or prone CT image data. The underlying elasticity is then estimated using a gradient descent binary search algorithm coupled with a fast-simulated annealing (FSA) based model parameter optimization.

2.2 Materials and Methods

The primary aim of this study was to formulate a method to estimate the Young's moduli [47] associated with each voxel in the breast anatomy and to quantitatively assess the accuracy of the estimated values using virtual breast phantoms. From a mathematical perspective, reconstructing the elasticity distribution of tissue can be approached in either a direct or an inverse manner. The direct approach reconstructs an elastographic image by converting the strain value at each voxel to a relative Young's modulus using a simple model constraint, such as Hooke's Law [21]. This approach is limited, however, and has been shown to be inferior when compared to the inverse approach [48]. The inverse approach, or model-based method, is an iterative approach that allows for more reasonable and realistic model constraints. Peers have formulated the inverse elasticity problem as a parameter optimization problem with an objective to minimize the difference between measured displacement and that computed by a biomechanical model representing observed mechanical behavior [19].

In our approach, we formulated breast elastography as an inverse problem. The supine-to-prone breast deformation is known to be gravity-induced [23, 24]. We used the observed tissue displacement between supine/prone postures as our measured ground-truth displacement. A biomechanical simulation was employed as the forward deformation model to evaluate the inverse breast elasticity problem, with its parameters being iteratively updated. It has been shown in [5] that the deformation of the biomechanical model acted upon by gravity matches the expected soft tissue response, indicating its potential for modeling the supine-to-prone breast deformation. Implementation of this model in a graphics processing unit (GPU) environment allowed for fast and accurate breast tissue elasticity estimations.

In this section, we first present the GPU-based forward deformation model that was devised to represent the breast anatomy. We then present the inverse formulation that was used to estimate the breast tissue elasticity. Finally, we present our experiments in systematically assessing the accuracy of the estimated tissue elasticity.

2.2.1 Forward problem.

While the forward problem is previously discussed in [5], for clarity, we hereby present the model.

2.2.1.1 Model initialization and geometry. The biomechanical model was constructed from clinically acquired or virtually constructed CT data. We defined deformation space as the virtual space where the model geometry can be instantiated and deformed. The model geometry was represented by mass elements corresponding to the center of each voxel of anatomy in the CT image. Mass elements were connected by mass-spring damping (MSD) connections in the deformation space. Connecting the mass elements with each other using a spring damper formulation ensured that the mass elements could deform in a physically realistic manner. The connections were established as follows: A local neighborhood search was performed in a parallelized manner around each mass element to find nearby elements. When a nearby element was within a threshold distance (determined by the voxel size of the input CT, approximately 3 mm in our case) from the search element, an MSD connection was established and the nearby element became a connected element for the given search element. The rest length and orientation of each connection was then recorded and assigned a Young’s modulus and a Poisson’s ratio as the final step in the model initialization.

2.2.1.2 Forward deformation computation. The corrective forces on each mass element were calculated as a summation of tensile force, shear force, and a dashpot damping force. At rest state, the elastic internal corrective forces were set to zero. When deformed, the model’s mass elements were relocated to new positions inside the deformation space, which caused the internal corrective forces to be non-zero. For each mass element, a, the tensile force, $\vec{f}_{Y,ab}$, shear force, $\vec{f}_{S,ab}$, and the dashpot damping force, $\vec{f}_{v,ab}$, were calculated for each connected element, b, and summed to find internal corrective force, $\vec{f}_a$:

$$\vec{f}_a = \sum_b \left(\vec{f}_{Y,b} + \vec{f}_{S,b} + \vec{f}_{v,b} \right) . \qquad \textbf{(2-1)}$$

The elastic force acting between the two mass elements is described by:

$$\overrightarrow{f}_{E,ab} = \sum_b \left(E_{ab} * \frac{\Delta L_{ab}}{L_{ab}} \right), \qquad \textbf{(2-2)}$$

where E_{ab} is the effective Young’s modulus acting between the two elements a and b, and L_{ab} is the rest length distance, and ΔL_{ab} is the change in length between the two elements. Since soft tissue is modeled as a linearly elastic material, Equation (2-2) is derived from the inverse relationship between Young’s modulus and displacement; for a constant force, if elastic modulus increases then displacement must decrease and vice versa [49].

The shear spring force ($\vec{f}_{S,ab}$) on element a due to element b is described by

$$\vec{f}_{S,ab} = \sum_b \left(S_{ab} * \frac{L_{ab} - \Delta L_{ab}}{L_{ab}} \right), \qquad \textbf{(2-3)}$$

where S_{ab} is the shear moduli between elements a and b, set to 4 kPa for each voxel in our estimations, an approximation based on the relationship between shear modulus, Young’s modulus, and Poisson's ratio and similar to values seen in [50, 51]. The dashpot damping force is calculated from the relative velocities $\vec{v}$ of elements a and b, and a local damping factor μ_{ab}

$$\vec{f}_{v,ab} = \sum_b(\mu_{ab} * (\overrightarrow{v_b} - \overrightarrow{v_a})). \qquad \textbf{(2-4)}$$

Once the internal forces were computed, the new positions, $\vec{x}_a^{n+1}$, and velocities, $\vec{v}_a^{n+1}$, of the mass elements were updated from the values $(\vec{x}_a^n, \vec{v}_a^n)$ at the previous iteration n, using Implicit (Backward) Euler integration.

$$\vec{v}_a^{n+1} = \vec{v}_a^n + \left(\frac{\vec{f}_a}{m_a} + \vec{g}\right)\delta\,, \qquad \textbf{(2-5)}$$

$$\vec{x}_a^{n+1} = \vec{x}_a^n + \vec{v}_a^{n+1}\delta, \qquad \textbf{(2-6)}$$

where δ was the time step between iterations, m_a was the mass of mass element a, and $\vec{g}$ was acceleration due to gravity.

The Euclidean distance between $\vec{x}_a^n$ and $\vec{x}_a^{n+1}$ for each mass element was taken to be the ground-truth displacement for that mass element, and then the biomechanical model was reset with an initial guess elastic distribution. The iterative binary search optimization scheme was utilized until convergence occurred.

2.2.2 Inverse analysis.

Solving the inverse elasticity problem was accomplished by iteratively deforming the model from rest state, as described in the section above. A gradient-based binary search was used as an iterative optimization scheme to update the spatial-elastic distribution in order to minimize the discrepancy between ground-truth and computed mechanical response, or displacement, for each voxel, while a fast-simulated annealing algorithm was simultaneously employed to optimize model parameters.

2.2.2.1 Iterative elasticity estimation. The iterative scheme for recovering the Young's modulus distribution was derived from the relationship between Young's modulus and displacement [25].

An elastic solid can be viewed as a series of mass elements connected by a grid of ideal linear elastic connections, where the elastic modulus acts on each mass element similarly to a material constant. Likewise, the resulting displacement can be related to the stiffness of the material as described in Equation (2.2). This equation illustrates that the elastic modulus and displacement are inversely related—if elastic modulus increases then displacement must decrease and vice versa. This principle defines the reasoning behind the iterative process for estimating elasticity.

The general basis of our reconstruction technique is to minimize the difference between the ground-truth and calculated displacements. Given an initial Young's modulus, the biomechanical model will provide theoretical estimates of mass element displacements. These displacements were then compared with ground-truth displacement vectors, and the Young's modulus distribution was iteratively updated until the error was minimized. Intermittent mass element displacements were generated on a per voxel basis by updating the Young's modulus values as described below.

The initial (E_a), minimum ($E_{min,a}$), and maximum ($E_{max,a}$) Young's modulus values were initialized for each voxel, a, in the physics-based biomechanical model. The displacement differential was calculated with the following relation

$$\varDelta d_a = d_{0,a} - d_a, \tag{2-7}$$

where $d_{0,a}$ and $d_a$are the ground truth and calculated displacement of voxel $a,$ respectively. The displacement differential was then used to update $E_{min,a}$ and $E_{max,a}$ as follows:

$$if\ \varDelta d_a < 0: \begin{cases} E_{min,a} = E_a \\ E_{max,a} = E_{max,a} \end{cases} \tag{2-8}$$

$$if\ d_a > 0: \begin{cases} E_{min,a} = E_{min,a} \\ E_{max,a} = E_a \end{cases} \tag{2-9}$$

After the minimum and maximum values have been updated, a new trial solution was generated at each iteration by updating the Young's modulus values

$$E_a = \frac{(E_{min,a} + E_{max,a})}{2}, \qquad (2\text{-}10)$$

where E_a now becomes the initial value for the next iteration.

This iterative procedure is based upon the modified Gauss-Newton method [26, 27], which was chosen because it requires no assumption about the homogeneity of the tissue in question, the implementation is straightforward, and the convergence occurs within *O(log n)* iterations. For our purposes, the range of Young's modulus values is given by $E_{min,a} < E_a < E_{max,a}$, where $E_{min,a}$ and $E_{max,a}$ are typically 1 kPa and 200 kPa for living soft tissues [27]. Convergence was obtained when each voxel of tissue was within 1 mm of the ground-truth deformation.

2.2.2.2 Fast-simulated annealing. Besides elasticity, another parameter of the biomechanical model that needs to be optimized is the number of iterations that the biomechanical model undergoes deformation. Iteration number refers to the deformation time for each iteration of the simulation. This is important because deformation time greatly impacts whether the system reaches an equilibrium state or whether the system is still in transition when the displacement values are recorded.

Fast-simulated annealing (FSA) was chosen to optimize iteration number because even in the presence of noisy data, it may not find the optimum solution, but it will find a very good solution very quickly. The FSA algorithm generates randomized iteration number candidates, and checks if this candidate solution is better than the current solution. If so, the current solution is replaced with the candidate solution, but if not, the current solution is replaced with a given probability. This allows us to accept iteration numbers that are not ideal in order to explore more of the possible solution space. The probability decreases with a logarithmic temperature scheme until the system converges or a set computation time has been exhausted. The lowered temperature limits the number of non-ideal iteration numbers that are accepted so that the solution is allowed to approach the global minimum. A flow chart describing the FSA process is shown in Figure 2-1.

2.2.3 Numerical analysis.

To enable a systematic study of the inverse analysis process, the biomechanical model was employed to generate a hemispherical geometry representing a breast in order to simulate the ground-truth displacement vectors. The hemispherical geometry was approximated from a volume rendered patient CT image of a breast in the prone position (Figure 2-2(a)). The chest-wall/breast tissue attachment interface is mimicked by anchoring the base of the hemisphere to prevent motion in the top layer of mass elements, which is illustrated in Figure 2-2(b).

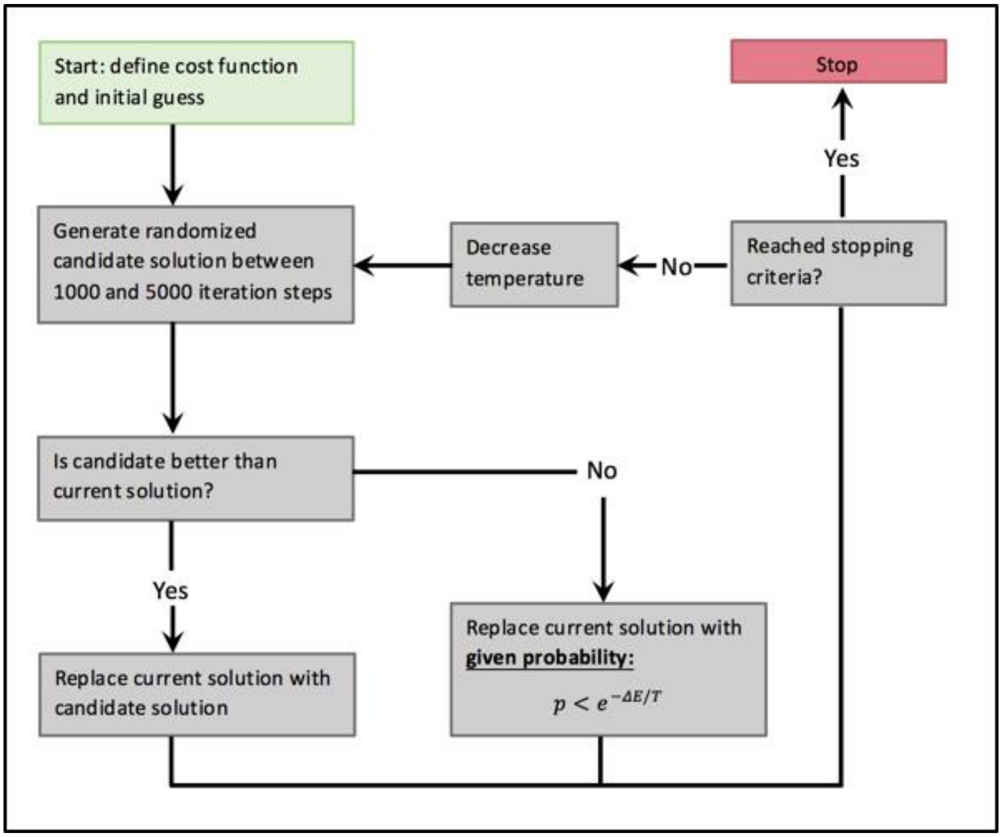

Figure 2-1: Flowchart depicting fast-simulated annealing process

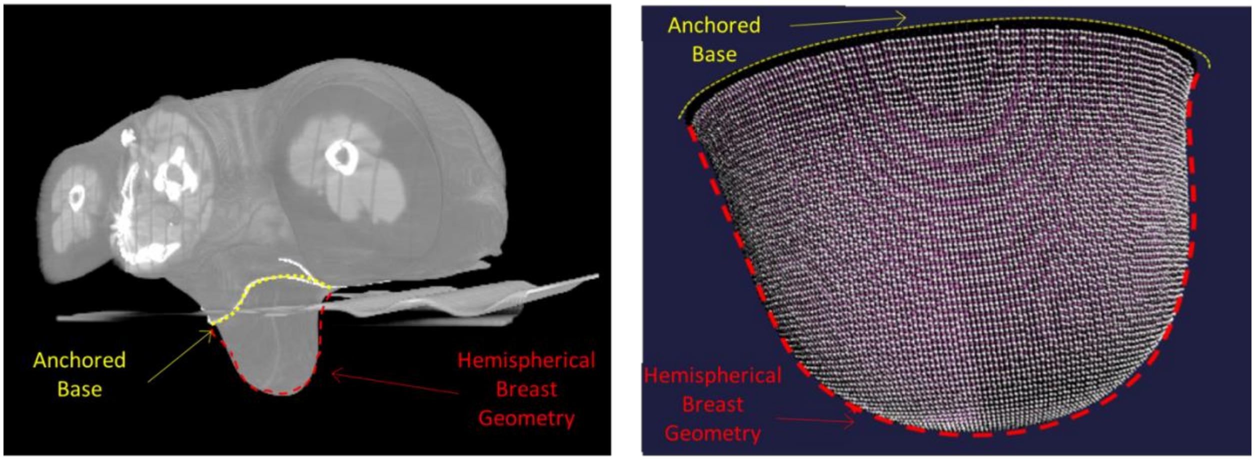

Figure 2-2: Volume renderings of prone DICOM CT (a) and biomechanical simulation with anchored base of a 128-voxel diameter hemisphere to mimic chest-wall interface (b).

<u>2.2.3.1 Virtual breast phantoms.</u> Two different hemispherical geometries were constructed with 1 mm^3 voxels to represent different model resolutions. The lower resolution simulation contained 100,000 voxels and had a 64 voxel diameter, while the higher resolution model contained about 600,000 voxels with a 128 voxel diameter. A homogenous elastic modulus distribution of 20 kPa was initially used to represent a mixture of fatty and glandular breast tissue [22]. Spherical inhomogeneities with diameters of 5, 10, and 15 mm were placed within the geometry [29]. These spherical masses, representing breast tumors within the tissue, were used to signify ductal carcinomas in situ (DCIS), invasive ductal carcinomas (IDC), and fibroadenomas, with elasticity values of 75 kPa, 90 kPa, and 110 kPa respectively, as derived from the literature and shown in Table 2-1 below [30]. The breast geometry was divided into quadrants and for each distribution, a tumor was placed either in the center of the hemisphere or the center of one of the quadrants. Combining the different types, sizes, and locations of tumors along with the different image resolutions resulted in 90 different ground-truth elasticity distributions. The biomechanical breast model was deformed in turn with each of these ground-truth elasticity distributions, with the resulting ground-truth displacements calculated as explained above.

Table 2-1: Elasticity values for different components of breast tissue found from the literature [30].

Breast Tissue Type	Fatty/Glandular Tissue (kPa)	Fibrous Tissue (kPa)	Ductal carcinoma in-situ (kPa)	Invasive ductal carcinoma (kPa)
Tissue Elastic Modulus	20	110	75	90

2.2.3.2 Inverse analysis with no a priori information. After the ground-truth deformation was recorded, the estimated elasticity was reset to an initial guess elasticity distribution. Primarily, the elasticity was reset to a homogenous initial guess in which no assumptions were made about the anatomy in question. This initial guess was used in order to investigate the robustness of our methodology by showing that the system could converge regardless of the disparity between the initial guess and the ground-truth elastic distribution. The time and accuracy of the convergence for each ground-truth distribution were recorded and analyzed.

2.2.3.3 Inverse analysis with a priori information. We then performed the same study using *a priori* information, which would be gained from the HU values obtained from the supine/prone CT images. For the purposes of our feasibility study, HU values were simulated and assigned to each voxel with values from the literature depending on whether the voxel represented normal fibroglandular tissue or was a part of one of our simulated spherical tumors [31]. These HU values were input into our simulation, and if the HU value for a voxel was above a certain threshold, that voxel was assigned a higher initial elastic modulus. It is expected that, using the *a priori* information, we can more precisely define the boundary of a tumor and decrease the computation time.

2.2.3.4 Fast-simulated annealing. A fast-simulated annealing (FSA) algorithm is used to optimize iteration number while the binary search to optimize elasticity is performed simultaneously, which is illustrated in Figure 2-3. To ascertain whether the fast-simulated annealing obtained an optimum solution, displacements were recorded for a random sample of the ground-truth elasticity distributions, and then the simulation attempted to recreate the ground-truth elasticity distributions both with and without the FSA optimization. For scenarios, when the FSA algorithm was not employed, the iteration number was set to 4000, which was the ground-truth iteration number.

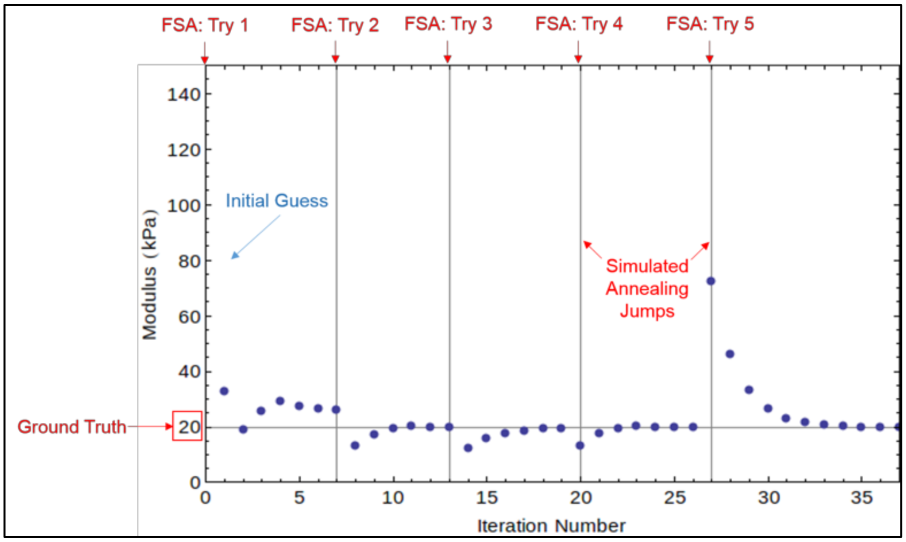

Figure 2-3: Illustration of the simultaneous binary search and FSA algorithms. The red lines indicate an FSA jump was performed, which the binary search process is illustrated by the points.

2.2.3.5 Error metric. The metric used for quantifying the accuracy of the inverse analysis was a combination of both the estimated elasticity and the displacement error produced using the estimated elasticity. Higher elasticity values of the tumor voxels represent stiffer connections, so a small error in the elastic moduli did not as greatly increase the displacement error when compared to the more elastic interactions with the normal tissue voxels. To determine whether or not our elasticity accuracy will translate to the required clinical accuracy, we deformed the synthetic phantoms and plotted the maximum displacement versus elasticity for hemispheres with different homogeneous elastic moduli distributions, and fit a curve to the plotted points, which is shown in Figure 2-4. The resulting equation is

$$d \cong 16.11 - 0.231297 * E + 0.00112246 * E^2 , \qquad \textbf{(2-11)}$$

which fit the data with an R^2 value of 0.996. Using this equation, we concluded that a displacement differential of $\Delta 1$ mm (or sub-millimeter clinical accuracy) corresponds to an elasticity differential of $\Delta 0.5$ kPa for voxels with elastic moduli falling somewhere in the normal tissue range (around 15 – 25 kPa). Similarly, a displacement differential of $\Delta 1$ mm corresponds to an elasticity differential of $\Delta 3$kPa for voxels with higher elasticity values in the tumor range (around 70 – 100 kPa). The values of 0.5 kPa and 3 kPa were approximated to 1 and 5 kPa for more robust binning, and were used to bin the elasticity differentials between estimated and ground truth elasticity distributions for the purposes of our study. Other elastography estimation methods, such as combined ultrasound and FE models, strive for displacement error that is less than the smallest tumor diameter that can be found in breast tissue, which is around 3 mm [32]. For a direct comparison, the displacement accuracy that is less than 3 mm is also presented for individual cases in the following section.

Besides looking at the results averaged over all of the distributions, we present the three other criteria that were also investigated: (a) relation between the use of *a priori* information and accuracy, (b) relation between the image resolution geometry and the accuracy, and (c) effectiveness of the FSA algorithm. A two-sample t-test was performed to analyze whether the statistical significance of the differences in the means of each population for each of the three criteria listed above. Volume renderings of the resultant and ground-truth elasticity distributions were also used to visually analyze the results as an addendum to the numerical results. The results gleaned from the systematic study are presented in the following section.

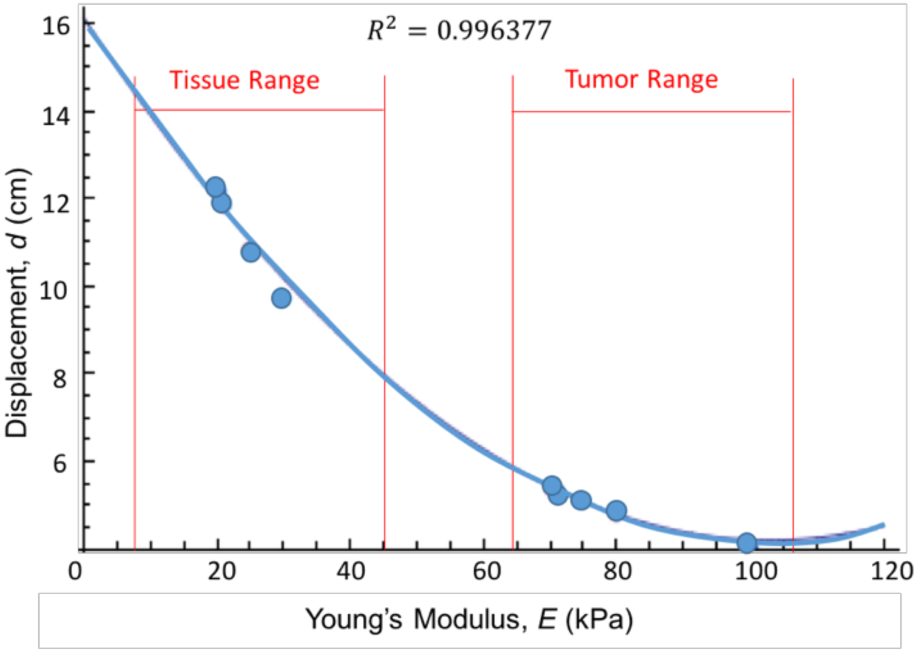

Figure 2-4: Displacement versus Young's Modulus fitted plot

2.3 Results

In this section, we present the results obtained from the systematic study. To illustrate the aptitude of the forward model for representing gravity-induced soft-tissue deformations, the biomechanical simulation was used to establish geometry from a prone breast DICOM CT Figure 2-5(a & b) with a homogenous elasticity distribution. This geometry was then deformed with gravity to simulate the supine orientation Figure 2-5(c & d), illustrating that the model can accurately represent the soft-tissue deformation between prone and supine breast postures. Figure 2-5 shows DICOM CT (a & c) and biomechanically simulated (b & d) prone and supine breast positions. Figure 2-5(e) shows an overlay of images (c) and (d). ImageJ was used to perform an image comparison and the images were shown to be 85.23% similar. The mismatch between the two images, highlighted in yellow, can be explained by segmentation errors, as the breast was manually segmented from the

DICOM CT images, and intensity differences between the DICOM CT and the mass-elements in the biomechanical simulation.

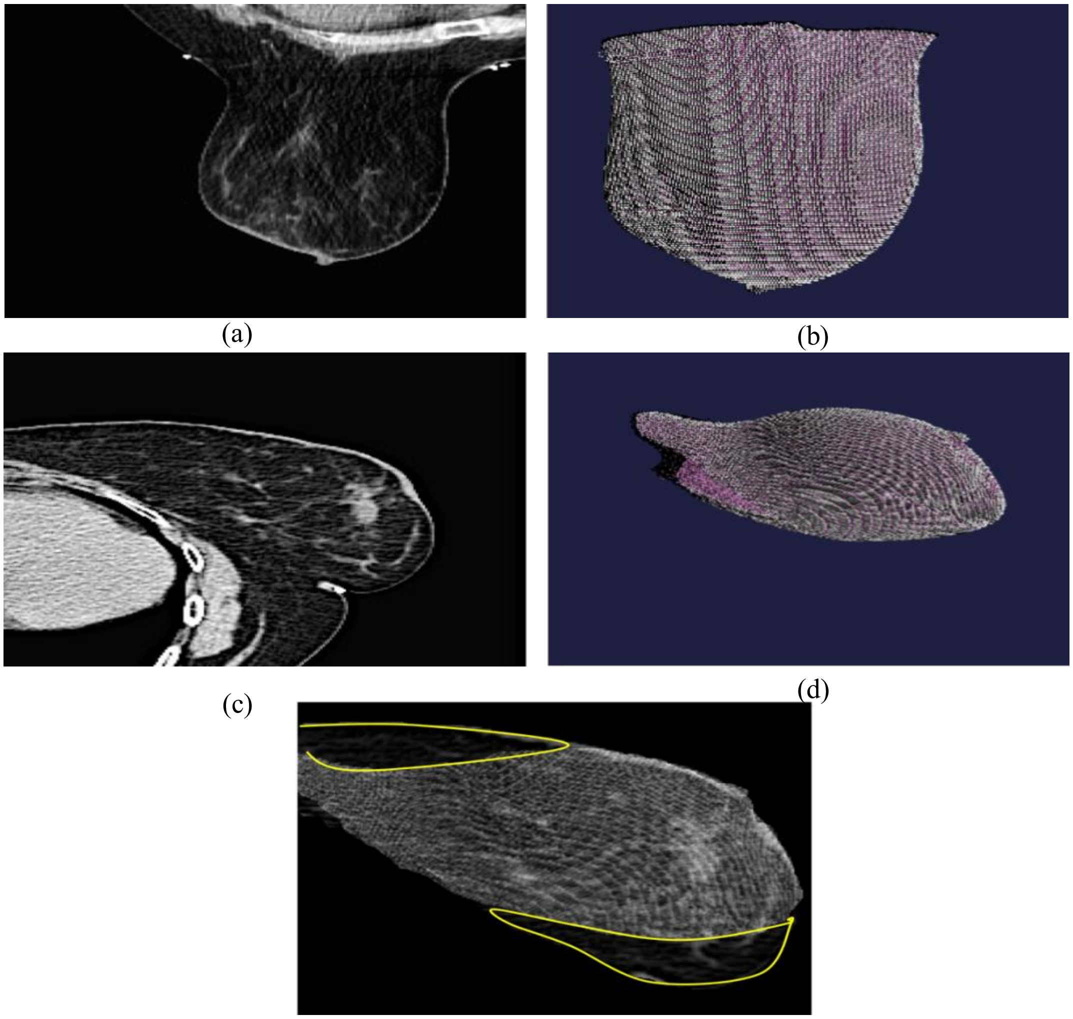
(a) (b) (c) (d) (e)

Figure 2-5: Prone DICOM CT (a) and biomechanically simulated (b) data. Supine DICOM CT (c) and biomechanically simulated (d) data. The biomechanically simulation shown in (b & d) was generated from the DICOM CT images which had a resolution of 134 x 144. Images (c) and (d) were overlaid in (e) to give a direct comparison of our simulation to the DICOM CT.

<u>2.3.1 Model resolution.</u>

To analyze the impact of the breast model resolution on the estimated elasticity, the simulation was performed with two different resolution of hemispheres. The lower resolution, 64 voxel diameter hemisphere converged on average with 98.87% of the voxels within 1 mm of the ground-truth results. This corresponded to 92.02% of voxels being within 1 kPa of their ground truth elasticity values, and 96.92% of voxels converging within a 5 kPa window. The higher resolution, 128 voxel diameter hemisphere converged on average with 96.19% of the voxels within 1 mm of the ground-truth displacement, resulting in 86.15% of voxels converging within a 1 kPa elasticity window and 98.38% converging within 5 kPa. These results are summarized in Table 2-2. A two-sample t-test of 20 different images shows that the differences between the results of the lower and higher resolution datasets was not significant ($P > 0.05$). Though the average elasticity error for the 1 kPa bins in each instance seems to be dissimilar, the t-test considers a one-to-one correspondence between the values in the samples. For example, the elasticity error of every ground-truth elasticity distribution is compared between the lower and higher resolution cases. Because a multitude of distributions were considered, the differences between the average values were not significant. This implies that regardless of image resolution, we can produce results with similar accuracy, which is paramount to implementation in the clinical setting. More specifically, Table 2-3 shows examples of the results of lower and higher resolution datasets for a large fibroid in the center, a small IDC in Quadrant II, and a medium DCIS in Quadrant IV. These results again illustrate that for multiple tumor locations, regardless of tumor type or size, both the low and high resolution reconstructions produce similar elasticity distribution. Figure 2-6 shows volume renderings of a medium IDC located in quadrant II for both the low resolution (a) and the high resolution (b) hemispheres. Both cases are visually and numerically similar—the boundary between the differing elasticity values is well-differentiated for both low and high resolutions. The inverse elasticity algorithm is invariant to image resolution, further indicating that image resolution will not hinder the accuracy of our reconstruction.

Table 2-2: Overall results and results for simulations run with and without a priori information, with and with the FSA algorithm, and with lower and higher resolutions.

	Elasticity Window		**Displacement Error**
Overall Results	$\pm 1\ kPa$ (%)	$\pm 5\ kPa$ (%)	$< 1\ mm$ (%)
	87.60 ± 3.18	97.15 ± 4.73	96.81 ± 3.62
Averages	$\pm 1\ kPa$ (%)	$\pm 5\ kPa$ (%)	$< 1\ mm$ (%)
Mean of datasets without a priori	87.60 ± 4.42	97.15 ± 1.26	96.81 ± 3.62
Mean of datasets with a priori	90.57 ± 3.23	98.15 ± 2.52	98.26 ± 2.82
Averages	$\pm 1\ kPa$ (%)	$\pm 5\ kPa$ (%)	$< 1\ mm$ (%)
Mean of datasets without FSA	96.57 ± 2.38	98.75 ± 0.78	98.78 ± 1.01
Mean of datasets with FSA	96.40 ± 1.14	97.88 ± 1.31	97.48 ± 1.72
Averages	$\pm 1\ kPa$ (%)	$\pm 5\ kPa$ (%)	$< 1\ mm$ (%)
Mean of datasets with Lower Resolution	92.02 ± 3.48	96.92 ± 1.32	98.87 ± 0.65
Mean of datasets with Higher Resolution	86.15 ± 4.10	98.38 ± 2.41	96.19 ± 1.87

Table 2-3: Example 64 and 128 voxel (lower and higher resolution) test cases for a large fibroid in the center of the hemisphere, a small IDC in quadrant II, and a medium DCIS in quadrant IV.

	Elasticity Window		**Displacement Error**	
Large Fibroid Center	$\pm 1\ kPa$ (%)	$\pm 5\ kPa$ (%)	$< 1\ mm$ (%)	$< 3\ mm$ (%)
Lower Resolution	88.25	96.36	94.98	100.00
Higher Resoltuion	80.42	98.45	89.95	100.00
Small IDC Quadrant II	$\pm 1\ kPa$ (%)	$\pm 5\ kPa$ (%)	$< 1\ mm$ (%)	$< 3\ mm$ (%)
Lower Resolution	85.28	98.85	96.58	100.00
Higher Resolution	86.91	98.12	94.92	100.00
Medium DCIS Quadrant IV	$\pm 1\ kPa$ (%)	$\pm 5\ kPa$ (%)	$< 1\ mm$ (%)	$< 3\ mm$ (%)
Lower Resolution	74.86	99.31	99.83	100.00
Higher Resolution	75.89	99.22	99.19	100.00

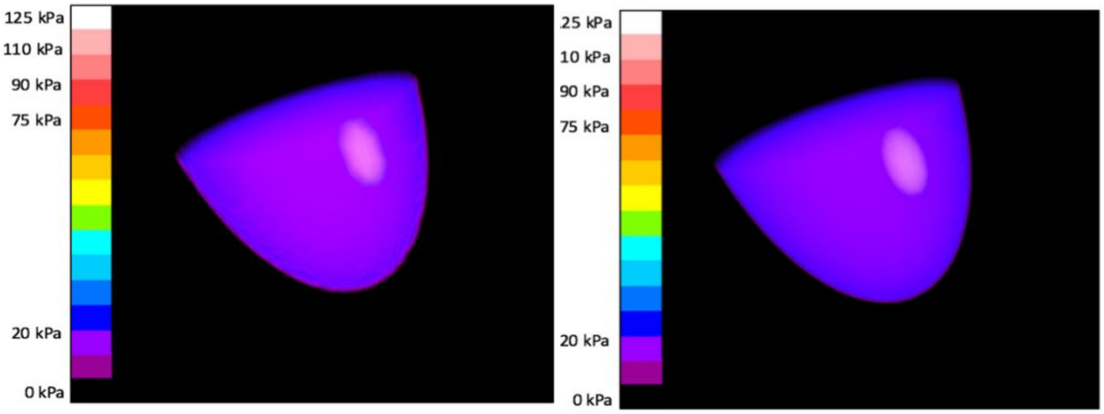

(a) (b)

Figure 2-6: Volume rendered comparison of a medium IDC in quadrant II within the (a) lower and (b) higher resolution hemisphere.

2.3.2 A priori information.

Two different initial guess distributions of elasticity values were investigated. The first required no *a priori* information about the underlying anatomy—the initial guess was set to a homogeneous elasticity value of 10 kPa. In the second case, *a priori* information was developed to be indicative of representative HU values that would come from the prone/supine CT scans taken in the clinic.

Table 2-4: Table showing average values for low (64 voxel diameter) and high (128 voxel diameter) resolution hemispheres, both with and without a priori information.

Hemisphere Size	**Elasticity Window**		**Displacement Error**	**Average Time**
Averages	$\pm \mathbf{1}\ \boldsymbol{kPa}$ (%)	$\pm \mathbf{5}\ \boldsymbol{kPa}$ (%)	$< \mathbf{1}\ \boldsymbol{mm}$(%)	**(s)**
64 voxel mean	89.76 ± 1.12	96.40 ± 4.73	98.67 ± 3.62	272.50 ± 236.12
64 voxel with a priori mean	94.27 ± 6.38	97.43 ± 3.37	99.07 ± 1.08	218.06 ± 216.17
128 voxel mean	85.43 ± 4.37	97.89 ± 2.33	94.94 ± 4.09	3345.38 ± 1618.00
128 voxel with a priori mean	86.87 ± 3.23	98.87± 2.52	97.44± 2.17	1595.69 ± 1012.2

Each ground-truth elasticity distribution was investigated starting with both types of initial guess. Table 2-2 shows the results averaged over every distribution both with and without the *a priori* initial guess. It can be seen that the *a priori* information increased the elasticity and displacement accuracy overall. Table 2-4 shows a further breakdown of these results in terms of image resolution along with the average time.

Average time decreased appreciably, especially for the higher resolution hemisphere with 128 voxel diameter where the average time decreased by about 30 minutes. Overall, both accuracy and computation time improved notably between simulations run with the homogenous initial guess and the *a priori* initial guess, which is also illustrated in Figure 2-7 for a random selection of ground-truth distributions.

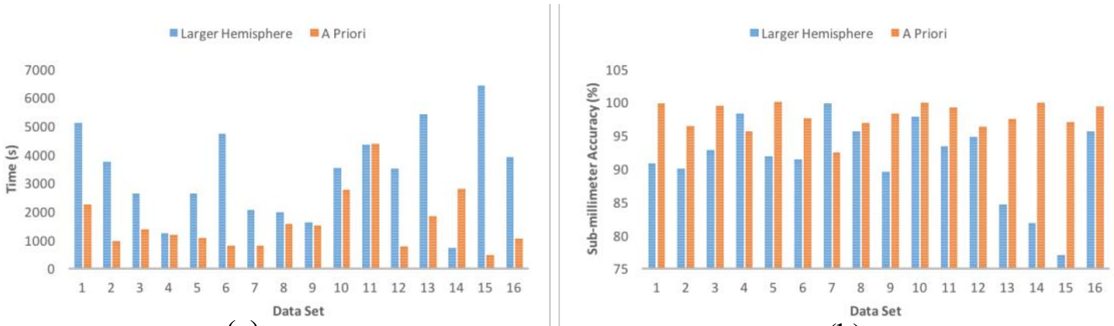

(a) (b)

Figure 2-7: (a) shows a time comparison for distributions with and without a priori information for random distributions, while (b) shows an accuracy comparison for the same datasets.

Figure 2-8 shows volume renderings of the ground-truth elasticity distribution (a), the resultant elasticity distribution when no *a priori* information was considered (b), and the resultant elasticity distribution when *a priori* information was used to form an initial guess (c) for a large IDC in Quadrant I. Visually, it can be seen that Figure 2-8(c) more closely matches the ground-truth distribution, without the distortion along the chest-wall and boundary distortions seen in Figure 2-8(b). When the *a priori* information was not utilized, as in Figure 2-8(b), the magnitude discrepancies and edge distortions are clear, which both agrees with, and thus strengthens, our numerical results.

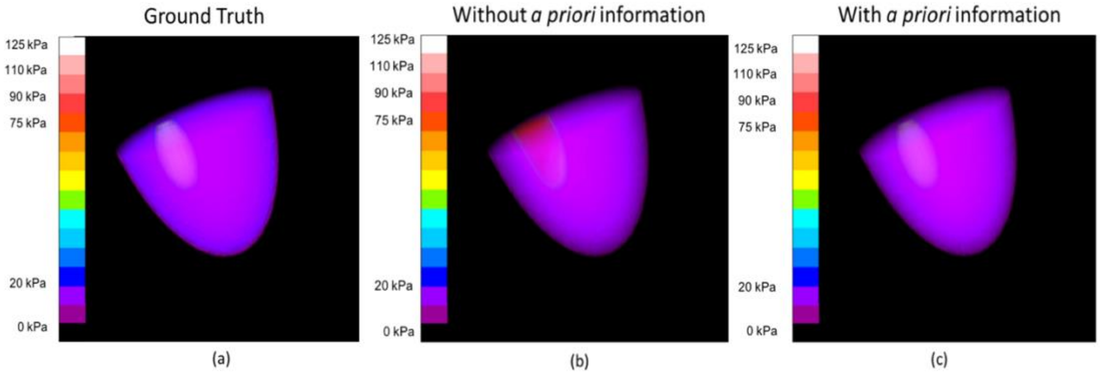

Figure 2-8: Volume renderings of small IDC located in Quadrant II. Part (a) shows the ground-truth distribution, (b) shows the reconstruction with a random initial guess, and (c) shows the reconstruction using a priori information to make an informed initial guess

Table 2-5 shows excerpts of the individual results for a large IDC in Quadrant II, a small fibroid in Quadrant I, and a medium DCIS in Quadrant III. These results are selected to illustrate that regardless of tumor type, location, or size, the addition of *a priori* information significantly improves the results. This is further illustrated when considering the statistical significance of the average accuracy values. When *a priori* information was used to form an initial guess, the average displacement accuracy for the lower and higher resolution hemispheres increased respectively from 94.94% and 98.67% to 97.44% and 99.07%. A two-sample t-test between 20 different distributions confirmed that the improvements resulting from the use of *a priori* information were significant ($P < 0.05$). These results suggest that taking advantage of *a priori* HU data obtained from the clinical CT scans can reduce the convergence time of our simulation while improving the accuracy of the resulting elastic distribution.

Table 2-5: Example of individual cases with and without a priori information for a large IDC in quadrant II, a small fibroid in quadrant I, and a medium DCIS in quadrant III.

	Elasticity Window		**Displacement Error**	
Large IDC Quadrant II	$\pm\mathbf{1}\ \boldsymbol{kPa}$ (%)	$\pm\mathbf{5}\ \boldsymbol{kPa}$ (%)	$<\mathbf{1}\ \boldsymbol{mm}$ (%)	$<\mathbf{3}\ \boldsymbol{mm}$ (%)
Without a priori	86.43	97.68	88.30	100.00
With a priori	96.90	98.25	100.00	100.00
Small Fibroid Quadrant I	$\pm\mathbf{1}\ \boldsymbol{kPa}$ (%)	$\pm\mathbf{5}\ \boldsymbol{kPa}$ (%)	$<\mathbf{1}\ \boldsymbol{mm}$ (%)	$<\mathbf{3}\ \boldsymbol{mm}$ (%)
Without a priori	72.20	99.62	90.02	100.00
With a priori	81.24	99.64	96.47	100.00
Medium DCIS Quadrant III	$\pm\mathbf{1}\ \boldsymbol{kPa}$ (%)	$\pm\mathbf{5}\ \boldsymbol{kPa}$ (%)	$<\mathbf{1}\ \boldsymbol{mm}$ (%)	$<\mathbf{3}\ \boldsymbol{m}$ (%)
Without a priori	80.86	92.29	68.38	100.00
With a priori	91.20	99.03	95.49	100.00

2.3.3 Fast-simulated annealing.

For ground-truth displacement distributions, the ground-truth elasticity distribution was prescribed and the ground-truth iteration number was set to 4000 iteration steps to allow the breast simulation adequate time to deform. The ground truth iteration number was set to 4000 to allow the breast simulation adequate time to deform. The deformation of the particles was recorded for multiple iteration numbers, and at an iteration number of 4000, the maximum deformation increased by less than 0.01 mm, or 1% of our convergence criteria, indicating that the simulation had reached a state of equilibrium within 4000 iteration steps.

The FSA algorithm returned an average iteration number value of 2960 ± 590 iteration steps. The small discrepancy between this result and the ground-truth iteration number occurs because the combination of iterative binary search and the FSA algorithm allows for multiple solutions. More relevant is the resulting displacement and elasticity accuracy for the simulation run both with and without the FSA algorithm. Table 2.2 lists the resulting estimations of average elasticity and displacement accuracy for the distributions computed both with and without the FSA algorithm.

The sub-millimeter convergence percentage of each instance (i.e. with and without FSA) was observed to be 97.45% and 98.78% respectively. A two-sample t-test of 20 different distributions indicated that the difference between the mean values of each population was not significant ($P > 0.05$), therefore use of the FSA algorithm allowed the iterative estimation process to converge correctly without reducing the integrity of the results. Figure 2-9 shows volume rendered elasticity distributions of the ground-truth (a) and estimated distributions with and without use of the FSA algorithm for a large IDC located in the center of the hemisphere (b & c). It can be seen that both instances (b&c) result in a very similar volume rendering, where the location of the IDC is located accurately with some small discrepancies around the boundary of the tumor. From the numerical and visual results, we can conclude that use of the FSA algorithm allows our simulation to converge correctly. This will allow for us to more easily transition to clinical data—we will not have any preconceived notions of iteration number yet we can still expect our simulation to determine accurate results.

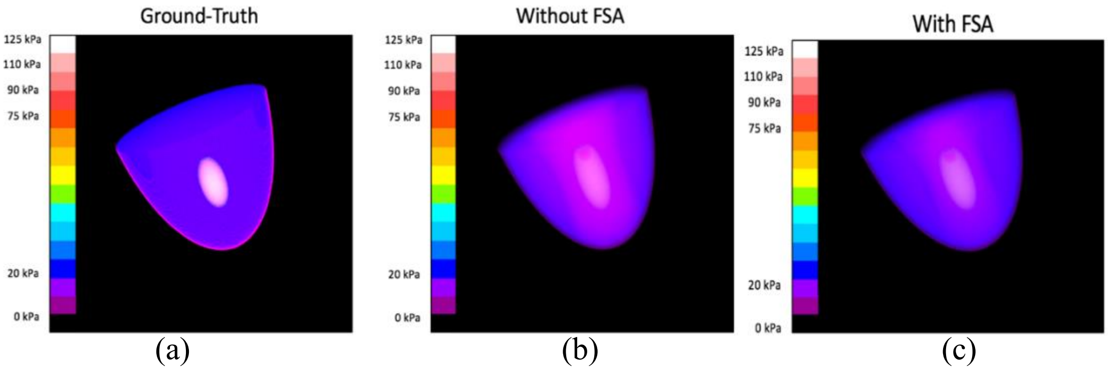

(a) (b) (c)

Figure 2-9: Volume rendering of a large IDC located in the center of hemisphere. Part (a) shows the ground-truth distribution, (b) shows the reconstruction without the use of the FSA algorithm, and (c) shows the reconstruction using the FSA algorithm.

Comparing Figures 2-8(b) and 2-9(b), it can be seen that elasticity was reconstructed with similar discrepancies in each case, indicating that tumor location does not obstruct our elasticity reconstruction. The use of *a priori* information, however, greatly impacted the resultant distribution, as shown in Figure 2-8(c). A minor fact to note is that the Figure 2-9(a) is also much "brighter" than Figure 2-8(a)—because the tumor was located in the center instead of the upper back quadrant, the window/level of the volume reconstruction did not have to be changed in order to see it.

Overall, our simulation converged with about 97% sub-millimeter accuracy. Though the errors were minimal, the largest elastic moduli discrepancies were seen around the boundary of the simulated tumors, and the largest displacement errors were seen both around the boundary of the tumor and the edge of the hemisphere. The use of *a priori* information greatly improved our results, while both use of the FSA algorithm and image resolution size do not affect the accuracy of our results. Tumor location also does not affect the accuracy of our outcome. The implications of these results are further discussed in the following section.

2.4 Discussion

In this work, a methodology for performing breast elasticity estimation using deformation resulting from the transition between supine and prone patient postures was presented. The procedure was developed and systematically assessed using a biomechanical simulation representing a breast in the prone position with a spherical tumor located within the breast. In order to investigate the accuracy and robustness of the approach for any given scenario, the synthetic tumors were given elasticity values from the literature used to represent three different common breast tumors: ductal carcinoma's in-situ, invasive ductal carcinomas, and fibroadenomas, and were positioned with different sizes throughout the breast tissue.

The biomechanical breast simulation was based on a physics-based approach. This choice was motivated by the previously shown accuracy of the approach for head and neck applications that were readily transferrable to the breast [52]. In addition, this model was validated for simulating motion caused by gravity, and the supine-to-prone deformation is known to be gravity-induced [5, 23, 24]. The implementation of this approach in a GPU environment enabled a high-resolution biomechanical simulation in nearly real-time. Inversing the forward deformation model allowed us to obtain elasticity maps for patient-specific biomechanical models that will be useful for reducing positioning errors in adaptive radiotherapy. Using the well-validated constitutive model previously used for head and neck allowed us to purely focus on the accuracy and feasibility of the inverse analysis, rather than the model's accuracy in regards to simulating gravity induced deformations. While the usage of such a GPU-based, biomechanical model has been recently validated for head and neck tissues, future studies will focus on the usage of such a model for breast tissue, which needs to be clinically validated using an extensive patient study. Model errors in such studies typically stem either from tissue elasticity estimation errors or from the model's inability to represent the complex anatomical deformation. Having shown in this study that the tissue elasticity estimation errors will be minimal for this biomechanical model, future work will focus on a clinical study to enumerate the model's ability to quantitatively represent the anatomy. While most deformable modeling efforts may be insensitive to soft tissue elasticity data, our approach has a direct relationship with the properties of soft tissue since it relies on the supine-to-prone breast deformation, which is driven by gravity. The ground-truth displacements required for our methodology depend on the ability to register prone and supine breast images with a one-to-one correspondence. Due to the large deformation induced to the breast tissue, image registration between these postures is a challenging problem. Various deformable image registration algorithms have been investigated by peers specifically for the prone-to-supine breast transition [33-35]. Future work will focus on further investigating a deformable image registration technique that provides accurate ground-truth data and a one-to-one correspondence between breast tissue in the prone and supine positions.

In our approach, we have employed a linear elastic deformation model to deform the breast anatomy from supine to prone patient posture. Such a deformation may be large enough to cite a need for hyperelastic model to represent the tissue behavior. Our future work will focus on extending the method to a hyperelastic regime. Such an analysis will require more patient postures to be imaged.

The iterative binary search optimization algorithm, along with the FSA algorithm, allowed for the estimation of elastic properties for the biomechanical model based upon the deformation of each mass element. The performance of the algorithm was confirmed with the high elasticity and displacement accuracy that was achieved. The iterative optimization algorithm allowed each mass element to converge individually, so that even tumors with diameters as small as 5 mm were located accurately. While our simulation study used a simplified framework that modeled tumors spherically, the per voxel approach of our inverse analysis should allow sufficient delineation of irregular tumors shapes as well. We believe the algorithm has potential to recognize other items of interest that may be located within the breast that were not investigated here. Future work will investigate the accuracy of our approach for irregular tumor shapes and sizes, as well as for irregular breast shapes.

Our results showed that an accuracy of 98% was achieved in estimating the ground truth elasticity. Because of the per-voxel nature of our approach, variations in the size of the tumor and the breast geometry had negligible impact on the accuracy of the estimation process. Our analysis indicated that the elasticity can be successfully reconstructed for tumors with a diameter as small as 5 mm and as large as 1.5 cm within the breast tissue. Changes in image resolution and geometry size showed no significant impact on the resulting accuracy, indicating that the CT image resolution should not influence the resulting elasticity estimation. The geometry size alternatives also indicated that the biomechanical simulation successfully represented different breast sizes.

The elasticity information that we obtain through this methodology will be used to design a new immobilization device specifically for precise and reproducible breast positioning. Ideal breast geometry for radiotherapy is similar to that achieved in the prone orientation, without the discomfort and associated normal tissue doses [36]. With the robotic assistance of an immobilization device, this ideal position can be achieved in a more comfortable, supine orientation. Our high-resolution, physics-based breast model will act as a control module for such a robotic system, simulating patient-specific breast geometry and its deformation when interacting with the robotic system [3]. Future work will focus on improving the breast simulation to more realistically simulate the breast anatomy, eventually progressing to patient data. We believe this methodology can also be readily transitioned to other anatomies such as the lung, liver, and head and neck for radiotherapy applications.

Because of the imaging techniques within current radiotherapy workflows, our current methodology uses DICOM CT images to construct the biomechanical model. Future work will focus on expanding this methodology to be coupled with US and MR measurements to further improve the model-guided elasticity estimation process. Evolutionary algorithms will be investigated and their functionality compared to that of the FSA and binary search algorithms. These efforts are crucial in order to apply the methodology in clinical radiotherapy practice.

2.5 Conclusion

In this chapter, we presented a systematic study of a novel GPU-based inverse analysis methodology for breast tissues using supine/prone CT image datasets. The methodology was investigated using a forward model, GPU-based, physics-based breast simulation that was iteratively deformed to represent the deformation of the breast between supine and prone orientations. The inverse analysis consisted of a gradient-based binary search optimization scheme that, coupled with a fast-simulated annealing algorithm, updated the spatial elasticity distribution of the breast tissue. Our analysis showed that the methodology enables a 97% accuracy in elasticity estimation of homogeneous breast tissue and an embedded tumor with regards to our novel error metric only using the two postures. These results indicate that our methodology has the potential be readily applied with great accuracy to advance breast positioning techniques in clinical radiotherapy practice. In the following chapters, the elasticity estimation methodology will be expanded into the lung and liver anatomies.

CHAPTER 3: PERFORM SYSTEMATIC STUDIES USING VIRTUAL ANATOMICAL PHANTOMS AND A BIOMECHANICAL MODEL TO ASSESS THE FEASIBILITY OF OBTAINING TISSUE ELASTICITY INFORMATION FROM BREATHING-INDUCED DEFORMATION DATA.

Feasibility and quantitative analysis of a biomechanical model-guided lung elastography for radiotherapy

A version of this chapter has been published as a manuscript: BPEX, Vol. 3, No. 2, 025006, 2017. doi: 10.1088/2057-1976/aa5d1c

3.1 Introduction

Radiation therapy is a clinical procedure that is commonly used to treat lung cancer, the leading cancer killer of men and women in the U.S. [53, 54]. With the increasing focus on hypo-fractionated therapy [55] and improving patient quality of life [56], there is a greater need to spare the normal lung regions and more precisely target the lung tumor. This requires an ability to precisely distinguish the regions inside the lung that function normally from those regions that are diseased.

Measurement of lung tissue elasticity, or elastography, within a radiotherapy workflow forms the focus of this study. Currently, common lung radiotherapy imaging protocols require the acquisition of 4DCT images for treatment planning to account for the lung tumor motion [43]. The focus of this chapter is to formulate a methodology to perform lung elastography using only deformation information that would be available from 4DCT data acquired during radiotherapy treatment planning, and to systematically validate and quantify the feasibility and accuracy of this methodology. In our lung elastography process, we focus on the identification of the Young's modulus (E) for each voxel using displacement fields. Our approach formulates lung elastography as an inverse problem that is solved using an iterative optimization of physics-based model parameters. The advantage of this approach to lung elastography is that the forward model is formulated from well-established physical laws that relate biomechanical properties to measured mechanical response [20]. From a clinical perspective, the approach is applicable for radiotherapy as no additional imaging is required for the lung elastography process. Other co-existing disease states, such as COPD, can also be precisely characterized at a voxel-by-voxel level and can further improve radiotherapy treatment plans. In addition, the accuracy of the lung elastography measurements presented in this study enables the information to be used for tasks such as the normal tissue sparing treatment planning [57].

Another key aspect of our approach is the usage of virtual lung phantoms for systematically quantifying the elastography accuracy. The need for such virtual lung phantoms stem from the fact that estimating a heterogeneous elasticity distribution is a multi-local minima problem; i.e., different elasticity distributions may end up providing the same displacement. Thus, for an elastography to be clinically applicable, we need to quantify the measured elasticity's accuracy explicitly in addition to comparing the voxel displacements. The usage of virtual phantoms also enables us to systematically assess the estimation accuracy for variations in the tissue elasticity, boundary conditions (the range of motion in the other organs), and CT image noise.

3.2 Methods

The primary aim of this study was to devise a methodology to estimate the Young's modulus (denoted by *E*) associated with each lung tissue voxel, and systematically assess and quantify the accuracy of the estimation. A systematic study is necessary to assess the feasibility of this approach since ground-truth Young's modulus values are not known for deformation values obtained from clinical 4D datasets. We formulated the inverse elasticity problem as a parameter-optimization problem, with an objective to determine the elasticity parameter that will minimize the difference between ground-truth displacement and that computed by the biomechanical model. In clinical implementations, the ground-truth displacement will be determined from deformable image registration techniques of 4DCT lung images, but for the purposes of our study, it is determined by the forward model described below. The inverse elasticity problem was solved by implementing a gradient descent optimization algorithm coupled with a novel convergence magnification approach that enables a high precision elasticity estimation. In our approach, we define the convergence criteria as the specific criteria, which the simulated deformation needs to meet in order for the underlying elasticity to be accepted as the lung's accurate elasticity. For our purposes, convergence occurred when 95% of the voxels were within 0.5 mm of the ground-truth displacement. This will be further explained in section 3.

The constitutive forward model used for this section was presented in §2.2.1, and the inverse analysis used in the iterative reconstruction was presented in §2.2.2. For brevity, here we will only present the updates to the algorithm that were used to transition from the breast to the lung anatomies.

In this section, we first present the constitutive forward model (§3.2.1; previously described in §2.2.1) to solve the inverse elasticity problem. Next, we present the inverse analysis used in the iterative reconstruction (§3.2.2; previously described in §2.2.2). Finally, we present the novel locally heterogeneous convergence magnification method (§3.2.3).

3.2.1 Forward model

From a physiological perspective, the lung, diaphragm, and the rib-cage deform during inhalation and exhalation, causing air to flow in and out and the lung to expand [58]. Modeling the lung deformation involves taking the diaphragm and rib-cage expansion as input and computing the lung anatomy's expansion and contraction for the subsequent airflow [59]. The forward model presented here is focused on computing the lung tissue deformation for a given lung surface displacement that corresponds to a given lung elasticity distribution [59]. The forward model utilized in this methodology has been previously described in [52, 60] and specifically for lungs in [61]. For clarity purposes, a brief description of the constitutive equations for the forward model [52] is presented here.

3.2.1.1 Model initialization and geometry. The biomechanical model of the lungs was constructed from clinically acquired source images as described in §2.2.1.1. The model geometry was represented by finite mass element nodes corresponding to the center of each voxel of anatomy in the CT image, and neighboring elements were connected to each other with linear elastic connections to ensure the mass elements could deform in a physically realistic manner. As patients are expected to breathe normally within a clinical radiotherapy setup, a locally heterogeneous distribution of linear elastic material properties and a Poisson's ratio of 0.43 was used for this study [62-64]. Linear elastic constitutive laws were utilized because recent publications have found that linear elastic representations have been effective in describing normal lung tissue deformations typically observed in a 4DCT based lung motion [65]. Additionally, the effect of non-linear elastic properties are only significant at remote locations within the lung where the diaphragm-induced motion is most significantly attenuated [66]. Furthermore, a study investigating lung tumor motion during external beam radiotherapy found that a hyperelastic constitutive model performs very similarly to the linear elastic constitutive law at the deformation magnitudes found within the lungs during normal breathing [67].

3.2.1.2 Forward deformation computation. The forward deformation computation used in our approach has been previously described in §2.2.1.2. In our approach, we employ Hooke's law as the constitutive equation, with the tissue elasticity represented by the Young's modulus. The corrective forces on each mass element were calculated as a summation of tensile, shear, and a dashpot damping forces. Initially, the elastic internal corrective forces were set to zero; when deformed, the model's mass elements were relocated to new positions inside the deformation space, causing the internal corrective forces to be non-zero.

As the material is assumed to be linear, displacement is inversely related to the elastic modulus of the material—for a constant force, if elastic modulus increases then displacement must decrease and vice versa. Once the model reached a deformed state of equilibrium, the 3D Euclidean distance between initial and current positions (described in Equation (2-3)) for each mass element was taken to be the displacement for that mass element, denoted henceforth as d_a, and then the biomechanical model was reset to the initial un-deformed position. The forward model is implemented in a graphics processing unit (GPU) environment to allow for fast and accurate computations.

3.2.1.3 Boundary constraints. In our approach, we formulated the diaphragm and rib-cage movements as boundary constraints for the lung deformation. Since the pleural cavity between the lung and the boundary constraints forms a hydrostatic seal, we translate the lung surface's displacement as the constraint for the lung tissue's elasticity estimation. The surface motion for each voxel of each section of the lung (i.e. apex, middle, or base) was constrained to values suggested from the literature [68, 69] and will be investigated further in this study. The maximum boundary motion was 2 – 16 mm depending on the lung section, and the strain was applied at a rate of 5 – 35 min^{-1}.

3.2.2 Inverse problem

Solving the inverse elasticity problem was carried out in two steps: 1) estimating the displacement field from every voxel of pre- and post-displaced tissue for a given elasticity distribution, and 2) optimizing the elasticity distribution that best reproduces the observed displacement field [70]. In the first step, for simplicity, we simulated the surface deformation of the lungs by deforming the boundary of the lung outward from rest state. Lung tissue, an elastic material, was viewed as a series of finite mass elements connected by a grid of ideal, linear elastic connections. The boundary voxels were deformed according to §2.1.3, while the interior voxels were allowed to deform according to the elastic forces within the model. The deformation process was previously described in §2.1.2.

The iterative scheme for recovering the spatial-elastic distribution was derived from the inverse relationship between Young's modulus and displacement, as described in Equation (2.2) above [71]. The general basis of our reconstruction technique was to minimize the difference between ground-truth and calculated displacements. Given an initial Young's modulus distribution, the biomechanical forward model provided theoretical estimates of mass element displacements. These displacements were then compared with ground-truth displacement vectors, and the Young's modulus distribution was iteratively updated until the error was minimized. Intermittent mass element displacements were generated on a per voxel basis by updating the Young's modulus values as described below. The initial (E_a), minimum ($E_{min,a}$), and maximum ($E_{max,a}$) Young's modulus values were initialized for each voxel, a, in the physics-based biomechanical model. For lung elastography purposes, the Young's modulus range is set to be from 1 kPa to 20 kPa, an extended approximation of values from the literature [72].

The reconstruction process (Equations (2-5 – 2-8)) was repeated until a suitable stopping criterion was reached. For our purposes, reconstruction was terminated after 30 iterations or when 95% of the voxels in the biomechanical model had a displacement differential that was less than 0.5 mm.

3.2.3 Locally heterogeneous convergence magnification

The inherently subtle tissue motion of different parts of the lungs results in deformation vectors that are impractical for use in conventional model-guided tissue elastography. Deformation values at small values of strain carry little to no information about the non-homogeneous elasticity parameter [73]. Because of the relatively small boundary motion, the displacement magnitude, and thus displacement differential, of each voxel of lung tissue is well within the convergence criteria regardless of the trial elasticity solution [74, 75]. In order to adjust the reconstruction methodology to be more sensitive to subtle changes, a locally heterogeneous convergence magnification technique was formulated as follows.

Let i represent the index of a reference voxel, $G(i)$ represent the position of voxel i in the ground-truth 3D model, and $P(i)$ represent the model generated position of the reference voxel. The convergence criteria can be defined as:

$$\| |P(i)| - |G(i)| \| < \epsilon, \tag{3-1}$$

where ϵ is defined to be the error tolerance in mm. For the gradient descent approach to accurately compute the elasticity, two constraints need to be met. First, the convergence discussed in Equation (3-1) needs to be satisfied for all voxels. Second, the difference in the convergence of each voxel needs to be locally heterogeneous. The convergence criteria (Equation (3-1)) does not reflect this local heterogeneity. To incorporate it, we formulated the convergence criteria as follows.

Let I represent all of the voxels in the ground-truth 3D model and J represent all of the voxels in the model-generated target anatomy. Let M represent a function that biomechanically deforms a given anatomy by a given force, denoted as $M\left(I, i\,, \vec{f}_{\eta\subset I}\,, E'\right)$ to include all voxels I, an applied force $\vec{f}_{\eta\subset I}$ to a subset of voxels η in I (which will be used to enforce local heterogeneity), and a prescribed generic elasticity E' that will remain the same throughout the entire process so that the added deformation is known. Now, Equation (3-1) can be rewritten as

$$\|\left(\left|M\left(J, P(\,i), \vec{f}_{\eta\subset I}, E'\right)\right| - \left|M\left(I, G(\,i), \vec{f}_{\eta\subset I}, E'\right)\right|\right)\| < \epsilon, \qquad \textbf{(3-2)}$$

where $\|M\left(\mathrm{J}, \mathrm{P}(\,i), \vec{f}_{\eta\subset I}, E'\right)\|$ denotes the magnitude of the model-generated deformation. This novel depiction of the convergence criteria now includes not only the i^{th} voxel position, but also the local neighborhood determined by I for the ground-truth and J for the deformed model and the amplified displacement discrepancies determined by the applied force $\vec{f}_{\eta\subset I}$ and the pre-assigned arbitrary elasticity E', that is separate from the elasticity parameters being estimated from the inversion process. In this study, we define M in a physics-based manner using the same lung boundary constraints and the implicit elasticity forces as employed for the estimation process. The applied force $\vec{f}_{\eta\subset I}$ is set to be a unidirectional force that deforms a specific subset of the lung tissue voxels in a specific direction according to the elastic forces in the model derived from E'. The value of E' is set to be 30 kPa so that the magnitude of the force is about 9.8 $\frac{g\cdot m}{s^2}$ and creates significant strain in every voxel.

The applied force will unevenly magnify the voxel deformations, so that some voxels will be more sensitive to convergence than others. This locally heterogeneous magnification is useful because it amplifies voxel deformation along the force direction enough to allow some voxels to converge correctly. The resulting voxel displacements range from 4-25 mm depending on the location of the voxel and the directionality of the force. The entire process is repeated with the unidirectional force being applied in different directions, which will allow a different subset (η) of voxels to converge each time. The resultant elasticity distribution is then taken to be a union of the elasticity estimation subsets such that all voxels are accounted for.

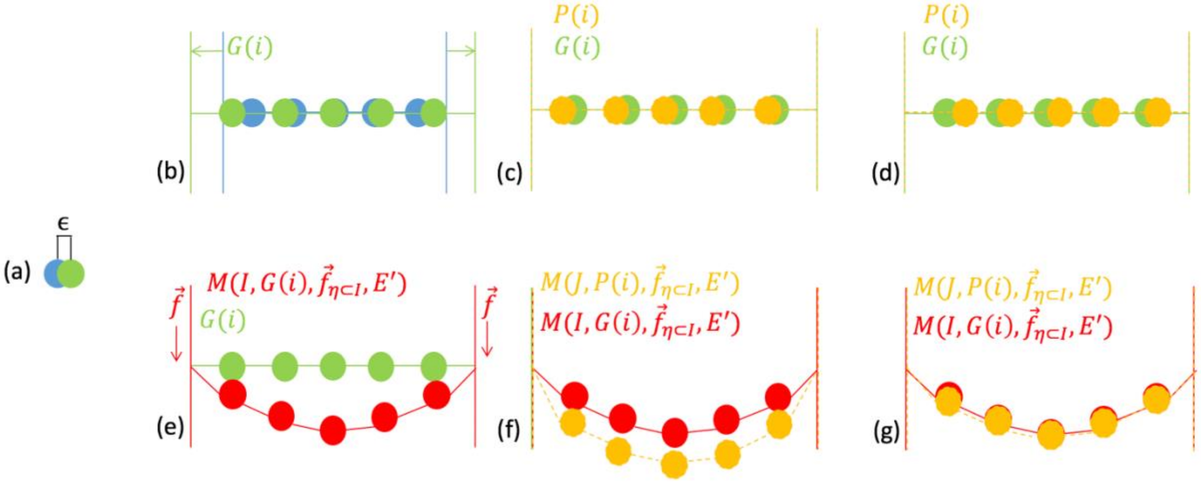

Figure 3-1. Simple geometrical illustration of novel convergence methodology. (a) shows sample convergence tolerance, (b) shows the undeformed geometry in blue and deformed geometry in green. (c) and (d) show sample reconstructions. (e) again shows the conventional deformation in green, and heterogeneous induced deformation in red. (f) and (g) show sample reconstructions, illustrating the magnification of small differences with our novel technique.

Figure 3-1 illustrates an example application of this novel convergence methodology using a simple geometry of 5 particles connected to a boundary. Figure 3-1(a) illustrates an example tolerance, ϵ. Figure 3-1(b) illustrates the undeformed state, in blue, and the model after it has been deformed with the lung boundary constraints, $G(i)$, in green. It can be seen that the difference in position of most of undeformed and deformed particles is less than ϵ. Figure 3-1(c & d) show two different example model constructed deformations, $P(i)$, in orange, both of which will converge to satisfy Equation (3-1) as they are less than ϵ as well. It can be seen that the formulation is not sensitive to small deformations. Figure 3-1(e) shows the conventionally deformed particles $(G(i))$ in green, and the amplified differences introduced by $M\left(I, G(i), \vec{f}_{\eta \subset I}, E'\right)$ in red. Because of the amplified differences induced with a unidirectional force over all particles in the z-direction, the example reconstructed deformation, $M\left(J, P(\ i), \vec{f}_{\eta \subset I}, E'\right)$ shown in orange in Figure 3-1(f) will not converge under Equation (3-2), while Figure 3-1(g) will converge. It can be seen that using Equation (3-2), the small differences can be significantly magnified in an locally heterogeneous manner. Such a process enables a smoother and faster estimation of elasticity.

To summarize, the inverse analysis, facilitated by the physics-based biomechanical model and novel locally heterogeneous convergence magnification approach is applied according to the following steps: Intermediate elasticity values are assigned to each voxel of the biomechanical model. The boundary of the lung is deformed outward. The inner voxels are allowed to deform and reach a state of equilibrium. To facilitate convergence and increase conditioning of the system, a prescribed unidirectional force is applied to the inner voxels of the lungs. The elasticity distribution is iteratively updated and new model deformations are obtained. This process is repeated until Equation (3-2) is satisfied and convergence occurs, as shown in Figure 3-2 below. Once the algorithm has converged with the initial unidirectional force, the biomechanical simulation is then run with the magnification force applied in another direction in order to induce different local heterogeneity and convergence. The union is then taken between the resultant elasticity distributions for the different forces and the elasticity value corresponding to the lowest displacement error is taken to be the optimal value.

3.3 Quantitative Analysis

It is important to quantify the accuracy with which the elasticity estimation method presented can be performed using deformation data that would be easily obtained 4DCT datasets. From a mechanics perspective, it is known that multiple distinct heterogeneous elasticity maps can result in the same displacement distribution [76]. So a direct usage of clinical datasets will not provide a full quantitative analysis. In addition, inverting a forward model with a heterogeneous elasticity distribution is not a straightforward problem [77, 78]. Variations in the elasticity, boundary constraints, and image noise may lead to a lowered accuracy. To address this issue and enable a systematic study of the application of our methodology for lung elastography, a physics-based lung model with known tissue elasticity was employed to generate a virtual lung phantom [65].

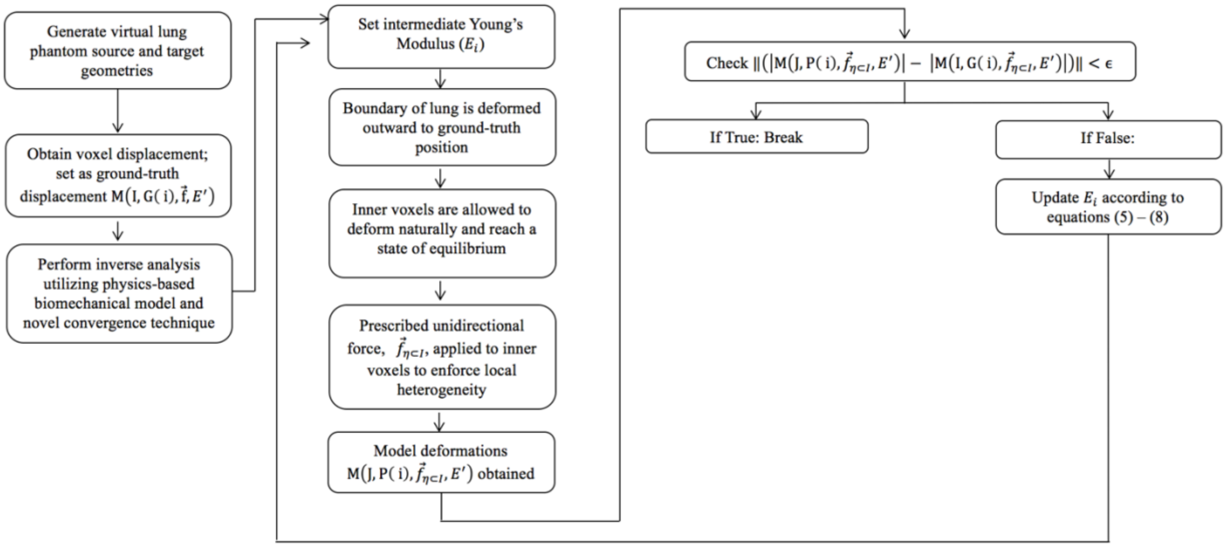

Figure 3-2: Flow chart depicting locally heterogeneous convergence magnification approach within elasticity reconstruction algorithm.

3.3.1 Virtual lung phantom

The virtual lung phantom geometry was obtained from anonymized lung CT geometry of both a right and left lung. Each lung phantom voxel was assigned a normal ground-truth Young's modulus based upon the HU value of the source CT, with elasticity values ranging between 1 and 20 kPa—an extended approximation of the range of elastic modulus values for normal and fibrotic lung tissue [79, 80]. This resulted in a locally heterogeneous elasticity distribution, which was further modified to represent different diseased tissue that might be seen in lung radiotherapy cases. The virtual lung phantom was deformed from the initial source geometry to a target geometry based on the prescribed boundary constraints. Two different forward models were used to displace the virtual lung phantom: an elastostatic Green's function model and the well-validated elastodynamic model used in the inversion process. The displacement of each voxel of the virtual lung phantom was taken to be the ground-truth displacement. Figure 3-2 summarizes the entire experimental process, from the development of the virtual lung phantom to the inverse analysis.

3.3.2 Experimental process

To enable a systematic study of the lung elastography methodology, the virtual lung phantom source datasets were segmented into 25 slice sections of the apical, middle, and basal regions, each slice with a resolution of 145x179 pixels. Each of the six sectioned lung regions (right apex, right middle, right base, left apex, left middle, and left base) were simulated using the physics-based biomechanical model and analyzed to evaluate the effect of geometry on the convergence of our methodology..

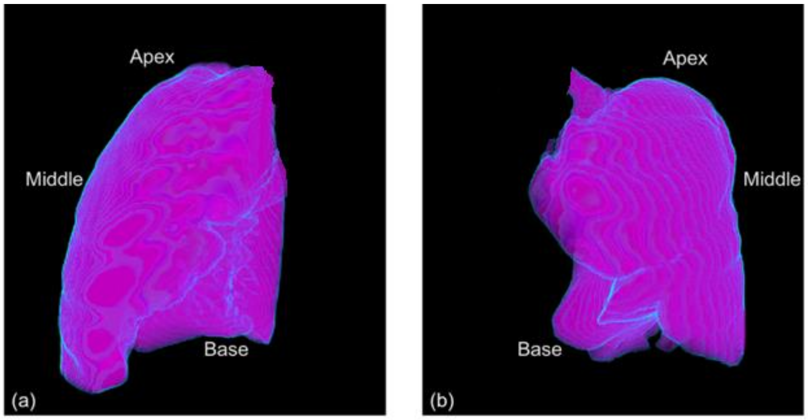

Figure 3-3: Volume rendering of left (a) and right (b) simulated geometry of the lungs used in systematic study. Approximate apex, middle, and base sections are labeled.

Figure 3-3 illustrates volume renderings of the left (a) and right (b) physics-based biomechanical lung models that were used to analyze the geometrical dependencies of our high precision lung elastography methodology. The approximate locations of the 25-slice apex, middle, and base sections of each lung are also labeled for clarity

To begin the systematic study, homogenous initial elasticity values were applied to the physics-based biomechanical lung model. Ground-truth boundary deformation values were applied to the surface voxels of the biomechanical lung model. The inner voxels were allowed to deform according to the elastic forces within the model. The steady-state displacements were then magnified. Finally, the resulting deformation and reconstructed elasticity distributions were compared to the ground-truth numbers on a voxel-by-voxel basis. Along with average results, we sought to examine four other criteria: (a) accuracy improvement due to use of locally heterogeneous convergence magnification, (b) accuracy deviations due to relevant model variations, (c) relation between ground-truth elastic distribution and accuracy, and (d) relation between boundary expansion magnitude and accuracy. The following experiments describe the approaches used to examine criteria (a) – (d).

3.3.2.1 Experiment 1: Assessing the locally heterogeneous convergence. To assess the function and necessity of this novel convergence criteria, the elasticity estimation was first performed using our conventional methodology (Equation (3-1)) with ϵ set to a small value of 0.5 μm to see the effects of reducing ϵ to magnify displacement differences._Such a value of ϵ also acts as a global magnifier of the displacement convergence. Then, the locally heterogeneous convergence technique (Equation (3-2)) was utilized and the accuracy improvements were evaluated and quantitated for a small ϵ value of 0.5 mm. For simplicity, in this study, the locally heterogeneous convergence technique is performed twice for each case that is considered: once with $\vec{f}$ in the z- and once with $\vec{f}$ applied at a 45 degree angle between the x- and y-axes (referred to as the xy-direction). The force that provided the least displacement error was taken to be optimal for each voxel. If these accuracy improvements were significant, the results would indicate the need for the, locally heterogeneous convergence technique to garner useful elasticity information from clinical lung deformation values.

<u>3.3.2.2 Experiment 2: Assessing estimation accuracy for forward model variations.</u> To assess the robustness of our methodology, two variations on the forward model were used to compute ground-truth displacement values. The conventional ground-truth displacement was taken from an elastodynamic forward model, previously well-validated in [52], in which the virtual lung phantom was deformed for 5000 timesteps. Secondly, an elastostatic forward model based on Green's function [61] was also used to compute ground-truth displacement.

Finally, to further validate the robustness of the model, random noise within ± 5% (± 45 HU) was added to the source images investigated for both the elastodynamic and elastostatic forward models used in this study. It has been shown that noise on clinical lung images generally averages around 30 HU [81], so excessive noise was added for further validation. The original and "noisy" source images are shown below in Figure 3-4. Virtual phantoms were then generated for these "noisy" geometry and the resulting image pairs were then deformably registered using an in-house registration algorithm. The resulting volumetric displacement was then used for estimating the elasticity.

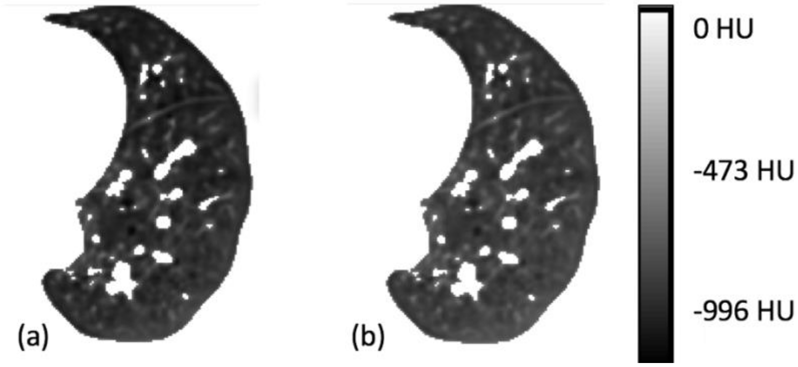

Figure 3-4: 2-D slices of base of left lung showing original (a) and "noisy" (b) source images

Reconstructed displacements computed using the elastodynamic forward model were then compared to each set of ground-truth displacement values mentioned above. If accurate elasticity estimations can obtained for forward model variations, it can be inferred that the elasticity estimation algorithm can be extended for use with clinical 4DCT datasets that has a similar noise.

3.3.2.3 Experiment 3: Assessing the estimation accuracy for variations in the ground-truth elastic distribution. As each image dataset is expected to be inherently associated with a unique elasticity distribution, we assessed the accuracy in the estimation for different elasticity distributions. Normal ground-truth elasticity distributions were assigned to the biomechanical model as described above. Since our primary aim was to investigate lung elastography for radiotherapy purposes, spherical masses were included within the normal elasticity distributions for each lung region to represent emphysematous and cancerous regions respectively. Emphysematous tissue was investigated along with tumors because the risk of lung cancer in patients with COPD in two- to five-fold greater than those without COPD [82, 83]. A homogenous Young's modulus value of 1 kPa was chosen to represent emphysema, as emphysema lowers the elastic modulus of tissue, while a homogenous Young's modulus value of 25 kPa was chosen to represent malignant tumors, which are known to have a higher elasticity than the surrounding soft tissue [84, 85]. The cancerous tumors had a diameter of 7 mm, while the emphysematous regions had a diameter of 21 mm [86, 87]. The accumulation of the normal, cancerous, and emphysematous elasticity distributions for each lung region resulted in 18 total ground-truth elasticity distributions that were evaluated in this study.

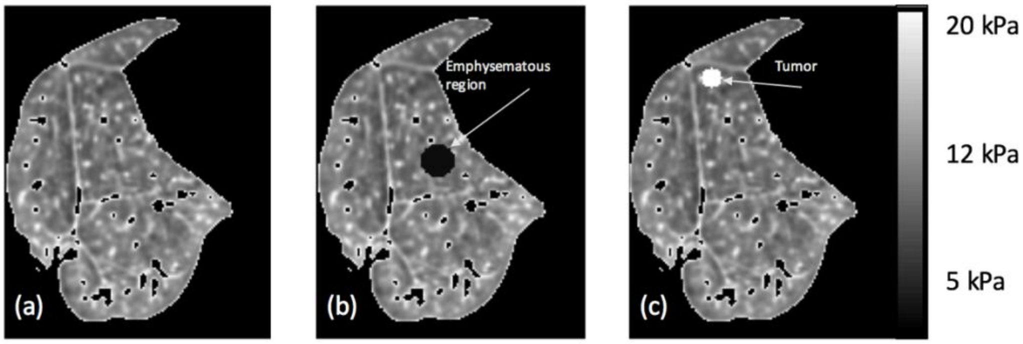

Figure 3-5: 2-D slices of base of right lung showing ground-truth elasticity distributions representing normal (a), emphemsema (b), and cancerous (c) tissue.

Figure 3-5 shows example ground-truth elasticity distributions for a 2-D slice of the base of the right lung. Figure 3-5(a) illustrates normal tissue, while an emphysematous region with low elasticity has been added in 3-5(b) and a stiff nodule representing a tumor has been added in 3-5(c). Emphysematous and cancerous regions were added at different locations in each of the 6 different geometries to evaluate whether or not the location of the abnormality affected the results.

3.3.2.4 Experiment 4: Assessing the estimation accuracy for variations in the boundary constraints. In order to emulate air filling different regions of the lung, the boundary of the lungs was drawn outward along a normal vector with respect to the center of mass of the modeled lung section. The magnitude of the outward deformation was constrained based upon typical motion amplitudes derived from the literature, as shown in Table 3-1 [68, 69]. Three different boundary constraints were investigated for each lung region to examine the influence of boundary motion on the convergence of our methodology.

Table 3-1: Boundary constraint based upon typical motion for apex, middle, and base regions of the lung [71, 72].

Boundary Constraint (BC)	**Lung Region**		
	Apex	Middle	Base
BC 1 (mm)	2	3	10
BC 2 (mm)	4	6	13
BC 3 (mm)	6	9	16

These boundary expansions were illustrative of the low ventilation and subsequent low parenchymal expansion in the apex during different breathing stages, and the slightly larger expansion of the middle and basal regions of the lungs. It shall be noted, that while the surface particles of the lung were drawn outward, the inner voxels were allowed to deform according to the elastic forces in the model.

3.4 Results

In this section, we present the results obtained from the systematic study. The experiments were performed with apex, middle, and base sections of a right and a left lung, as shown in Figure 3-3 above.

As mentioned above, each of the virtual phantom generated dataset contained 25 slices with a resolution of 145x179 pixels. Finite mass elements were created for each voxel of lung tissue, which resulted in between 300,000 and 500,000 finite element nodes depending on the dataset. The elastodynamic biomechanical lung model was deformed for 5000 timesteps during each iteration. Each iteration took about one minute to complete, and the whole system converged in 15 – 30 minutes. Two elasticity estimations were completed for each dataset using an applied xy- and z-force, and the final elasticity estimation results were achieved within an hour of computation time.

The average results for the measured elasticity are as listed in the geometry section of Table 3-2. On average, the right lung converged with an average of 99.98% of voxels within 0.5 mm of ground-truth displacement values. This ensued with 91.59% of voxels converging within 1 kPa of ground-truth elasticity. For the left lung, an average of 99.92% of voxels converged within 0.5 mm of ground-truth displacement, corresponding to 91.87% of voxels arising within 1 kPa of ground-truth elasticity. A two-sample t-test was performed between 27 right and 27 left lung ground-truth distributions, and confirmed that the differences between the convergence results of the right and left datasets were not significant ($P > 0.05$). Figure 3-6 highlights the geometrical differences between a 2-D slice of the right (a & b) and left (c & d) apex. Figure 3-6(a & c) show ground-truth elasticity distributions, while Figure 3-6(b & d) show our lung elastography results with the discrepancy (error > 1 kPa) highlighted in yellow. It should be noted the similarity between the novel reconstructions (b & d) and the corresponding ground-truth distributions (a & c)—both novel reconstructions are 95% similar to their ground-truth distributions, illustrating that the high accuracy of the elasticity estimation process is independent of the lung geometry's complexity. We now present the results obtained from the experiments outlined above.

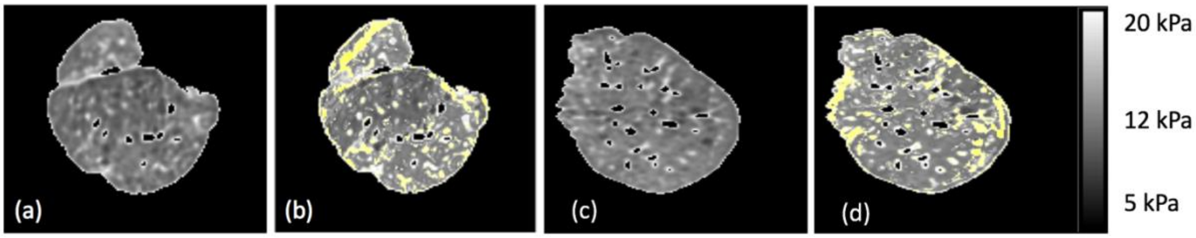

Figure 3-6: 2-D slice of right (a & b) and left (c & d) apex. (a & c) show the ground-truth elasticity distributions, while (b & d) show elasticity reconstructions with the use of our novel convergence criteria. Elasticity discrepancies (error > 1 kPa) are highlighted in yellow

3.4.1 Experiment 1: Assessing the locally heterogeneous convergence

First, to reinforce the necessity of the locally heterogeneous convergence magnification approach, the convergence criteria ϵ from Equation (3-1) was reduced to 5 μm in an attempt to homogeneously magnify the displacement differences. While over 90.2% of voxels converged within 5 μm, less than 5% of voxels converging within 1 kPa of the ground-truth data.

Figure 3-7(a) illustrates the ground-truth elasticity distribution for a 2D-slice of the base of the middle left lung, while (b) shows the reconstruction with a modified ϵ of 5 μm. Since the methodology was unable to draw useful information from the subtle deformation of each voxel, it converged to a low contrast, homogenous Young's modulus estimation, as shown in Figure 3-7(b). For comparison, 3-7(c) again illustrates the inability of the conventional reconstruction (this time with a convergence criteria of 0.5 mm used as ϵ in Equation (3-1)) to estimate the elasticity distributions precisely. While high displacement accuracy is again achieved, similarly to Figure 3-7(b), the resulting elasticity distribution is a low contrast, homogenous Young's modulus estimation. Reducing epsilon does not improve the accuracy of the reconstruction using Equation (3-1). The reconstruction was much improved when the novel locally heterogeneous magnification technique was used, as shown in Figure 3-7(d). Therefore, we conclude that it is necessary to use Equation (3-2) to achieve good elasticity estimation results. For the rest of the systematic study, a global convergence criterion of 0.5 mm is utilized.

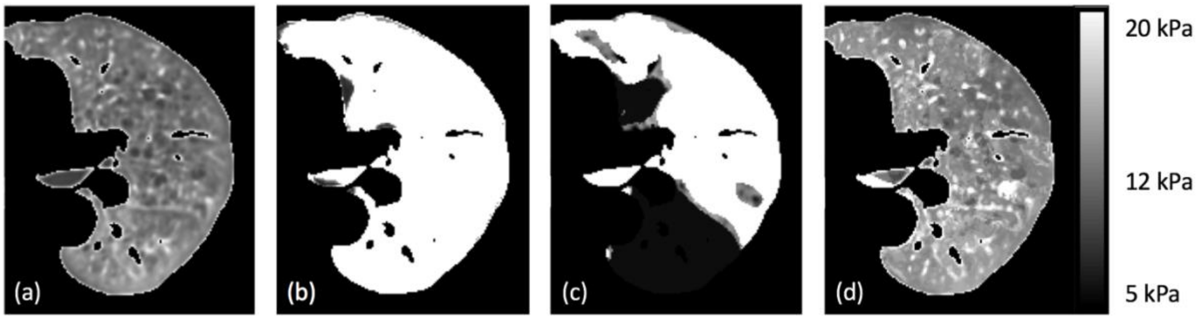

Figure 3-7: Ground-truth (a), conventionally reconstructed elasticity with ϵ of 5 μm (b), conventionally reconstructed elasticity distribution with globally magnified convergence criteria of ϵ being 0.5 mm (c), and reconstruction using novel locally heterogeneous convergence magnification approach (d) for a 2-D middle slice of the left lung

To further reinforce the necessity of the locally heterogeneous convergence magnification approach, a two-sample t-test was performed to determine whether or not the differences observed between the results with and without the use of the technique were significant. With a mean displacement accuracy of 93.27% and 99.95%, and a mean elasticity accuracy of 77.05% without and 91.94% with the use of the novel technique, the two-sample t-test confirmed that the observed difference was significant ($P < 0.05$).

The improved accuracy of the methodology with the use of the novel technique is also documented in Figure 3-8. The subtle displacement error of the conventional technique, shown in green in Figure 3-8(a) leads to divergence in the elasticity estimation shown in green Figure 3-8(b). However, when the locally heterogeneous magnification method was applied, shown in blue, both the displacement and elasticity error converged correctly. Therefore, we concluded that use of the locally heterogeneous technique provided meaningful improvements to our methodology, and it is used for the rest of the systematic analysis.

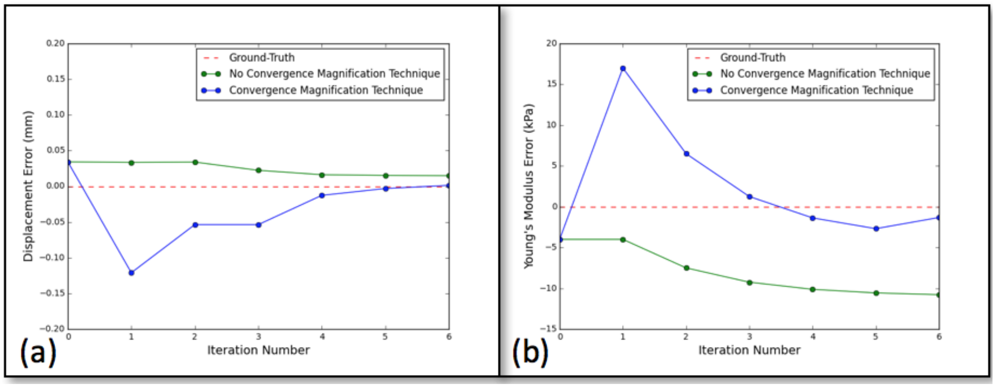

Figure 3-8: Displacement (a) and elasticity (b) error for methodology with and without convergence magnification approach.

Table 3-2: Overall average results from systematic analysis, along with results broken down by performance analysis criteria.

Performance Analysis Criteria – Average Results	**Displacement Accuracy < 0.5 mm (%)**	**Elasticity Accuracy < 1 kPa (%)**
Overall Averages	99.95	91.95
Geometry		
Right	99.98	91.59
Left	99.92	91.87
Ground-truth distribution		
Emphysema	99.95	91.90
Cancerous Tumor	99.94	91.68
Normal Tissue	99.95	91.62
Boundary Constraint		
BC 1	99.97	93.81
BC 2	99.98	90.87
BC 3	99.90	90.56

3.4.2 Experiment 2: Assessing estimation accuracy for forward model variations

Both an elastodynamic and elastostatic forward model were used to compute ground-truth displacement values. Elastodynamic ground-truth displacement values and elastostatic ground-truth displacement values were calculated using the corresponding forward models. Reconstructed displacements computed using the elastodynamic forward model were then compared to each set of ground-truth displacement values mentioned above. The overall and average results for the elastodynamic ground-truth are discussed in the previous section. When the ground-truth data was recorded using an elastostatic forward model, without the novel convergence magnification technique 71.39% of voxels converged within 0.5 mm and 1 kPa . When the novel convergence technique was utilized, 86.17% of voxels converged. This indicates the potential of our approach to converge even when a different model is used to obtain ground-truth deformation values. Therefore, it is reasonable to assume our approach can extend to clinical deformation information. To determine the impact of SNR on estimation accuracy, random noise within ± 5% was added to each of the source images for both the elastodynamic and elastostatic forward models analyzed in the experiments above. It was found that without the novel convergence magnification technique, the 57.2% of the voxels converged within 0.5 mm and 1 kPa of the "noisy" ground-truth values. When the locally heterogeneous convergence magnification approach was utilized, however, 73.3% of voxels converged within the aforementioned tolerance. This illustrates that our approach will obtain useful deformation information from image datasets with lower SNR. These results are summarized in Table 3-3 below.

Table 3-3: Average results from systematic analysis of three different ground-truth forward models.

Ground-truth forward model	Accuracy w/o Novel Magnification (%)	Accuracy w/ Novel Magnification (%)
Elastodynamic	77.07	91.94
Elastostatic	71.39	86.17
"Noisy"	57.20	73.29

For the remainder of the experiments, the elastodynamic forward model is used to obtain ground-truth deformation values.

3.4.3 Experiment 3: Assessing the estimation accuracy for variations in the ground-truth elastic distributions

Table 3-2 lists the average results for the systematic analysis performed using the locally heterogeneous convergence magnification method. The results were also broken down by experimental category. As mentioned above, three different ground-truth elasticity distributions—emphysematous, cancerous, and normal tissue—were investigated to analyze the robustness of our methodology. On average, the methodology converged with displacement accuracy values of 99.95%, 99.94%, and 99.95% for emphysematous, cancerous, and normal tissue respectively. These results, presented in Table 3.2 above, corresponded to 91.90%, 91.68%, and 91.62% of voxels converging within 1 kPa of the ground-truth elasticity values. Figure 3-9 illustrates the robustness of the methodology for reproducing different ground-truth elasticity distributions. Figure 3-9(a) shows the conventional elasticity reconstruction, which was the same for normal, emphysematous, and cancerous ground-truth elasticity distributions. Discrepancies between the reconstruction and the normal ground-truth elastic distribution that are greater than 1 kPa are highlighted in yellow. It can be seen that initially, the reconstruction is very different from the ground-truth, with a similarity of less than 50%.

Figure 3-9(b – d) show the novel elasticity reconstruction for normal, emphysematous, and cancerous tissue respectively, with the discrepancies (error > 1 kPa) between the reconstructed and ground-truth data highlighted in yellow. With similarity values of 92.73%, 93.44%, and 91.10%, it can be seen that use of the locally heterogeneous convergence magnification greatly improves the elasticity reconstruction, allowing for the visualization of emphysematous and cancerous regions within the lungs. It should be noted that for each lung geometry, cancerous and emphysematous regions were placed at different locations within the 2-D slices to ensure that the regions could be localized regardless of position. A two-sample t-test was performed between the mean values of 18 different emphysematous, 18 different cancerous, and 18 normal tissue distributions, and the observed difference was convincing enough to say that the average values of each ground-truth elasticity distribution did not differ significantly (P > 0.05).

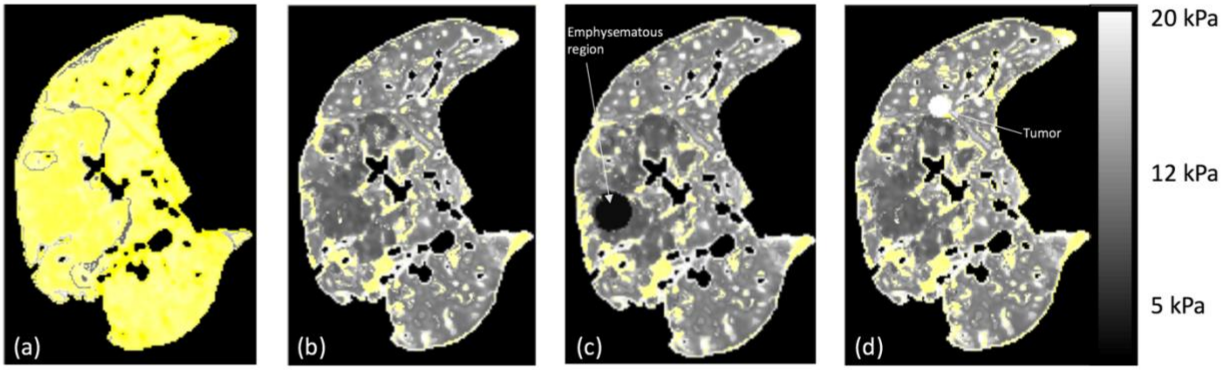

Figure 3-9: 2-D slice of middle right lung. (a) shows the conventional reconstruction for all 3 ground-truth elasticity distributions. (b) shows the novel reconstruction for normal tissue, (c) shows the reconstruction for normal tissue with emphysematous region, and (d) shows the reconstruction for normal tissue with tumor. Discrepancies (error > 1 kPa) between the reconstructed and ground-truth distributions are highlighted in yellow.

3.4.4 Experiment 4: Assessing the estimation accuracy for variations in the boundary constraints

As previously noted, the outward motion of the lung boundary was constrained to three different values for each section of the lung as listed in Table 3-1. The resulting displacement and elasticity accuracy values of the methodology are listed in Table 3-4 below. Overall averages are listed for the three different boundary constraints in Table 3-2 above. A two-sample t-test was performed on these values, and it was found that there were no significant differences between the results regardless of whether boundary constraint 1, 2, or 3 was used for each geometry.

Table 3-4: Displacement and elasticity accuracy values for different geometries and boundary constraints.

Lung Geometry - Boundary Constraint	Displacement Accuracy < 0.5 mm (%)	Elasticity Accuracy < 1 kPa (%)
Apex – 2 mm	99.99	97.89
Apex – 4 mm	99.99	97.55
Apex – 6 mm	99.97	96.82
Middle – 3 mm	99.92	94.17
Middle – 6 mm	99.94	92.18
Middle – 9 mm	99.95	90.07
Base – 10 mm	99.98	89.37
Base – 13 mm	99.99	82.86
Base – 16 mm	99.78	84.80

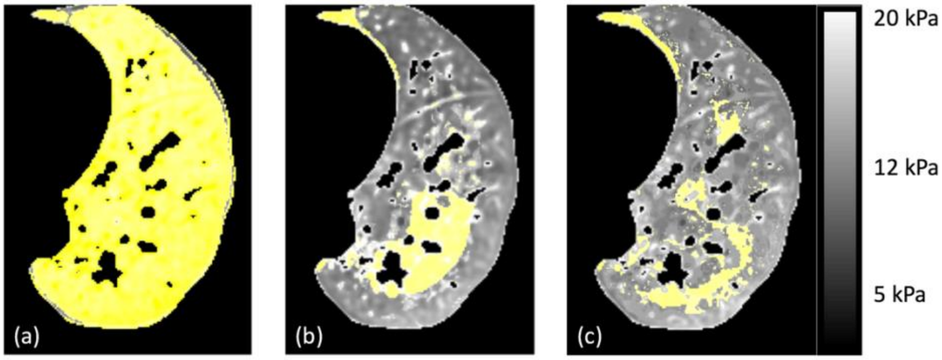

Figure 3-10: 2-D elasticity reconstruction of base of left lung. (a) shows conventional reconstruction, (b) shows novel reconstruction with 10-mm boundary constraint, and (c) shows novel reconstruction with 16-mm boundary constraint. Discrepancies (error > 1 kPa) between the reconstructed and ground-truth distributions are highlighted in yellow.

Figure 3-10 further illustrates that the reconstruction converges similarly regardless of the boundary constraint magnitude. Figure 3-10(a) shows the conventional reconstruction of the base of the left lung, (b) shows the reconstruction when a 10-mm boundary constraint was applied, and (c) shows the reconstruction when a 16-mm boundary constraint was applied. Figure 3-10(a) is over 50% different than the ground-truth, while 3-10(b) and 3-10(c) are only 6.07% and 6.34% different from the ground-truth respectively. The result supports the accuracy in estimating the lung elasticity for varying boundary constraints.

In summary, our elasticity estimation converged with about 99% sub-millimeter accuracy, resulting in an elastic convergence of about 92%. We have shown that the use of the locally heterogeneous convergence magnification approach is necessary in the transition to apply our conventional elastography technique to lung anatomy. However, use of different ground-truth elasticity distributions and different boundary constraint magnitudes did not affect the convergence of our technique. While we mainly focus on ground-truth values obtained from an elastodynamic forward model, “noisy” and elastostatic forward models also produced reliable elasticity estimations.

3.5 Discussion

In this chapter, we presented a methodology for determining lung tissue elasticity using conventional CT imaging protocols performed within a radiotherapy workflow. The procedure was developed and assessed using a virtual lung phantom with simulated ground-truth elasticity and displacement values. A high-resolution biomechanical simulation was employed as an elastodynamic forward model to solve the inverse linear elasticity problem. To simulate breathing motion, lung surface displacements were applied as boundary constraints, while the inner lung voxels of the biomechanical model were allowed to deform according to the pre-assigned linear elasticity. A novel locally heterogeneous convergence magnification was then applied to allow our conventional elastography methodology to be sensitive to the subtle deformation of the interior lung tissue.

The biomechanical model was created with a physics-based approach to represent the interior lung tissue, a choice that was motivated by the previously shown accuracy of the simulation for head and neck and breast applications [52, 60]. Because of the successful simulation of other anatomies, along with the work of other researchers that suggested that the lung can be successfully modeled as a linear elastic material, the physics-based biomechanical model was expected to be able to accurately model the lung [88, 89]. Using this well-validated constitutive model allowed us to focus on the accuracy and feasibility of the model when applied to lung elastography. Such a well-validated constitutive model is necessary as lung behavior differs drastically between in vivo and ex vivo environments, so typical ex vivo validation experiments would probably prove infeasible and would need to be very carefully designed. When transitioning to clinical deformation data, potential differences in the numerical estimation may stem from sources such as the 4D image artifacts, cardiac motion, irregular breathing and hyperelastic lung behavior. Novel efforts, such as the 5D imaging protocol, have been employed to address imaging-related issues, which will enable the measurement of lung tissue elasticity within the radiotherapy setup to be a feasible approach. While elasticity estimation has been performed using elastostatic and “noisy” forward deformation models, other complicated physics-based models have also been used to represent lung deformation; it would also be worthwhile to perform the elasticity estimation technique using these models as a forward setup.

For the systematic analysis, a forward model is employed that utilizes the same elastodynamic physics as the forward model used during the elasticity estimation process. This is necessary to systematically examine the accuracy of the elasticity estimation, as ground-truth elasticity values of lung tissue are not known. Though we are utilizing the same linear elastic constitutive model to deform and invert the biomechanical model, the iterative inverse process utilizes a gradient-based binary search methodology and a locally heterogeneous convergence magnification technique that allow elasticity estimations to be obtained from any displacement information, regardless of the model used to generate the deformation data. Such an experiment was necessary in order to investigate the potential accuracy of the elasticity estimation algorithm. As our biomechanical simulation has been shown to accurately model tissue motion, it is our hypothesis that, when actual tissue motion vectors obtained from optical flow DIR techniques are used, our elasticity estimation algorithm will still be able to perform well. This is further represented by the convergence that was obtained using elastostatic and “noisy” ground-truth deformation values. Further studies will focus on extending the usage of such a model to incorporate clinical 4DCT lung deformation data obtained from optical flow deformable image registration techniques. Errors quantified during this approach will be correlated to the quantitative nature of the 4D imaging systems. The following chapter will focus on addressing the challenges associated with transitioning from virtual phantoms to clinical data.

Unlike other elastography methods, the novel lung elastography method presented directly relates elasticity with the displacement of lung tissue in a clinically relevant manner. Initial results using the conventional elastography method presented in Chapter 3 (Hasse, Neylon [60]) indicated the need for an additional novel locally heterogeneous convergence magnification. The conventional methodology resulted in high displacement accuracy, but no useful elasticity information was gleaned upon convergence, further highlighting the need for a systematic study with virtual lung phantoms and known ground-truth elasticity distributions. The novel technique provided added deformation to each voxel and amplified the differences in displacement error, stabilizing the elasticity estimation and allowing it to converge while maintaining the integrity of the solution. This allows our elasticity estimation methodology to be much more sensitive to the subtle changes often seen in the interior tissue of the lungs. Future work will focus on addressing the general applicability of the proposed algorithm for solving more general inverse problems.

Our results indicated that high accuracy can be obtained using deformation information gleaned from 4D lung datasets (e.g. 4DCT and 5D lung protocols). Variations in the lung geometry and ground-truth elasticity distribution resulted in insignificant differences in the resultant elasticity distributions, indicating the potential of the methodology to converge with clinical data, which may be more complex than the data used in our study. The convergence of the methodology irrespective of the boundary constraint demonstrates that, when applied to clinical data, the elasticity estimation technique should converge with any breathing stage that can be utilized to garner displacement data. Future work will investigate using deformation data from multiple breathing stages to more quickly estimate elasticity distributions. Further constraints on the boundary motion of the biomechanical model will also be investigated with respect to the physical motion of the lungs and the effect on estimation accuracy. In order to optimize the force applied to each voxel in the convergence magnification technique, the elasticity estimation process is completed multiple times for each dataset, and converges completely within an hour.

The elasticity information we obtain through this methodology will be used to improve respiratory brachytherapy seed implantation and tumor tracking in radiotherapy. Knowing the elastic distribution and motion of the lung tissue can allow radiation therapists to increase dose to the lung tumors while sparing normal tissue, reducing clinical margins, and decreasing normal tissue toxicity. This methodology could also prove useful for patients with other lung diseases, such as COPD.

Because 4DCT imaging techniques are currently used within lung radiotherapy workflows, lung tissue deformation data is known on a voxel-by-voxel basis and the construction of the biomechanical model devised in this study can be easily integrated. While 4DCT image artifacts could cause errors in elasticity estimation, the recent push towards 5DCT imaging techniques could provide less noisy, artifact-free clinical ground-truth deformation data. The usage of GPU based computations for the elasticity estimation enables the computations to be completed in reasonable timings.

Since our focus was to bring lung elastography into the radiotherapy setup, a linear elastic model was employed for the elasticity estimation process. However, the linear elastic model of the lungs may be simplistic for representing complete lung behavior in those patients with COPD. In our future studies, the linear elastic assumptions will be expanded to hyperelastic constitutive laws to try and more accurately depict the mechanics of diseased lung tissue. The impact of different strain rates on the elasticity assumptions and estimations will also be investigated. For these future studies, a fast simulated annealing approach will be designed to estimate the lung's hyperelasticity. The current imaging protocols will also need to be modified in order to better describe the hyperelastic lung behavior; for example, the incorporation of fast helical CT scans could provide more information about the lung deformation.

3.6 Conclusions

In this chapter, we present a systematic study of a novel inverse analysis elastography method for lung tissue using virtual lung phantoms and simulated deformation values. The methodology employed a forward physics-based biomechanical model of the lungs that was iteratively deformed to represent the deformation of lung tissue that occurs during the breathing cycle. A novel locally heterogeneous convergence magnification technique was applied in order to gain elasticity information from the subtle deformation of the interior voxels of the lungs. The inverse analysis consisted of a gradient descent based binary search optimization scheme to update the spatial elasticity distribution of lung tissue according to the discrepancy between ground-truth and experimental deformation. Our analysis showed an average of 92 ± 5 % of voxels converged within 1 kPa of the ground-truth elasticity and within 0.5 mm of ground-truth deformation. These results indicate the potential of this methodology to be applied to clinical deformation data, which will be investigated in Chapter 4.

CHAPTER 4: UTILIZE BIOMECHANICAL MODEL AND DEFORMATION VECTOR FIELDS TO OBTAIN LUNG ELASTICITY INFORMATION FROM 4D IMAGING.

Estimation and validation of patient-specific high-resolution lung elasticity derived from 4DCT

A version of this chapter has been published as a manuscript: Med Phys, Vol. 45, No. 2, 025006, 2018. doi: 10.1002/mp.12697

4.1 Introduction

Many lung diseases, including lung cancer, are associated with changes in lung tissue biomechanical properties [90]. For instance, pulmonary emphysema and fibrosis are known to be associated with changes in the parenchymal stiffness. Using excised tissue studies, it has been shown that localized changes in the biomechanical properties of lung parenchyma preceded the initiation and progression of certain lung diseases [17, 90]. However, the ability to quantify and localize pulmonary disease onset and progression at a regional level using *in vivo* studies is currently limited. Gold-standard spirometry-based estimates are the current state of the art approach used for overall chronic disease characterization [91] but do not explicitly characterize regional lung biomechanical information [92]. While computed tomography (CT), specifically 4DCT, is commonly used for lung radiotherapy imaging and treatment planning purposes, it does not present a quantitative characterization of the lung biomechanical properties [93].

To learn patient-specific lung biomechanical properties within the radiotherapy context, this study investigates the application of elastography using 4DCT scans of the human lung. We hypothesize that such an approach will enable lung tissue elastic properties to be estimated using conventional radiotherapy imaging modalities. A critical step in furthering the uses elastography within the radiotherapy context is the need to quantitatively validate the lung elasticity measurements. Once validated, these properties can be used for advancing lung cancer treatment planning and delivery, and monitoring treatment response.

The lung elastography approach was previously described in Chapter 3. For application of the elastography approach in this study, the ground-truth tissue behavior was characterized from the 4DCT datasets. 4D displacement vector fields (DVF) obtained from deformable image registration were employed as a boundary constraint to guide the elastography process [94]. A key component of this study is the quantitative validation of the estimated lung elastography distributions. Since 4DCT scans have data for every phase of the breathing cycle, validation is performed by analyzing mid-exhalation.

The rest of the chapter is organized as follows: Section 4.2 introduces the methods employed for the elastography and the validation processes. Section4.3 presents the qualitative results of the deformable image registration, elastography, and validation process, while section 4.4 presents a numerical analysis of the results. Section 4.5 presents a discussion of the results and highlights the areas for continued research, and section 4.5 concludes this chapter.

4.2 Methods

Our elastography process focused on the effective Young's modulus (E) estimation for each voxel of lung tissue using 4DCT lung data. Figure 4-1 shows a flow chart summarizing the elasticity estimation. First, the end-inhalation and the end-exhalation breathing phases from the 4DCT lung images were registered using an optical flow deformable image registration (DIR) algorithm. The lung DVF was obtained for every voxel of the end-exhalation breathing phase. The biomechanical model was then assembled using the end-exhalation lung geometry along with a random elasticity distribution as the initial elasticity value. Using the ground-truth lung DVF, the elasticity distribution was optimized. Spatial elasticity and displacement error distributions were obtained and validated.

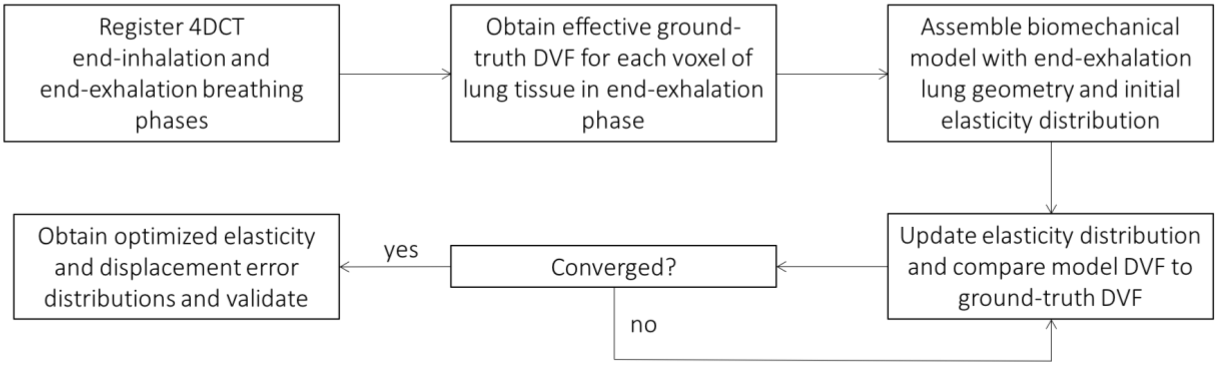

Figure 4-1: Flow chart showing 4DCT elasticity estimation process

In this section, we first briefly present the DIR technique used to obtain the ground-truth DVF. Next, we present the constitutive model used for representing tissue biomechanics in order to solve the inverse elasticity problem. We then present the optimization process used in the iterative elasticity estimation. This is followed by a discussion of the convergence criteria used for the optimization process. We then describe the image similarity metrics used in our study to characterize the quantitative accuracy of the estimated elasticity combined with the constitutive model. We conclude the section with a discussion of the validation study.

4.2.1 Deformable image registration

The model-guided elasticity approach presented in this study relies on displacement values extracted from DIR of 4DCT datasets. The lung is a challenging organ to register and requires DIR due to the large deformation caused by respiration. A patient cohort of 15 4DCT datasets that were acquired using 5DCT protocol (IRB# 11-000620-CR-00004) was employed for the elasticity estimation [95-97]. The patient cohort consisted of lung cancer patients undergoing SBRT at UCLA. The average age of the patients was 66, six of the patients were male, and nine were female. The 4DCT scans were acquired on Siemens Definition Flash, Siemens Biograph 64, and Siemens Definition AS 64 scanners with 1 mm slice thickness.

The left and right lungs were segmented using an intensity-based thresholding approach [98]. Segmented end-inhalation (85th percentile breathing amplitude) were deformably registered to the spatial domain of the end-exhalation (15th percentile breathing amplitude) breathing phases using a well-validated in-house multi-level optical flow DIR algorithm [94]. This registration algorithm has been well-validated for both the lung and head and neck anatomies [99, 100]; therefore, we trust the resulting DVF to be an effective representation of the ground-truth lung motion. The registered DVF for each voxel will be taken to be the effective ground-truth displacement, henceforth denoted as simply ground-truth, for the elasticity estimation process.

4.2.2 Constitutive model

The model presented in this section is focused on computing the lung tissue deformation for a given lung boundary displacement arising from the ground-truth DVF, as previously demonstrated in [59]. The model has been previously described in [52, 60] and specifically applied to the lungs in [61, 101]. This approach is appropriate for our current study since its applicability has been systematically investigated [101]. For clarity purposes, a brief description of the constitutive equations for the forward model [52] is presented here.

4.2.2.1 Model geometry. The biomechanical lung model was assembled from the 4DCT end-exhalation images. The model geometry was represented by finite element nodes corresponding to the center of each voxel in the end-exhalation image. Lung tissue, an elastic material, was viewed as a series of these finite mass elements coupled with linear elastic connections to adjacent mass elements in deformation space. This was to ensure a physically realistic deformation. Rest length and orientation of each connection were then documented and assigned an initial effective Young's modulus and a Poisson's ratio of 0.43 [62-64].

4.2.2.2 Model physics. In our approach, linear elastic constitutive laws were implemented because linear elastic representations have been found to be effective in describing normal lung tissue deformations typically observed in 4DCT-based lung motion [65]. Additionally, a study investigating lung tumor motion during external beam radiotherapy found that a hyperelastic constitutive law performed very similarly to linear elastic constitutive law at deformation magnitudes found within the lungs during normal breathing [64].

The model is actuated due to changes in boundary constraints, which subsequently calculates corrective forces on each mass element for given boundary constraints. In our approach, we compute the boundary constraints from the lung boundary DVF. The corresponding forces on each mass element were calculated as described in §2.2.1.2.

4.2.3 Inverse elasticity formulation

For clarity, the simplifying notation that will be used in this chapter is listed in Table 4-1.

Table 4-1: Notation and description for resultant terms utilized in the manuscript

Notation	Description
$\mathrm{D}VF_{DIR,A}$	Ground-truth end-exhalation to end-inhalation DIR DVFs
$\mathrm{D}VF_{DIR,B}$	Ground-truth end-exhalation to mid-exhalation DIR DVFs
$\mathrm{D}VF_{Model,A}$	Model-generated end-exhalation to end-inhalation DVFs
$\mathrm{D}V\mathrm{F}_{Model,B}$	Model-generated end-exhalation to mid-exhalation DVFs
E_A	Effective elasticity distribution obtained from minimizing error between $DVF_{DIR,A}$ and $DVF_{Model,A}$

The inverse elasticity problem was formulated as a parameter-optimization problem with an objective to determine the elasticity parameter that would minimize the difference between the ground-truth DVFs ($DVF_{DIR,A}$) and those computed by the constitutive model, as described in §2.2.2. Solving this inverse elasticity problem was carried out in two steps : 1) estimating the DVF for every voxel of tissue for a given elasticity distribution and changes in boundary constraints, and 2) optimizing the elasticity distribution to best reproduce the $DVF_{DIR,A}$.

In the first step, we applied the lung boundary conditions, and the interior mass elements were allowed to deform according to the elastic constitutive forces within the model, as described in §2.2.1.2 above. For the second step, the iterative scheme for estimating the elastic distribution is based on the inverse relationship between Young's modulus and displacement. Given an initial Young's modulus distribution, the constitutive model computed mass-element displacements [70]. These displacements were then compared with $DVF_{DIR,A}$, and the effective Young's modulus was iteratively updated until the difference between the above two displacement maps was minimal. New displacements values were generated for each iteration by updating the effective Young's modulus distribution as described in §2.2.2.1.

After the elasticity was updated, the biomechanical model was then reset to the initial un-deformed rest position, and the boundary constraints were re-applied. The reconstruction process was repeated until a suitable stopping (convergence) criteria was reached. Upon convergence, the resultant elasticity estimation (E_A) is recorded along with the resultant deformation vector for each voxel ($DVF_{Model,A}$).

4.2.4 Convergence metrics

The convergence metrics utilized in this study are a critical component to interpreting the results. At each iteration of the elasticity estimation, the resultant model DVF, $DVF_{Model,A}$, were compared to $DVF_{DIR,A}$. The number of voxels that converged within a certain ϵ value of ground-truth was quantified as follows:

$$c_a = \begin{cases} 1: & \left\| |d_a| - |d_{a,0}| \right\| < \epsilon \\ 0: & otherwise \end{cases} \quad (4\text{-}1)$$

$$p_\epsilon = \frac{\sum_1^n c_a}{n}. \quad (4\text{-}2)$$

In Equation (4-1), (ϵ) represents the L2-norm of the DVF for each voxel a and c_a represents the error for each voxel. The percent accuracy p_ϵ was then tabulated by summing the c_a over all n voxels in lung volume V using Equations (4-1) and (4-2). For elastography purposes, the iterative process was stopped when $p_\epsilon \geq 0.95$. The maximum iteration limit was set to be 100.

Factors that impact the convergence criteria are determined by image resolution and range of DVF values. In our case, the image resolution was limited to 1 cubic mm, which led to a $\epsilon_1 = 1$ mm. Image resolution is also impacted by the signal in the underlying tissue. Higher signal-to-noise (SNR) is generally observed in blood vessels due to the high contrast and constant structure during deformation, while parenchymal tissue exhibits lower SNR. For this reason, accuracy will be considered for voxels representing blood vessels and parenchymal tissue separately. The voxels representing the two substructures were segmented using an intensity threshold of -500 HU [102]. Since lung deformation can vary widely between patients and breathing phases, we also formulated a convergence criteria, where the percent of voxels converged within 10% of the maximum deformation, or $\epsilon_2 = 0.1 * \max_a(|d_a|)$. For each 4DCT dataset, we computed the minimum value among ϵ_1 and ϵ_2, and employed that for the optimization process. However, once the elasticity estimation converged, the results were evaluated according to both convergence criteria.

4.2.5 Image similarity metrics for quantitative evaluation

While the convergence criteria provided a quantitative way to assess the elasticity estimation accuracy, an additional metric was necessary to ensure the precision of the estimated elasticity. Specifically, we wanted to ensure that E_A and $DVF_{Model,A}$ could be used to warp the end-exhalation image to closely represent the end-inhalation image. In addition, the usage of image similarity metrics could quantify the accuracy of the ground-truth data. The image similarity metrics will be quantified for both the estimation and validation datasets. The results will be compared for significant difference using the student's t-test. For this purpose, three different image similarity metrics were utilized.

4.2.5.1 Structural Similarity Index Metric. The Structural Similarity Index Metric (SSIM) was the first image similarity metric we investigated. SSIM has been previously investigated for the lung, and examines structural changes that more closely correlate with a visual evaluation rather than differences that do not contribute to perceived image quality, which is important for lung [103-105].

The SSIM [106] is formulated as follows:

$$SSIM(x,y) = \frac{(2\mu_x\mu_y+c_1)(2\sigma_{xy}+c_2)}{(\mu_x^2+\mu_y^2+c_1)(\sigma_x^2+\sigma_y^2+c_2)} \quad \textbf{(4-3)}$$

The SSIM can vary between -1 and 1, where a score of 1 indicates perfect similarity using the equation below. The parameters of Equation (4.3) include spatial patches extracted from two images x and y, the mean of the voxel intensities in x and y (μ), the variance of the intensities in the x and y (σ), and the covariance (σ_{xy}).

4.2.5.2 Normalized Cross Correlation. Another image similarity metric that was used to assess the results of our study was normalized cross-correlation (NCC). NCC is a simple but effective similarity measure that is invariant to brightness and contrast variations [107]. NCC has been previously used to compare similarity of medical lung images in [107] and has the advantage that it is less sensitive to linear changes in amplitude of grayscale values. NCC is often used to overcome intensity changes caused by tissue compression difference between different breathing phases [108]. Like SSIM, NCC values range from a perfect match of 1 to a completely anti-correlated match of -1. The equation for calculating the NCC is shown as

$$NCC(x,y) = C_{xy}(\hat{x},\hat{y}) = \sum_{i,j\in R} \hat{x}(i,j), \hat{y}(i,j), \tag{4-4}$$

where $\hat{x}$ and $\hat{y}$ are intensity normalized warped end-exhalation and end-inhalation images.

4.2.5.3 Mutual Information. The final image similarity metric that we used was mutual information (MI), which is a symmetric and nonnegative similarity measure of entropy between two images that takes high values for similar images. Maximization of MI indicates complete correspondence between two images. MI assumes no prior functional relationships between the images, but rather a statistical relationship that can be evaluated by analyzing the images' joint entropy [109]. Although MI is normally applied to multimodal registration, it is often commonly used for lung alignment [110].

Assuming two images x and y, the mutual information is computed by comparing the image entropy values (i.e. a measure of how well-structured the common histogram is) as follows:

$$MI(x,y) = H(x) + H(y) - H(x,y) \tag{4-5}$$

where $H(x,y)$ is the joint entropy

$$-\sum_{x,y} p_{xy}(x,y) \log p_{xy}(x,y) \tag{4-6}$$

and $H(x)$ and $H(y)$ are the individual entropies

$$-\sum_{x} p_{x}(x) \log p_{x}(x). \tag{4-7}$$

4.2.6 Validation study

A key part of our focus is to validate the estimated elasticity using clinical datasets. However, patient-specific elasticity distributions have not been previously documented in the literature. For quantitative validation purposes, we employed a mid-exhalation breathing phase from the 4DCT dataset that was not used for the elasticity reconstruction. An illustration of the lung deformation differences seen between the estimation dataset and the validation dataset is shown in Figure 4-2 below. The end-exhalation segmented CT is shown in (a). Figure 4-2(b) shows the magnitude of displacement between the end-exhalation and end-inhalation breathing phases used in the elasticity estimation, while Figure 4-2(c) shows the magnitude of displacement between the end-exhalation and mid-exhalation breathing phases used in the validation study.

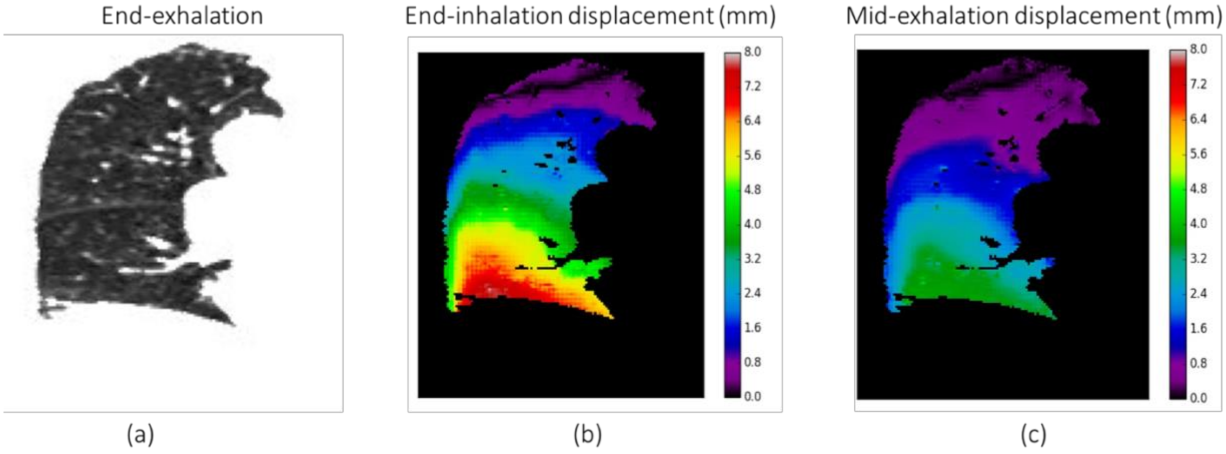

Figure 4-2: Comparison of the breathing phases utilized for elasticity estimation. Source end-exhalation image is shown in (a). The displacement between end-exhalation and end-inhalation is shown in (b), and the displacement between end-exhalation and mid-exhalation is shown in (c).

The accuracy of the elasticity distribution E_A derived from end-inhalation breathing data was quantified by its' ability to also represent the mid-exhalation breathing data. Specifically, the mid-exhalation breathing image dataset was first registered to the end-exhalation breathing phase using the optical flow DIR algorithm. These DVFs were then recorded as $DVF_{DIR,B}$. The elasticity information (E_A) estimated using $DVF_{DIR,A}$ was applied to the biomechanical lung model according to the boundary conditions described above with lung surface displacement now prescribed by $DVF_{DIR,B}$, which generated $DVF_{Model,B}$. The $DVF_{Model,B}$ were then compared to the $DVF_{DIR,B}$, and the accuracy was reported according to the convergence criteria. As an alternative means of quantifying and describing the validation results, image similarity measures were employed to compare end-exhalation images warped with both $DVF_{DIR,B}$ and $DVF_{Model,B}$ to the validation mid-exhalation images. Our hypothesis is that the image similarity measures for the $DVF_{DIR,B}$ and $DVF_{Model,B}$ will be similar to those of $DVF_{DIR,A}$ and $DVF_{Model,A}$.

4.2.7 Implementation details

The computational complexity of iteratively updating a high-resolution finite element model [52] until convergence was countered using a GPU cluster that consisted of 32 NVIDIA TitanX GPUs interconnected by an Infiniband backbone. The GPU cluster allowed the elasticity estimation for each patient lung dataset to converge in around 2 hours of computation time. The numpy and scikit packages of Python 2.7 were used for numerical analysis in this manuscript [111].

4.3 Qualitative results

In this section, we first present the qualitative DIR results, followed by the elasticity estimation results for all the 15 datasets. Finally, we present the qualitative results of the validation process.

4.3.1 Deformable image registration

The accuracy of the DIR results is critical in order to ensure the DIR's validity as ground-truth data for the elastography procedure. Figure 4-3 illustrates an example of the deformable image registration results for a 2D-slice of the left (a & b) and right (c & d) lung. Figure 4-3(a & c) show an overlay of the end-exhalation image in green and end-inhalation image in red. The misalignments between slices are depicted in red (features that are only seen in end-inhalation image) and green (features that are only seen in the end-exhalation image). Significant motion can be observed between the two images in each case. Figure 4-3(b & d) show an overlay of the end-exhalation image warped using $DVF_{DIR,A}$, and the end-inhalation, illustrating the high accuracy at which our in-house optical flow DIR algorithm can calculate DVFs. The maximum $DVF_{DIR,A}$ was observed to be between 6 and 31 mm, while the maximum $DVF_{DIR,B}$was observed to be between 2 and 10 mm.

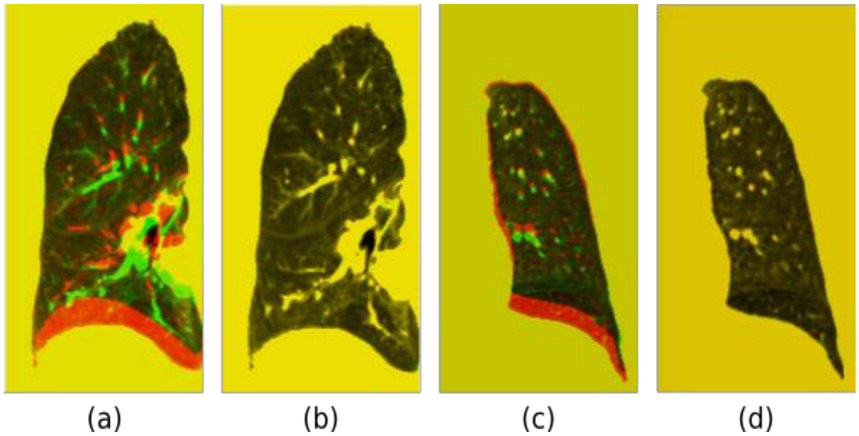

Figure 4-3: Deformable image registration results for sample left (a & b) and right (c & d) 2D lung slice. (a & c) overlay of end-exhalation in green and end-inhalation in red (b & d) overlay of DVF_(DIR,A)-warped end-exhalation and end-inhalation.

<u>4.3.1.1 Elasticity estimation results and accuracy.</u> Over all 15 patient lung datasets, 89.91 $\pm$ 4.85 % of voxels converged within ϵ_2. To illustrate elasticity results and correlate these results to displacement accuracy, Figure 4-4 show the displacement accuracy corresponding with a resultant elasticity map for a 2D-slice of a left patient lung.

Figure 4-4(a) shows the ground-truth displacement in mm ($DVF_{DIR,A}$), while Figure 4-4(b) shows the model displacement also in mm ($DVF_{Model,A}$). Figure 4-4(c) shows the displacement error between Figures 4-4(a) and 4-4(b), with error greater than 1 mm (ϵ_1) highlighted in purple and error greater than 1.2 mm (ϵ_2) highlighted in blue. Finally, Figure 4-4(d) shows the optimized elasticity map, E_A, in kPa. It can be seen that the $DVF_{DIR,A}$ and $DVF_{Model,A}$ are very similar, with low error illustrated in Figure 4-4(c). The minimal displacement error supports the validity of the elasticity estimated for this case. Regions of low motion correspond to regions of lower elasticity; this is due to our underlying assumption guiding the elasticity update process. Though the displacement distributions are relatively smooth, the resultant elasticity distribution varies from voxel to voxel. As no ground-truth elasticity distributions are available for absolute elasticity accuracy calculations, validation was performed using mid-exhalation breathing phase 4DCT data. The results of the validation process will be qualitatively evaluated in the following section.

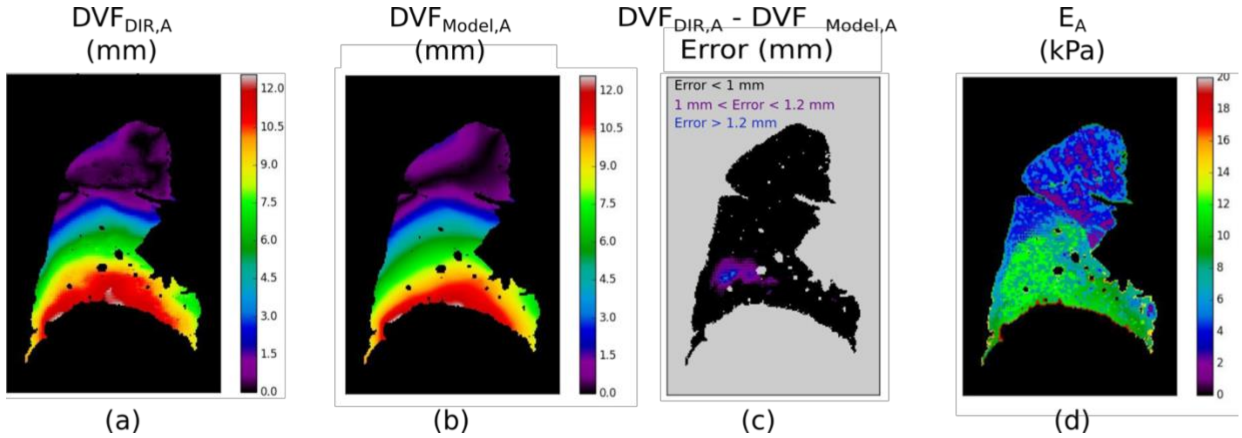

Figure 4-4: 2D-slice illustrating (a) ground-truth displacement $DVF_{DIR,A}$, (b) model displacement $DVF_{Model,A}$, (c) displacement error between (a) and (b) with error greater than ϵ_1 and ϵ_2 highlighted in purple and blue, and (d) resultant elasticity distribution

<u>4.3.1.2 Validation.</u> On average, the validation datasets converged with 87.13 ± 10.62% of voxels within ϵ_1. To illustrate the validation process and results, we present Figure 4-5. Figure 4-5(a) shows the $DVF_{DIR,A}$ for a 2D slice of the right lung in mm. Figure 4-5(b) shows the E_A estimated from the $DVF_{DIR,A}$ in 4-5(a) for the corresponding slice. The validation displacement for a 2D slice of the right lung ($DVF_{DIR,B}$) is shown in mm in Figure 4-5(c). Figure 4-5(d) shows the resultant model displacement in mm after the lung biomechanical model is deformed with the E_A seen in

Figure 4-5(b) ($DVF_{Model,B}$). Figure 4-5(e) illustrates the displacement error between 4-5(c) and 4-5(d), with error greater than 0.4 mm, ϵ_2, highlighted in blue. While a cluster in the center of the slice shown in 4-5(e) had error higher than ϵ_2, a majority of the voxels converged with a high accuracy, illustrating the estimated elasticity's validity in representing the $DVF_{DIR,B}$. The decrease in ϵ_2 due to the decrease in maximum lung displacement can also explain the higher error seen in Figure 4-5(e). These results will be analyzed further in the following section.

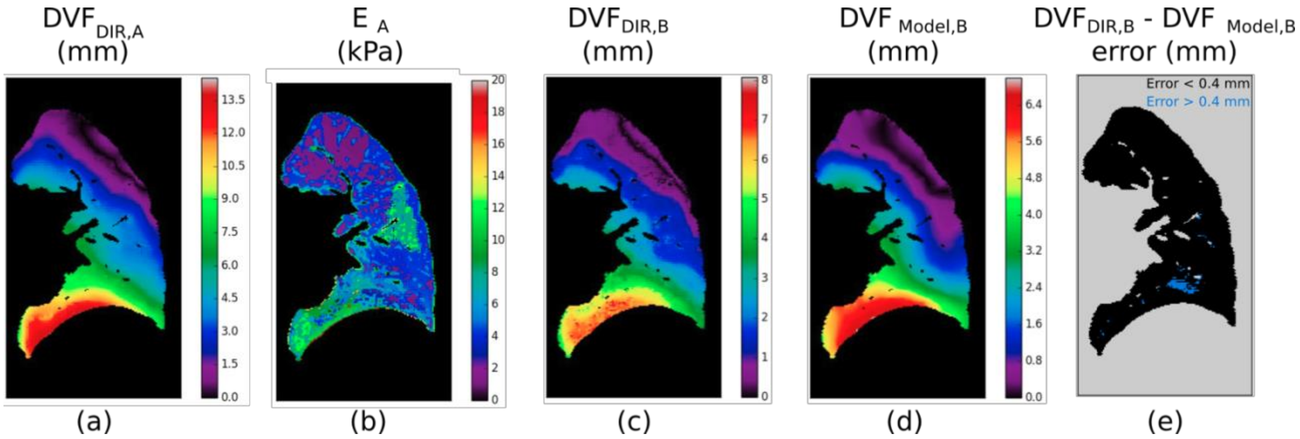

Figure 4-5: 2D-slice illustrating (a) end-inhalation ground-truth displacement $DVF_{DIR,A}$ in mm , (b) estimated elasticity E_A in kPa, (c) mid-exhalation ground-truth $DVF_{DIR,B}$ in mm, (d) mid-exhalation model $DVF_{Model,B}$ in mm, and (e) error between (a) and (b) with error greater than 0.4 mm highlighted in blue.

4.4 Quantitative Evaluation

In this section, we first present the image similarity measures for the DIR, followed by a numerical analysis of the elasticity estimation and validation results.

4.4.1 DIR

The quantitative image similarity of the DIR was documented for two image pairs: a) the $DVF_{DIR,A}$ -warped end-exhalation and end-inhalation images, and b) $DVF_{DIR,B}$ -warped end-exhalation and mid-inhalation images. Table 4-2 summarizes the results for both a) and b), respectively.

On average for a), image pairs had an SSIM of 0.88, NCC of 0.99 and an MI of 1.94, indicating a high similarity. This illustrates the high accuracy of the $DVF_{DIR,A}$ that were used as ground-truth throughout the elastography process. For the validation DIR b), image pairs had an average SSIM of 0.89, NCC of 0.99, and MI of 1.81. These numbers are not significantly different ($p > 0.05$) from the SSIM, NCC, and MI values of a), confirming our hypothesis and illustrating the accuracy of the $DVF_{DIR,B}$ used to validate the elastography process.

Table 4-2: Image similarity metrics SSIM, NCC, and MI for a sample of patient initial end-inhalation to end-exhalation registration as well as validation end-inhalation to mid-exhalation registration

ID	**$\text{DVF}_{\text{DIR, A}}$-warped end-exhalation and end-inhalation**			**$\text{DVF}_{\text{DIR, A}}$-warped end-exhalation and end-inhalation**		
	SSIM	NCC	MI	SSIM	NCC	MI
1	0.90	0.99	1.92	0.91	0.98	2.01
2	0.88	0.98	2.01	0.88	0.98	2.00
3	0.88	0.99	2.01	0.89	0.99	1.95
4	0.86	0.99	2.01	0.88	0.99	2.14
5	0.83	0.98	2.14	0.86	0.96	1.81
6	0.86	0.99	2.04	0.88	0.99	1.76
7	0.87	0.98	1.91	0.88	0.98	1.64
8	0.87	0.99	1.86	0.89	0.99	1.63
9	0.91	0.99	1.73	0.93	0.99	1.69
10	0.87	0.99	2.07	0.87	0.99	1.97
11	0.88	0.99	1.85	0.89	0.99	1.72
12	0.90	0.99	1.61	0.92	0.99	1.49
13	0.88	0.99	2.03	0.89	0.99	1.79
14	0.88	0.99	1.96	0.90	0.99	1.70
15	0.87	0.99	1.87	0.88	0.99	1.66
Avg	0.87	0.99	1.94	0.89	0.99	1.80

4.4.2 Elasticity estimation results and accuracy

The quantitative results of our elasticity estimation for the 15 patient lung datasets are now presented. Table 4-3 indicates the average elasticity, displacement, displacement error, and ϵ_2 accuracy for each patient lung dataset. Overall, $89.91 \pm 4.85\%$ of voxels converged within the prescribed ϵ_2. All patient datasets converged with greater than 80% of voxels within ϵ_1 or ϵ_2. The average elasticity ranged from 4.91 kPa to 7.66 kPa. Variations in the lung physiological factors, such as range of motion and total lung volume, did not affect the accuracy, indicating the applicability of the elastography process to a wide range of patients.

Table 4-3: Average elasticity, displacement, error, and overall accuracy for each patient investigated in this study

ID	Average elasticity (kPa)	Average displacement (mm)	Average error (mm)	Average ϵ_2 accuracy (%)
1	7.66	5.22	0.74	89.43
2	5.87	1.62	0.23	97.75
3	6.23	2.14	0.40	90.64
4	4.91	2.39	0.38	94.37
5	7.07	6.41	0.91	92.63
6	6.37	4.14	0.68	84.38
7	6.72	4.30	0.72	85.01
8	6.79	4.76	0.75	89.39
9	6.45	4.12	0.83	83.68
10	5.17	4.84	0.62	90.78
11	5.37	3.09	0.78	80.95
12	6.14	4.96	0.63	94.26
13	7.25	3.93	0.61	92.53
14	6.20	5.01	0.81	87.29
15	5.46	3.11	0.44	95.55
Avg	6.24	4.00	0.63	89.91

As mentioned above, two convergence criteria were investigated to better quantify the accuracy of the model generated elasticity. Table 4-4 denotes the $\epsilon_1$and ϵ_2 convergence percentages broken down by underlying tissue types for the 15 4DCT patient datasets. Maximum deformation has also been included in the table to illustrate the difference in deformation between patients. It can be seen that the voxels representing blood vessels had a slightly higher accuracy than the parenchymal voxels, though it was not significant when looking at the accuracy with regards to ϵ_2.

The higher accuracy can be attributed to the higher signal-to-noise ratio in the blood vessels when compared to the parenchymal tissue. This illustrates that though local image noise contributes towards estimation error as expected, the accuracy of the parenchymal tissue is still within a clinically applicable error range.

Table 4-4: Voxel convergence and maximum deformation for a sample of patient 4DCT datasets

		Blood Vessels		**Parenchyma**	
ID	Max DV$F_{Model,A}$ (mm)	ϵ_1 accuracy (%)	ϵ_2 accuracy (%)	ϵ_1 accuracy (%)	ϵ_2 accuracy (%)
1	20.30	80.85	90.32	78.93	89.32
2	6.31	98.03	86.86	97.74	85.51
3	8.58	93.83	92.02	89.26	85.63
4	12.12	94.03	95.83	90.96	94.30
5	26.31	75.73	93.87	71.74	92.47
6	14.85	89.31	93.10	75.17	83.89
7	15.68	85.75	90.55	74.07	84.70
8	19.97	87.12	92.52	79.69	89.18
9	17.32	85.33	90.49	69.24	83.41
10	16.99	90.19	95.24	76.72	90.61
11	18.58	95.16	98.27	89.55	98.12
12	20.32	88.25	95.29	79.38	94.20
13	15.53	82.37	90.90	78.58	92.82
14	21.11	82.68	91.00	73.72	87.08
15	15.59	94.20	97.27	88.14	95.43
Av	16.57	88.19	92.91	80.86	89.77

The SSIM, NCC, and MI metrics were used to quantify the similarity between the ground-truth end-inhalation and $DVF_{Model,A}$-deformed end-exhalation images. Table 4-5 shows the SSIM, NCC, and MI for these results. On average, the end-inhalation and $DVF_{Model,A}$-deformed end-exhalation images had an SSIM of 0.89, NCC of 0.97, and an MI of 1.83, indicating high similarity regardless of structural or intensity changes between end-exhalation and end-inhalation images. These numbers were not significantly different from the DIR results shown in Table 4-2, indicating that the accuracy of the elasticity estimation correlates to the accuracy of the underlying ground-truth data.

Table 4-5: Image similarity metrics SSIM, NCC, and MI comparing patient ground-truth end-inhalation images to $DVF_{Model,A}$ deformed end-exhalation images

ID	SSIM	NCC	MI
1	0.95	0.99	1.85
2	0.91	0.97	1.97
3	0.91	0.98	1.86
4	0.87	0.96	2.12
5	0.92	0.98	1.97
6	0.90	0.98	1.94
7	0.92	0.98	1.88
8	0.92	0.99	1.90
9	0.91	0.98	1.73
10	0.93	0.99	2.12
11	0.90	0.97	1.74
12	0.94	0.99	1.54
13	0.92	0.99	1.93
14	0.92	0.98	1.81
15	0.92	0.98	1.61
Av	0.92	0.98	1.86

4.4.3 Validation

The quantitative results of the validation study for the 15 patient lung datasets are now presented. On average, the validation datasets converged with $87.13 \pm 10.62\%$ of voxels within ϵ_1. Table 4-6 denotes the convergence percentages reported according to the two different ϵ values for the validation datasets. The convergence percentages have been separated based on the underlying tissue types. The maximum deformation is also shown.

When compared to Table 4-4, Table 4-6 shows differences in maximum deformation values. On average, the deformation between end-inhalation and end-exhalation breathing phases was 16.57 mm, while the deformation between end-inhalation and mid-exhalation was 6.51 mm. Because the maximum deformation was significantly lower for the validation datasets, the ϵ_2 accuracy decreased. As seen in Table 4-4, the blood vessels had higher accuracy than the parenchymal tissue. Again, this can be explained by the higher signal-to-noise ratio in the blood vessels as compared to the parenchymal tissue. This indicates that the validation error is still skewed by the underlying image quality, which is consistent with the initial results. However, the significantly smaller magnitudes of $DVF_{DIR,B}$ exerted more influence on the overall accuracy of the elasticity estimation than the SNR.

Table 4-6: Convergence percentages for validation datasets

		Blood Vessels		**Parenchyma**	
ID	Max $DVF_{Model,B}$ (mm)	ϵ_1 accuracy (%)	ϵ_2 accuracy (%)	ϵ_1 accuracy (%)	ϵ_2 accuracy (%)
1	4.90	96.17	88.44	92.31	77.01
2	2.24	94.93	84.92	90.87	56.41
3	3.34	93.74	84.38	82.48	58.64
4	4.14	88.13	77.06	78.86	50.81
5	8.85	89.90	87.99	94.77	92.70
6	4.83	96.47	90.49	95.00	75.34
7	9.56	87.88	74.08	72.13	70.10
8	7.08	85.97	83.77	69.06	62.89
9	6.94	83.20	77.40	69.64	58.20
10	8.58	86.31	85.40	55.45	51.88
11	8.50	97.11	97.31	89.63	89.33
12	9.83	85.07	85.42	71.15	71.11
13	5.81	98.39	91.79	96.36	79.63
14	7.26	94.06	89.60	83.67	72.21
15	5.72	96.16	93.04	99.04	97.66
Av	6.51	91.57	86.07	82.70	70.93

Finally, image similarity was investigated for the validation results. Table 4-7 shows the SSIM, NCC, and MI results for the validation model. The end-inhalation and $DVF_{Model,B}$-deformed mid-exhalation images had an SSIM of 0.80, NCC of 0.95, and an MI of 1.85. These numbers are not significantly different from the image similarity achieved in Table 4-5 ($p > 0.05$), validating the accuracy and robustness of the elasticity estimation.

Table 4-7: Image similarity metrics SSIM, NCC, and MI comparing validation mid-exhalation images to $\mathrm{DVF}_{\mathrm{Model,\,B}}$-deformed end-exhalation images to $\mathrm{DVF}_{\mathrm{Model,\,A}}$-deformed end-exhalation images

ID	SSIM	NCC	MI
1	0.87	0.97	1.90
2	0.72	0.86	1.96
3	0.79	0.91	1.88
4	0.72	0.91	1.86
5	0.92	0.99	1.71
6	0.80	0.98	2.00
7	0.80	0.93	1.73
8	0.79	0.90	1.75
9	0.77	0.95	2.00
10	0.76	0.93	2.16
11	0.88	0.96	1.61
12	0.86	0.98	1.78
13	0.78	0.97	2.05
14	0.83	0.98	1.93
15	0.86	0.98	1.77
Av	0.81	0.95	1.87

4.5 Discussion

In this chapter, we presented the results of a lung elastography process performed on 15 4DCT patient datasets. A physics-based biomechanical constitutive model was used as a forward model to solve the inverse elasticity problem. Lung DVFs from end-inhalation to end-exhalation breathing phases were obtained from an in-house optical flow DIR algorithm. The lung boundary displacements were then employed as boundary constraints for the forward model, while the inner voxels of the biomechanical model were allowed to deform according to linear elastic material properties.

Using 15 clinical 4DCT datasets, this study indicated that maximum lung deformation ranged from 6 to 31 mm and 89.91 ± 4.85% of voxels converged within the prescribed metrics. In addition, SSIM, NCC, and MI image similarity metrics showed high similarity between both the end-inhalation and $DVF_{DIR,A}$-warped end-exhalation registration images, and end-inhalation and

$DVF_{Model,A}$-warped end-exhalation experimental results, with average values of 0.89, 0.98, and 1.90, respectively for the DIR results. Similarly, we observed average values of 0.85, 0.97, and 1.83 for the model generated results.

The potential of 4DCT-based lung elastography to be used within a clinical radiotherapy workflow required extensive quantitative validation. Mid-exhalation 4DCT datasets were used as validation datasets so that the elasticity results could be validated in a radiotherapy clinically-relevant manner. The maximum lung deformation of the validation datasets ranged from 2 – 10 mm, and $87.13 \pm 10.62\%$ of voxels converged within 1 mm of ground-truth deformation. Our results indicated that convergence percentages for each of the subjects during the elastography and validation process were similar, citing the quantitative nature with which the process can be used within the context of clinical radiotherapy. The accuracy was observed to be independent of the subject’s lung DVF magnitude, thereby indicating the applicability of such measurements to a wide range of patients and breathing phases.

The average elasticity values obtained for the patient cohort ranged from 4.91 to 7.66 kPa. These values are similar to those seen in the literature [72], especially for patients with diseased lungs [112]. As no ground-truth elasticity distributions are available for accuracy calculations, the accuracy of the elasticity estimation is dependent of the accuracy of the DIR technique and ground-truth DVF values. While we are confident in the capability of our in-house optical flow DIR algorithm, future work will investigate in vivo tissue sample experiments and US/MR elastography techniques for the lung for further verification and validation purposes.

We currently foresee two challenges to the elastography methodology implementation within a radiotherapy setup: image artifacts and computational complexity. Firstly, the lung elastography approach discussed in this study is sensitive to image artifacts in the 4D image dataset. SNR differences due to the underlying tissue slightly affected the elasticity estimation, though the parenchymal accuracy was still greater than 80%. In this study, a 5D imaging protocol was used to acquire the 4DCT images, which eliminated potential elasticity estimation errors arising from 4D imaging artifacts, irregular breathing, and hyperelastic lung behavior. Though we expect 5DCT methods to become more prevalent, in the future, we will investigate ways to ensure elasticity estimation accuracy for 4DCT datasets that are inherent with image artifacts. We envision machine learning techniques as an approach for predicting initial elastic material properties that will be refined with our biomechanical model. The complexity of the inverse elasticity estimation is a computationally intensive problem. The implementation of the methodology on a GPU cluster allowed for the calculation of patient-specific lung elasticity distributions to be completed in about 2 hours.

We foresee a wide range of clinical applications for our elastography method. The novel lung elastography method utilized here is able to directly relate tissue elasticity with the lung tissue deformation derived from clinical radiotherapy datasets. The elasticity information obtained through this methodology can be used to characterize response to radiotherapy and the functionality of the lung tissue on a voxel-by-voxel basis. Functional lung information can lead to patient-specific radiotherapy treatment options. Several authors have reported methods for functional imaging of the lungs for radiation treatment. One example is ventilation imaging, which is generated from the DIR of 4DCT datasets [8, 113, 114]. Ventilation imaging is based on the Jacobian of DVFs, which describe the lung motion. However, ventilation imaging does not take into account the underlying biomechanical properties of the lung tissue [115]. Lung elastography provides critical information about the biomechanical properties of tissue, which have been shown to be related to the underlying lung function and disease. We expect elastography to provide complementary information to current functional imaging techniques. Future work will investigate comparing and integrating elastography and ventilation imaging methods to more fully describe lung function.

Beyond the context of radiotherapy, the elasticity distributions can be used to assess degree of disease in COPD patients, track disease progression, and differentiate between tissue affected by changes in the stiffness, for example, bronchitis and emphysema. Future work will focus on describing and characterizing the lung tissue of patients with different stages of COPD, obtaining more scan time points, and correlating changes in elasticity over time with radiotherapy and disease progression. This will be preliminarily addressed in Chapter 7.

4.6 Conclusion

In this study, we presented the results of a lung elastography study using 4DCT deformation vectors. Patient-specific ground-truth deformation values between end-inhalation and end-exhalation breathing were obtained for each voxel of lung tissue using optical flow deformable image registration. The methodology employed a constitutive physics-based biomechanical model of the lungs that was iteratively deformed according to patient-specific lung boundary constraints. An inverse analysis consisting of a modified Gauss-Newton based binary search optimization scheme was utilized to update the spatial elasticity distribution of the lung tissue according to the discrepancy between ground-truth and model deformation. Our analysis showed that an average of 89.91 ± 4.85% of voxels converged within a prescribed error metric of 10% of maximum deformation. SSIM, NCC, and MI image similarity metrics indicated high similarity between model results and ground-truth deformation. A validation dataset of mid-exhalation breathing phase deformation data converged with 87.13 ± 10.62% of voxels within 1 mm of ground-truth deformation. These results indicate the quantitative accuracy of the elasticity estimation process.

The 4DCT lung elastography methodology investigated here can easily be implemented within a radiotherapy workflow and has potential to improve patient-specific lung cancer radiotherapy treatment options. To further the applications of the elastography methodology, the next chapter will investigate the accuracy of elastography results using reduced dose CT scans.

CHAPTER 5: DETERMINE IF LOW-DOSE CT SCANS CAN PRODUCE RELIABLE ELASTOGRAPHY RESULTS.

Systematic feasibility analysis of performing elastography using reduced dose CT lung image pairs

A version of this chapter is currently being prepared for submission to Medical Physics

5.1 Introduction

COPD is a major cause of disability and the third leading cause of death in the United States [116]. COPD refers to a large group of incurable lung diseases characterized by the persistent reduction of lung function. Changes in lung function are associated with changes in lung tissue biomechanical properties; for example, diseases of the lung that alter lung function often do so by altering the amounts of elastin and collagen of parenchymal tissue, leading to changes in tissue elasticity [19]. Excised tissue studies have shown that localized changes in the biomechanical properties of lung parenchyma precede the initiation and progression of certain lung diseases, including cancer [17, 50]. Knowing the tissue biomechanical properties using in-vivo techniques is emerging as a critical component for improving treatment efficacy and the patient's quality of life. While computed tomography (CT), is commonly used for lung imaging, it does not explicitly present a quantitative characterization of the lung biomechanical properties [93].

Elastography has the potential to inform diffuse lung disease phenotype characterization and staging and treatment response monitoring [117]. In our preliminary work, we demonstrated a novel elastography approach using virtual lung phantoms (Chapter 3) [101]. This methodology was quantified and validated for lung cancer radiation therapy CT scans reconstructed using a published breathing motion model (Chapter 4) [118].

Our elastography estimation method used multiple fast helical CT scans, each delivering 1.2 mSv to the lungs. The original protocol utilized 25, 40 mAs scans, but Thomas et al and O'Connell, et al determined that minima of 10 and 6 scans would be required for ungated and prospectively gated protocols, corresponding to a total effective dose of 12 mSv and 7.2 mSv, respectively [119, 120]. Mettler, et al showed that the published dose range for routine diagnostic CT scans ranges from 4.0 mSv to 18.9 mSv, with an average of 7 mSv [121]. Currently, SPIROMICS studies have employed an effective imaging dose as low as 4.9 mSv in their protocols for acquiring image pairs [122]. Our current technique delivers exposures similar to routine diagnostic CT studies. Diagnostic CT studies are used for human image interpretation while the scans acquired for elastography estimation are used to determine the motion and distortion characteristics of lung tissues during breathing. Therefore, we assessed elastography quality using simulated reduced dose CT scans.

5.2 Materials and Methods

This study used a cohort of CT datasets of 8 radiotherapy patients that were acquired under IRB # 11-000620-CR-00004 at UCLA [95]. The patients underwent a series of 25 fast low dose helical CT scans. The scans were co-registered using DEEDs and the deformation vector fields, along with the breathing amplitude and rate, were used to develop patient-specific breathing motion models (termed 5DCT models) [95]. Exhalation and inhalation, defined as the 5th and 85th percentile tidal volume, were reconstructed using the 5DCT model. Unlike the published 5DCT approach, where multiple deformed scans are averaged to reduce noise, only a single CT scan was deformed to represent these tidal volumes to maintain the noise characteristics of the original fast helical (1.2 mSv) scans, termed the baseline scans.

5.2.1 Low dose CT simulation

Noise was injected in the image domain of the baseline scans to simulate the effects of lower dose scanning. As lowering the tube current is the most direct way of achieving radiation dose reduction, different tube currents were simulated as a way of replicating the additional noise of lower dose scans [123]. The noise injection process used forward projection to estimate raw data [124], calculated appropriate photon statistics, and finally back projected added and filtered noise. The details of this method are described in the Appendix.

For each patient dataset, noise was injected to represent CT scans acquired with reduced tube current-time products of 30, 25, and 20 mAs. The lower limit of 20 mAs was selected to match the lower end of lung cancer screening and emphysema detection programs [123].

5.2.2 Image registration

The model-guided elasticity approach presented in this study relies on DVFs extracted from deformable image registration (DIR) of exhalation and inhalation breathing phases. The lungs were segmented using an intensity thresholding approach, and the two breathing phases were deformably registered using a well-validated in-house multi-level optical flow DIR algorithm [94]. The DVFs of the baseline images were taken to be the ground-truth displacement for the elasticity estimation process.

5.2.3 Elasticity estimation

The elasticity estimation process has been systematically studied and validated for the lung in [101, 118]; for clarity, the process will be summarized briefly here. The inverse elasticity problem was formulated as a parameter-optimization problem with an objective to determine the elasticity parameter that would minimize the difference between ground-truth (registration) DVFs and those computed by a constitutive biomechanical model [52]. Solving the inverse elasticity problem was conducted in two steps: 1) estimating the DVF for every voxel of lung tissue for a given elasticity distribution and boundary constraint using a biomechanical model, and 2) optimizing the elasticity distribution to best reproduce the registration ground-truth DVF.

The elasticity results derived for the baseline CT scans will be considered ground-truth and used for comparison to the lower mAs results.

5.2.4 Quantitative analysis

As a first measure of quantitative analysis, the displacement results from each of the lower mAs model-guided elasticity estimations were evaluated and compared with those obtained with the baseline CT scans. The comparison was first performed using average and maximum values. Absolute error between the distributions was then calculated by subtracting the lower mAs DVFs from the baseline DVFs. We then computed the number of voxels whose estimated DVF errors were less than 0.5 mm or 1 mm. Equivalent analyses were conducted for the elasticity estimates, with an error threshold of 0.5 kPa or 3 kPa.

For further elasticity analysis, underlying elasticity values were split into low elasticity, representing voxels with elasticity values between 1 and 3 kPa, mid elasticity, representing voxels with elasticity values between 3 and 6 kPa, and high elasticity, representing voxels with elasticity values greater than 6 kPa, subgroups. The error within each of the elasticity ranges is relevant since parenchymal tissue, specifically diseased parenchymal tissue, is known to have low elasticity values.

In addition to the previous evaluation, the Normalized cross-correlation (NCC) image similarity metric was used to further assess the results of our study. NCC was explained in §4.2.5.2 in the previous chapter.

5.3 Results

5.3.1 Low dose CT simulation

Figure 5-1 shows an example of a baseline exhalation lung scan (a), a simulated 30 mAs lung scan (b), and a simulated 20 mAs lung scan. The reduced dose images are noisier than the baseline image, as expected.

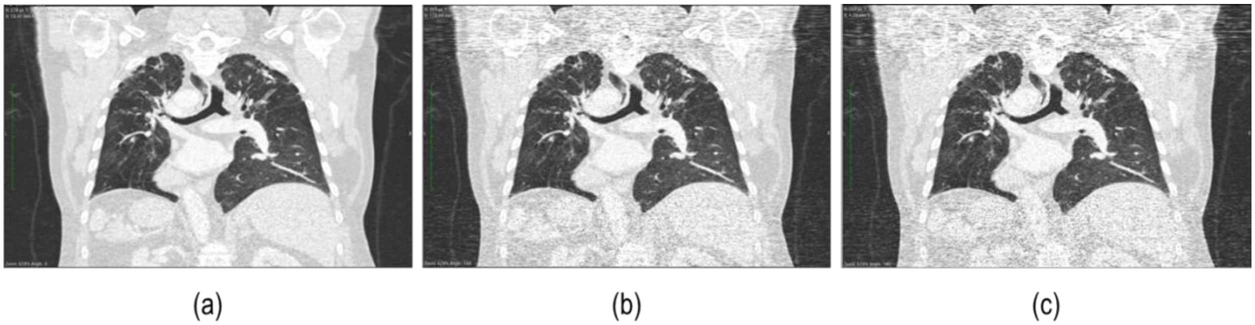

Figure 5-1: Example of exhalation baseline (a), 30 mAs (b), and 20 mAs (c) scans

5.3.2 Image registration

An example of the registration results for both a baseline and 20 mAs scan pair is shown in Figure 5-2. Figure 5-2(a & c) show the exhalation superimposed with inhalation. Mismatches can be seen between the exhalation and inhalation images, especially near the base of the lung. Figure 5-2(b & d) show the overlay between the warped exhalation and inhalation images. The registration accounts for the lung deformation well, with little mismatch seen between the warped end-exhalation and end-inhalation images, for both the baseline and reduced mAs scans. The registration accuracy visually appears to be similar, regardless of injected noise.

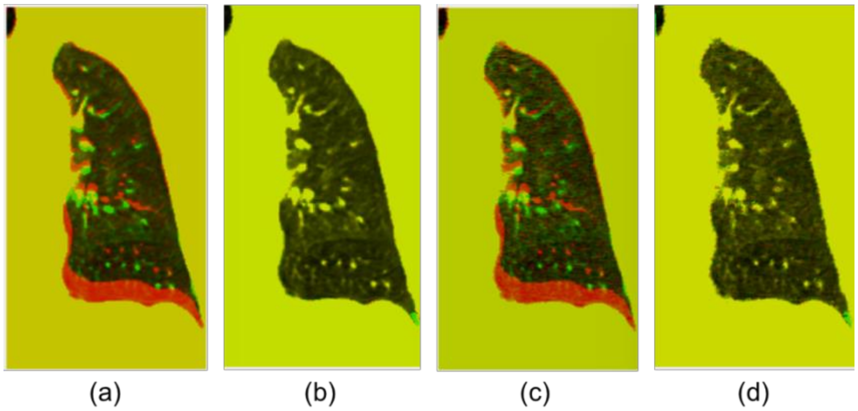

Figure 5-2: Example of registration for baseline (a & b) and 20 mAs (c & d) CT scans. (a&c) show the exhalation in green overlain with inhalation in red. (b & d) show the warped exhalation in green with inhalation in red

5.3.3 Quantitative analysis

Table 5-1 shows the maximum and average displacements for the baseline, and simulated reduced mAs scans for all patients. For each dataset, the model-generated displacement vectors were compared with the registration-generated ground-truth displacement vectors, and the average displacement error and percent of voxels with error less than 1 mm and 0.5 mm were tabulated.

Table 5-1: Displacement results for original, and dose reduced scans

Average	Maximum Displacement (mm)	Average Displacement (mm)	Average Displacement Error (mm)	Error < 1 mm (%)	Error < 0.5 mm (%)
Baseline (40 mAs)	13.79	4.89	0.42 ± 0.31	84.02	65.08
30 mAs	12.01	4.08	0.52 ± 1.52	85.03	65.27
25 mAs	13.72	4.27	0.53 ± 1.53	84.96	63.91
20 mAs	12.46	4.21	0.56 ±1.56	84.00	62.08

For each reduced mAs value, the corresponding percent differences relative to baseline were tabulated, as shown in Table 5-2. It can be seen that the displacement metrics obtained for all three mAs levels were quite similar to the baseline scans. The error increased most at 20 mAs, but none of the differences were statistically significance.

Table 5-2: Percent difference between the values for the baseline and reduced mAs scans

Percent differences (%)	**Maximum Displacement (%)**	**Average Displacement (%)**	**Error < 0.5 mm (%)**
30 mAs	12.85	16.39	0.30
25 mAs	0.44	12.61	1.80
20 mAs	9.62	13.76	4.61

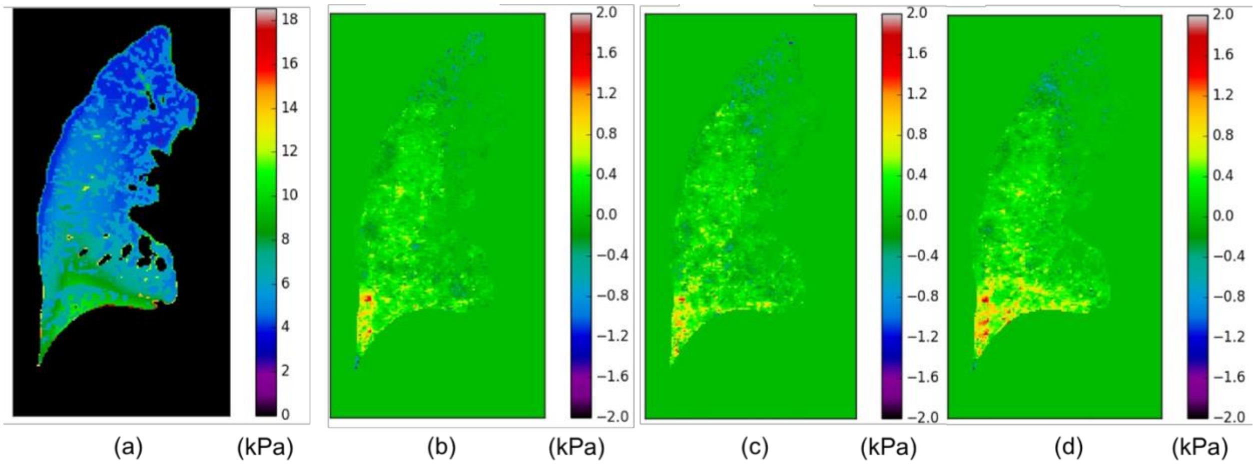

Figure 5-3: Estimated elasticity distribution in kPa for baseline CT scan (a). Absolute difference between baseline and 30 mAs (b), 25 mAs (c), and 20 mAs (d) scans.

Figure 5-3(a) shows the estimated elasticity distributions for the baseline CT scan. Figure 5-3(b - d) shows the absolute elasticity difference between baseline scan and the 30 mAs (b), 25 mAs (c), and 20 mAs (d) scans. On average, the error was less than 0.62 kPa, which is small compared to the average lung elasticity of 6.59 kPa. This is further illustrated in Table 5-3 below. Table 5-3 quantitates the elasticity error between that estimated from the baseline and reduced mAs scans. Maximum elasticity error, average elasticity error, and error less than 0.5 and 3 kPa are listed for each dose reduction. The elasticity error increases as the dose is reduced, however even with a current-time product of 20 mAs, the average elasticity error remained less than 0.76 kPa. A two-sample t-test showed that all of the tabulated values for the simulated 20 mAs scans were not significantly different than the baseline elasticity values.

Table 5-4 shows the percentages of voxels in which the low dose elasticity estimations converged within 1 kPa of the baseline elasticity estimation results, binned by underlying elasticity value. It can be seen that the high elasticity bin had the most error. Since lung diseases, such as diffuse lung disease and COPD, are known to be associated with lower than normal values, this result supports the fact that low dose CT elastography can be performed accurately for these patients.

Table 5-3: Elasticity error results between the baseline estimated elasticity and reduced mAs estimated elasticity.

	Maximum Elasticity Error (kPa)	Average Elasticity Error (kPa)	Error < 0.5 kPa (%)	Error < 3 kPa (%)
30 mAs	7.25	0.65	75.56	92.44
25 mAs	6.96	0.71	71.46	92.27
20 mAs	7.40	0.76	68.07	91.70

Table 5-4: Elasticity errors for low, mid, and high elasticity bins for each low mAs simulation.

	Low elasticity error < 1 kPa (%)	Mid elasticity error < 1 kPa (%)	High elasticity error < 1 kPa (%)
Average	95.81	94.13	63.81
30 mAs	96.85	94.95	66.86
25 mAs	95.67	94.11	63.99
20 mAs	94.91	93.32	60.59

Table 5-5 shows the NCC values between a) the reduced mAs and baseline ground-truth displacement, b) the reduced mAs and baseline estimated elasticity distributions, and c) the reduced mAs ground-truth and model displacement. The reduced mAs displacement values were similar to the baseline displacement values, with similarity decreasing with decreased mAs as expected. However, the estimated elasticity distributions were similar in all cases, as were the ground-truth and model displacements for each mAs reduction. This demonstrates that low dose CT-based model displacements can be used to characterize lung tissue deformations during breathing.

Table 5-5: Image similarity metrics between the baseline and reduced mAs ground-truth displacement, baseline and reduced mAs elasticity, and reduced mAs ground-truth and model displacement

NCC	Low mAs displacement v. baseline displacement	Low mAs estimated elasticity v baseline estimated elasticity	Low mAs ground-truth displacement v low mAs model displacement
30 mAs	0.987	0.977	0.986
25 mAs	0.984	0.975	0.986
20 mAs	0.984	0.973	0.985

A two-sample t-test shows that the NCC values for 30 mAs, 25 mAs, and 20 mAs were not significantly different, illustrating that current-time product could be reduced to as low as 20 mAs and still provide equivalent elastography results.

5.4 Discussion

In this study, low mAs CT scans were simulated using a noise injection process in order to determine the effect of noise on our lung elastography process. Simulated scans with tube current-time products representing 30 mAs, 25 mAs, and 20 mAs were investigated. The results of the baseline scans and low mAs simulated scans were not significantly different, indicating that low dose CT scans could produce reliable elastography results. Since the baseline scans were taken with mAs of 40 mAs and an effective dose of 1.2 mSv, this suggests that the effective dose could be reduced to about 0.6 mSv per scan while still obtaining useful elastographic information.

We foresee a few limitations to this study. Firstly, the noise injection code assumed no tube current modulation, which is not typically employed in radiation therapy but is often employed for diagnostic purposes. The algorithms to select tube current modulation are proprietary and depend on the capability of the x-ray generator, which place limits on the slew rate of the tube current. The lack of modulation creates increased noise at the top or bottom of the image as the shoulders or abdomen starts to appear. However, as the parenchymal tissue is located near the center of the image on the chest CT, we believe these artifacts will not affect the parenchymal registration process. Secondly, the quality of the elastography results depend on the quality of the deformable image registration, which is affected by the addition of noise. There is a need to investigate registration algorithms that are more robust to high imaging noise, which will be addressed in future work. Thirdly, we employed image domain-based noise injection which is not as accurate as noise injection in the raw data domain [125]. As shown in the Appendix, the image domain based noise injection generated results that closely match experimental data. Future work will focus on extending the noise injection technique to the raw data domain, and performing more water tank scans to ensure the accuracy of the results.

5.5 Conclusions

Our study suggests that pairs of CT scans acquired with as little as 20 mAs each could be used to reliably perform elastography, exposing the patient to a total dose of 1.2 mSv, substantially less than the average diagnostic CT effective dose. These results indicated the feasibility of performing elastography using low mAs CT scans, expanding the potential of CT-based elastography.

CHAPTER 6: UTILIZE BIOMECHANICAL MODEL AND DEFORMATION VECTOR FIELDS TO OBTAIN LIVER ELASTICITY INFORMATION FROM 4D IMAGING.

Estimation and validation of patient-specific liver elasticity distributions derived from 4DMR for radiotherapy purposes

A version of this chapter has been submitted for publication as a manuscript to Biomedical Physics and Engineering Express

6.1 Introduction

Hepatocellular carcinoma (HCC) is one of the most common malignancies, and the third most common cause of cancer-related death worldwide [126, 127]. Surgical resection and liver transplantation are the primary treatment methodologies, however strict criteria limit the pool of eligible patients for both cases. HCC has a poor prognoses, with a 5-year survival rate of less than 12% due to a combination of late diagnosis and lack of efficient therapies for advanced stages [128]. Stereotactic body radiotherapy (SBRT) has been used to treat patients with HCC who are not eligible for other treatments [129]. SBRT uses advances in imaging and conformal radiotherapy to deliver ablative, high dose radiation in order to optimize local control. Radiation-induced liver disease (RILD) is a significant limiting factor in the use of SBRT because there are no effective treatments or predictors [127]. Most patients with HCC have pre-existing cirrhosis or hepatitis, which increases their risk of RILD [130]. Baseline liver function is thought to be the most important factor associated with risk of RILD [126]. Pre-treatment visualization of liver function in vivo is necessary in order to expand the use of SBRT for HCC.

The liver plays a role in metabolism, synthesis, secretion, immunity, and many other functions [131]. Liver disease, including cirrhosis, fibrosis and tumors, can disrupt the functions of the liver by altering the biomechanical properties of the tissue, most notably by changing the tissue stiffness [132, 133]. Clinically, elastography provides a measurement of liver stiffness and is a predictor for HCC [134]. Magnetic resonance elastography (MRE) can noninvasively and quantitatively assess the elasticity characteristics of soft tissue [132]. Liver stiffness measured by MRE has been shown to correlate well with histologic staging of fibrosis and differentiation of benign and malignant liver lesions [135]. However, current MRE techniques require equipment that is not typically available within a radiotherapy setup.

Recently, an MR guided radiation therapy (MRgRT) system (MRIdian System™, ViewRay™, Cleveland, OH, USA) was introduced in the field of radiotherapy (RT) [136]. The ViewRay system integrates a 0.35T MRI with three Cobalt-60 sources, which allows for simultaneous MRI acquisition and treatment delivery for a variety of malignancies [137]. The superior soft tissue contrast from Viewray's on-board MRI enables soft tissue based gated RT and on-line adaptive RT. Both techniques are especially helpful for treating thoracic and abdominal tumors by accounting for intra-fractional and inter-fractional motion. In this study, we present a novel elastography process for estimating liver tissue elasticity using 0.35 T 4DMRI to observe liver deformation in each respiratory cycle during patient simulation. The rest of this chapter is organized as follows: section 6.2 introduces the methods employed for the deformable imaging registration, elasticity estimation, validation, and quantitative evaluation. Section 6.3 presents the qualitative and quantitative results of the deformable image registration, elastography, and validation processes. Section 6.4 presents a discussion of the results and highlights the areas for continued research, while section 6.5 concludes the chapter.

6.2 Methods

Our elastography process focuses on estimating the effective Young's modulus for each voxel of liver tissue using 4DMR liver data. Figure 5-1 shows a flow chart summarizing the elasticity estimation. First, phase 1 and phase 8 datasets from the 4DMR liver images were registered using an optical flow deformable image registration (DIR) algorithm [94]. Liver deformation vectors (DVFs) were obtained for every voxel of liver tissue. The biomechanical model was then assembled using segmented phase 1 liver geometry and a randomly initialized elasticity distribution. Using the ground-truth liver DVFs, the elasticity distribution was optimized. The inverse elasticity problem was formulated as a parameter-optimization problem with an objective to determine the elasticity parameter that would minimize the difference between the ground-truth deformation and the deformation computed by a biomechanical model. The biomechanical model and inverse elasticity estimation was implemented on a GPU cluster, which allowed the elasticity estimation for each patient dataset to converge in around 2 hours. Spatial elasticity and displacement error distributions were then obtained and validated.

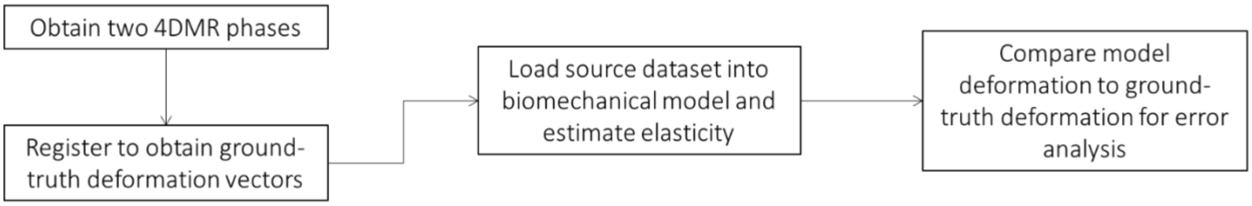

Figure 6-1: Flow chart describing the liver elastography process. Two 4DMR liver phases are registered and ground-truth deformation vectors are obtained. A biomechanical model is used to obtain an optimal elasticity estimation and error analysis.

In this section, we first briefly present the 4DMR acquisition process and the DIR technique used to obtain the ground-truth DVF. Next, we present the constitutive model and convergence criteria used for the elasticity estimation process. We then describe a technique that was used to validate the estimated elasticity. We conclude the section with a discussion of the metrics used to evaluate the quantitative accuracy of the elasticity estimation and validation results.

6.2.1 4DMRI acquisition.

The study was approved by our institutional review board and each patient provided written informed consent. Eleven patients with tumors in the liver treated on Viewray were included in our study. The MRI study was performed immediately after high resolution 3D MRI simulation acquisition. The 4DMRI sequence parameters are: TE/TR=3.0/6.0ms; bandwidth=400Hz/pixel; FA=110°; field-of-view=500x350x200mm, resolution=1.3x1.3x1.8mm^3, acquisition time = 7min. No specific breathing instruction was given to the subjects during the MRI exam.

6.2.2 Deformable image registration.

The model-guided elasticity approach presented in this chapter relies on displacement values extracted from DIR of 4DMR datasets. 4DMR datasets were acquired from 4DMR ViewRay (MRIdian System™, ViewRay™, Cleveland, OH, USA) scans taken within a radiotherapy setup. The 4DMR datasets were separated into phases according to diaphragm position. The liver was segmented and phase 1 datasets, corresponding to end inspiration, and phase 8 datasets, corresponding to end expiration, were then deformably registered using a well-validated in-house multi-level optical flow DIR algorithm [94]. The resulting DVFs were taken to be the ground-truth displacement for the elasticity estimation process. For the rest of the chapter, the phase 8 datasets will be considered the source images, the phase 1 datasets will be considered target images, and the phase 8 datasets deformed according the ground-truth DVFs will be considered warped images.

6.2.3 Elasticity estimation.

The inverse elasticity problem was formulated as a parameter-optimization problem with an objective to determine the elasticity parameter that would minimize the difference between ground-truth DVFs and those computed by a constitutive biomechanical model, as described in the previous chapters. Solving the inverse elasticity problem was carried out in two steps: 1) estimating the DVF for every voxel of liver tissue for a given elasticity distribution and boundary constraint using the biomechanical model, and 2) optimizing the elasticity distribution to best reproduce the ground-truth DVF. These steps will be further explained in the following sections.

6.2.3.1 Biomechanical model. The first step requires a forward biomechanical constitutive model. The model presented in this section is focused on computing the liver tissue deformation for a give boundary constraint arising from the ground-truth DVF. This model has been previously described for the head and neck, breast, and lung anatomies in [52, 60, 101, 118] but will be summarized briefly here. This approach is appropriate for our current study since it's applicability has been systematically investigated for breathing motion, which is the main factor in diaphragm-induced liver deformations [138].

The biomechanical liver model was assembled from the segmented 4DMR phase 8 dataset. Our approach uses linear elastic constitutive laws that were implemented because of the quasi-static tissue response of liver tissue to small diaphragm-induced deformations [139]. The elasticity optimization process was repeated similarly to that described in chapters 2, 3, and 4.

6.2.4 Quantitative evaluation and validation.

The convergence metrics utilized in this study are critical to interpreting the results. At each iteration of the elasticity estimation, the resultant model DVF was compared to the ground-truth DVF. The percent accuracy, p_ϵ was then tabulated as described in §4.2.4. The convergence criteria was formulated to be 1 mm, the current standard for DIR-based targeting errors for liver SBRT dose planning purposes [140].

An additional error metric was necessary in order to ensure the precision of the estimated elasticity. Specifically, we needed to ensure that the estimated elasticity and displacement distributions could be used to warp the phase 1 liver dataset to closely represent the phase 8 image. Furthermore, the accuracy of the ground-truth data needed to be more fully quantified. For this purpose, normalized cross-correlation was used as an imaging metric to quantify accuracy between both the target and warped images along with the model-deformed and ground-truth deformed images. Normalized cross-correlation was used because it has been found to be an accurate similarity measurement for the registration of soft tissue, and is unaffected by intensity changes [141].

A key part of our focus is to validate the estimated elasticity using clinical datasets. However, patient-specific elasticity distributions have not been previously documented in the literature. For validation purposes, deformation vectors from the phase 4 datasets (representing mid-expiration breathing phase) that were not used for the elasticity estimation were employed. The accuracy of the elasticity distribution derived from phase 1 and phase 8 datasets was quantified by its' ability to also represent the phase 4 liver data. To further ensure the quantitatively evaluate the precision of the DIR and the estimated elasticity, normalized cross-correlation (NCC) was used as an image similarity metric between two sets of images for both the estimation and validation process: first between the target and warp images used in the deformable image registration, and second between the target image and model-deformed images.

6.3 Results

In this section, we first present the qualitative DIR results, followed by qualitative elasticity estimation and validation results. Finally, we present the quantitative results for the respective sections.

6.3.1 Deformable image registration.

The accuracy of the DIR results is necessary to ensure the validity of the ground-truth deformation data. Figure 6-2 illustrates an example of the DIR for a 2D-slice of 4DMR data. Figure 6-2(a) shows the source data (phase 8 dataset) in red overlain with the target (phase 1) data in green. Mismatches can be seen between the source and target, especially near the diaphragm and liver boundaries. Figure 6-2(b) shows the target data is red overlain with the warped source data in green. It can be seen that the registration accounts for the liver deformation well, with little mismatch seen between the target and warp images. The extent of the registration accuracy will be further quantified in a following section.

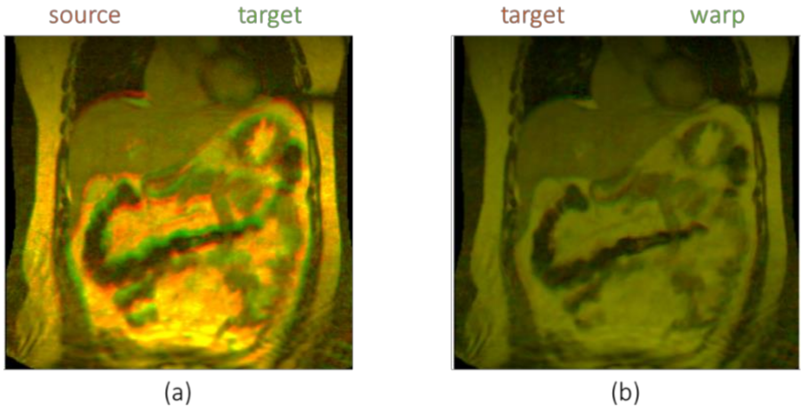

Figure 6-2: Example of the registration results achieved with our in-house optical flow algorithm. The source (red) and target (green) were registered (a), resulting in the warped image that is overlain with the target in (b).

6.3.2 Elasticity estimation.

Figure 6-3 shows the displacement accuracy corresponding with a resultant elasticity map for a 2D-slice of patient liver. Figure 6-3(a) shows the source image of a segmented liver. Figure 6-3(b) shows the ground-truth displacement derived from DIR in mm, while Figure 6-3(c) shows the optimized model displacement, also in mm. Figure 6-3(d) shows the displacement error between 6-3(b) and 6-3(c), with error greater than 1 mm highlighted in blue. Finally, Figure 6-3(e) shows the optimized elasticity distribution. The low error supports the validity of the error estimation. Furthermore, regions of high elasticity correspond to apparent liver lesions seen in Figure 6-3(a).

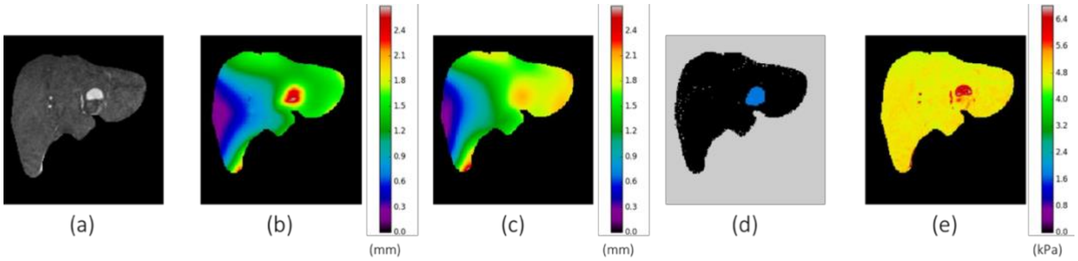

Figure 6-3: Example of elasticity estimation results. (a) source, (b) ground-truth displacement in mm, (c) model displacement in mm, (d) displacement error in mm, and (e) estimated elasticity in kPa

6.3.3 Quantitative evaluation and validation.

Table 6-1 indicates the average elasticity, displacement, and accuracy for both the estimation and validation for each patient dataset.. Overall, 95% of voxels converged within 1 mm of ground-truth. The average elasticity ranged from 2.69 kPa to 6.42 kPa. The maximum deformation ranged from 3.73 mm to 9.04 mm. Variations in the liver physiological factors, such as range of motion, did not affect the accuracy, indicating the applicability of the elastography process to a wide range of patients.

As no ground-truth elasticity distributions are available for absolute elasticity accuracy calculations, validation was performed using phase 4 (representing mid-expiration breathing phase) 4DMR liver data. To illustrate the validation process and results, we present Figure 6-4.

Table 6-1: Elasticity estimation and validation results for 11 patient datasets

	Estimation			**Validation**	
Patient	Elasticity (kPa)	Maximum Displacement [142](mm)	Error < 1 mm (%)	Maximum Displacement (mm)	Error < 1 mm (%)
1	5.88	9.04	71.34	7.88	53.10
2	2.69	5.10	98.88	5.08	97.94
3	5.91	4.96	97.61	3.05	86.94
4	6.16	6.29	94.64	3.76	91.42
5	4.90	6.30	98.97	5.83	85.61
6	6.26	8.60	99.13	6.56	88.22
7	6.42	6.61	96.17	5.71	95.07
8	5.80	7.64	96.35	5.73	69.92
9	4.44	3.73	100	2.79	100
10	5.28	3.99	99.98	2.59	99.584
11	5.06	6.34	96.61	6.20	76.67
AVG	5.34	6.23	95.43	5.02	85.86

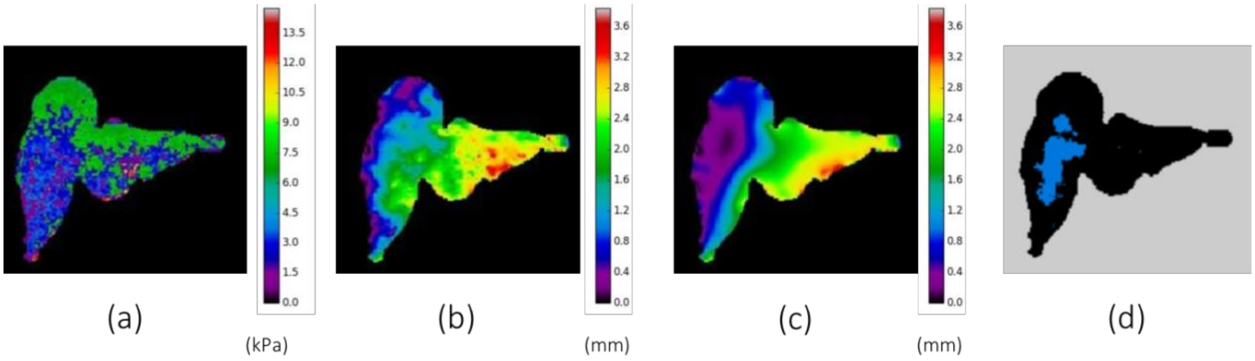

Figure 6-4: Example of validation results. (a) estimated elasticity, (b) validation displacement, (c) model displacement using estimated elasticity for a scaled number of iterations, and (d) displacement with error greater than 0.3 mm highlighted in blue.

Figure 6-4(a) shows the elasticity estimated from the ground-truth displacement vectors. Figure 6-4(b) shows the validation displacement acquired from deformable image registration between phase 1 and phase 4 images. Figure 6-4(c) shows the resultant model displacement in mm after the liver biomechanical model is deformed with the elasticity seen in Figure 6-4(a). Figure 6-4(d) shows the displacement error between (b) and (c), with error greater than 0.3 mm highlighted in blue. A majority of the voxels converged with high accuracy, illustrating the estimated elasticity's validity in representing different 4DMR phases. The validation results are also quantitated in Table 6-1; maximum deformation ranges from 2.59 to 7.88 mm, and average accuracy is 86%.

Finally, image similarity results are presented in Table 6-2 below. On average, the deformable image registration had an accuracy of around 0.97 for both the estimation and validation processes. The resultant model-deformation represented the ground-truth deformation with a similarity of 0.97 for the estimation process and 0.90 for the validation process.

Table 6-2: Image similarity metric normalized cross-correlation between target (phase 1) and warp (deformed phase 8) data and optimized model deformation and ground-truth deformation for both estimation and validation results

	Estimation		**Validation**	
	Target → Warp	Model DVF → Ground-truth DVF	Target → Warp	Model DVF → Ground-truth DVF
1	0.941	0.978	0.952	0.866
2	0.966	0.861	0.967	0.779
3	0.982	0.972	0.977	0.931
4	0.979	0.944	0.977	0.795
5	0.974	0.993	0.973	0.947
6	0.972	0.982	0.977	0.949
7	0.974	0.953	0.972	0.896
8	0.973	0.994	0.984	0.912
9	0.963	0.993	0.965	0.952
10	0.954	0.995	0.961	0.916
11	0.966	0.990	0.973	0.971
Average	0.968	0.969	0.971	0.901

6.4 Discussion

In this chapter, we presented the results of a liver elastography process performed on 11 4DMR datasets. A physics-based biomechanical model was used to solve the inverse elasticity problem. Liver DVFs from the registration of phase 1 and phase 8 diaphragm positions were obtained using an in-house optical flow DIR algorithm. Liver boundary displacements were employed as boundary constraints, while the inner liver tissue voxels were allowed to deform according to linear elastic material properties.

On average, 95% of voxels for 11 patients converged within 1.0 mm of ground-truth deformation. Maximum deformation ranged from 3.73 to 9.04 mm for the estimation cohort. The average elasticity ranged from 2.69 to 6.42 kPa. The average values found here correspond well with those found in the current work in the field [135, 143, 144]. In addition, an image similarity metric showed high similarity between the phase 8 and warped phase 1 registration and experimental results, with values of 0.97 and 0.97 respectively. Overall, these results suggest that liver elastography can be performed using ViewRay 4DMR datasets for a wide range of patients.

The potential of 4DMR liver elastography to be used in the clinic requires extensive validation. Phase 4 datasets were obtained as a validation cohort so that the elasticity results could be validated in a clinically-relevant manner. The maximum deformation ranged from 2.59 to 7.88 mm for the validation cohort, and 86% of voxels converging within 1 mm of clinical ground-truth deformation. An image similarity metric again showed high similarity between phase 4 and warped phase 1 registration and validation model results, with values of 0.97 and 0.90 respectively. Future work will investigate obtaining MRE data for patients so the elasticity distributions can be more explicitly and quantitatively validated.

We foresee two main limitations to the methodology presented here. First, the linear elastic constitutive model employed in the biomechanical model might be overly simplistic for describing the diaphragm-induced motion of diseased liver tissue. Future studies will focus on expanding to a non-linear constitutive model. Secondly, since the ViewRay implementation at UCLA is relatively new, we only had access to a small number of patients. Future work will focus on collecting more patients for further studying the elastography process along with a multi-modal validation.

6.5 Conclusion

The 95% convergence of the elastography technique presented here indicates the potential for integrating liver elastography directly within the radiotherapy workflow. Elastography of the liver anatomy using (Viewray) 0.35 T MR Scanners has not yet been developed and validated. The elastography process described in this chapter can be implemented within the radiotherapy treatment setup without the need for additional imaging modalities. Elastography information acquired within the radiotherapy setup can lead to improved tissue sparing radiotherapy treatment plans and more precise monitoring of treatment response.

CHAPTER 7: DETERMINE IF LUNG ELASTICITY INFORMATION PROVIDES USEFUL FUNCTIONAL INFORMATION FOR RADIOTHERAPY PATIENTS

A novel imaging biomarker based on patient-specific lung elasticity for characterizing the degree of COPD of lung radiotherapy patients

A version of this chapter has been submitted for publication as a manuscript to The British Journal of Radiology

7.1 Introduction

Despite the heterogeneity of COPD phenotypes, diagnosis is based on symptoms and presence of fixed airflow obstruction, which do not fully reflect the heterogeneous pathophysiological conditions observed in COPD [145] [146, 147]. There is an emerging role for quantitative computed tomography (CT) to assess lung structure and function in the evaluation of pulmonary emphysema [148, 149]. A common method employed for the detection and quantification of the lung function is lung densitometry, where voxels with less than -950 HU are classified as emphysematous tissue; this is measured by the relative area of voxels less than -950 HU and known as RA_{950} [150, 151]. A clear limitation of this method stems from the fact that COPD pathophysiology is related to changes in the tissue mechanics, which are not fully represented by a single quantitative CT [19].

There is a need to characterize COPD pathophysiology by considering the lung tissue mechanics. Peers have investigated characterizing lung function using only the deformation vector fields by computing the voxel-by-voxel expansion and contraction [146]. However, voxel expansion and contraction may not fully explain the complex dynamics of the lungs. Lung function is closely related to the mechanical properties of the lung parenchyma [152]. COPD is characterized by damaged lung tissues with altered mechanical properties and ventilation profiles [153]. For example, the destruction of collagen and elastin fibers in emphysematous tissue decreases the strength and elastic recoil of the tissue, subsequently reducing the elastic modulus [154, 155]. Although the link between lung mechanics and disease initiation and progression has been established, the ability to noninvasively assess disease progression through mechanical property (i.e. elasticity) changes at a regional level has not been investigated. Currently, elastography exists across several modalities including MR and ultrasound, but has not yet been investigated for COPD patients [156] [29].

4DCT images are pertinent for lung elastography as they encapsulate lung tissue motion during breathing [157]. They are also routinely acquired for lung cancer patients that receive radiation therapy [68]. Since a significant portion of lung cancer patients also have some level of COPD, analyzing their 4DCT images for lung elastography could yield critical information regarding the lung tissue elasticity for COPD affected regions. The result of such lung elastography is novel for the field of COPD diagnosis and treatment.

We present a 4DCT-based lung elastography procedure for evaluating lung tissue elasticity in COPD patients undergoing lung radiotherapy treatment. We further correlate the spatial distribution of lung tissue elasticity with the inherent GOLD severity criteria to validate the diagnostic and staging ability of the lung tissue elasticity. From the estimated elasticity distributions, we derived a novel imaging biomarker, $YM_{1\text{-}3}$ that is comparable to the quantitative diagnostic results seen with RA_{950}. The results presented in this chapter support our hypothesis that lung tissue elasticity could lead to an effective biomarker for characterizing spatial lung pathophysiological changes and its heterogeneity can be used for the quantitative evaluation of functional lung regions. In addition, the biomarker presented in this study demonstrates the potential for mechanics-derived elasticity as a biomarker for COPD.

7.2 Methods

7.2.1 Data

A set of 13 patient 4DCT datasets were retrospectively obtained using a novel protocol designed to mitigate image artifacts at UCLA from October 2012 to August 2016 [101]. The patient datasets were acquired with patient consent and approval from the Institutional Review Board of UCLA (IRB #11-000620-CR-00004). The patient cohort consisted of lung cancer patients undergoing SBRT at UCLA. The average age of the patients was 66, five of the patients were male, and eight were female. The 4DCT scans were acquired pre-treatment with the same acquisition protocol on Siemens Definition Flash, Siemens Biograph 64, and Siemens Definition AS 64 scanners with 1 mm slice thickness. Pulmonary function tests were available for all 13 of the patients.

7.2.2 Elastography

7.2.2.1 Biomechanical model. The primary aim of the lung elasticity evaluation for COPD patients was to determine if patient disease status could be correlated with underlying tissue elasticity derived from the 4DCT geometry, boundary conditions, and the deformation vector fields. Integrating the three above-mentioned components using a biomechanical framework enabled to precise characterization of lung tissue elasticity [118]. A biomechanical model that has been well validated using head and neck, breast, and lung datasets was used as a forward model to solve the inverse elasticity problem [52, 101]. Biomechanical property estimations are generated using iterative inverse deformation methods that use biomechanical models to estimate the linear elasticity that duplicates the image dataset deformations [158]. The geometry of the biomechanical model was instantiated using end-exhalation lung datasets, where every image voxel corresponded to a finite element within the model.

7.2.2.2 Elasticity estimation. For the estimation process, an initial density-guided linear elastic distribution was assigned to the biomechanical lung model, associating a discrete elasticity value to every lung tissue voxel. For each patient, end-inhalation and end-exhalation breathing phases were first registered using an in-house optical flow DIR algorithm [94]. The displacement of each voxel was taken to be the ground-truth. The inverse elasticity problem was formulated as a parameter-optimization problem with an objective to determine the elasticity that would minimize the difference between the ground-truth displacement and that computed by the biomechanical model. Lung boundary displacements obtained from the DIR algorithm were used as boundary condition for the elastography analysis to deform the biomechanical model to represent end-inhalation geometry. For changes in the lung boundary, the inner voxels biomechanically deformed according to the linear elastic forces within the biomechanical model. The Euclidean distance between the initial and final position for each voxel was taken to be the model deformation for that voxel.

7.2.2.3 Parameter optimization. A detailed description of the inverse elasticity estimation and underlying parameter optimization has been discussed in [101]. For clarity, we present a brief description of the parameter optimization process. Solving the inverse elasticity problem was carried out by (a) computing the displacement vector field for every voxel of lung tissue for a given elasticity distribution (as discussed above), and (b) optimizing the elasticity distribution that best reproduced the ground-truth [70]. The tissue elasticity was iteratively updated and optimized and the resulting displacement was then compared with the ground-truth DIR displacement until convergence [118].

7.2.3 Lung elasticity evaluation for COPD patients

To evaluate the correlation of disease status with underlying elasticity, the patients were first classified by an experienced physician with a score of 0 – 4 according to the GOLD 2017 standard, where 0 corresponds to no limitation and 4 to very severe airway limitation [159]. The physician had no prior knowledge of the elasticity metrics of the patients. The corresponding 4DCT patient datasets were used to estimate the tissue elasticity and assessed for their ability to discriminate patient COPD status with the following three experiments:

7.2.3.1 Experiment 1: Documenting spatial changes in the elasticity for COPD patients. The spatial elasticity distributions will be analyzed, as COPD should not present homogeneously. In addition, to quantify whether elasticity will provide any more information than traditional displacement, correlations between the tissue displacements and elasticity distributions were analyzed. For similar reasons, correlations between intensity and elasticity distributions were also analyzed.

7.2.3.2 Experiment 2: Investigating changes in elasticity distribution for different stages of COPD patients. An increase in the GOLD criteria reflects a decrease in the lung function – these changes should be evident in the underlying elasticity. Parenchymal voxels were segmented using an intensity thresholding approach [160]. Average elasticity values for parenchymal tissue were correlated with the GOLD criteria to observe for any changes in the lung function. Elasticity histograms were generated for all GOLD scores and also analyzed for change in lung tissue function.

7.2.3.3 Experiment 3: Comparing an elasticity-derived biomarker to RA950. While the elasticity estimation gives a distribution of values, for diagnostic purposes it is convenient to have a binary indicator of disease. A binary COPD classification was first determined based on the GOLD score; a score of 0 or 1 corresponded to a non-COPD (normal) classification (value of 0) and a score greater than 2 corresponded to a COPD classification (value of 1) [161]. These values are listed explicitly in Table 7-1 below.

Table 7-1: Gold score and binary COPD classification for each patient that had pulmonary function testing information available.

Patient ID	GOLD score	Binary COPD Classification
1	1	0
2	1	0
3	2	1
4	3	1
5	4	1
6	0	0
7	2	1
8	4	1
9	2	1
10	2	1
11	2	1
12	0	0
13	2	1

Using these classification methods, 9 of the patients that were included in this study were then classified as having COPD (GOLD 2-4). First, the voxel-to-voxel correlation of the elasticity with RA_{950} was investigated, to determine if the elasticity information could serve as a proxy for COPD diagnosis. Second, a binary elasticity threshold was empirically derived to discriminate patient COPD status. The relative area of voxels with an elasticity less than the binary elasticity threshold or Young's modulus, YM_{1-3}, was compared to the conventional RA_{950} imaging metric using a confusion matrix and ROC analysis.

7.3 Results

Overall, 89.35 ± 8.16% of voxels converged within 10% of the maximum deformation.

Table 7-2: Convergence results of elasticity estimation study for parenchymal tissue

Patient ID	**Convergence percentage of voxels < 10% maximum deformation (%)**
1	92.85
2	89.32
3	94.11
4	94.70
5	78.75
6	85.51
7	85.63
8	94.30
9	92.47
10	89.18
11	90.61
12	92.82
13	87.08
Average	87.32

Table 7-2 denotes the convergence percentage for each of the patients for parenchymal tissue. 87.32 ± 4.61% of parenchymal voxels converged within 10% of maximum deformation. The high convergence of the parenchymal tissue motivates the use of the elasticity results for the remainder of the experiments.

7.3.1 Experiment 1: Documenting spatial changes in elasticity for COPD patients.

Figure 7-1 (a) shows the ground-truth displacement for a 2D slice of non-COPD patient lung, while figure 7-1(b) shows the resultant elasticity distribution. Figure 7-1(c & d) show the ground-truth deformation and elasticity maps, respectively, for a COPD patient with impaired lung function.

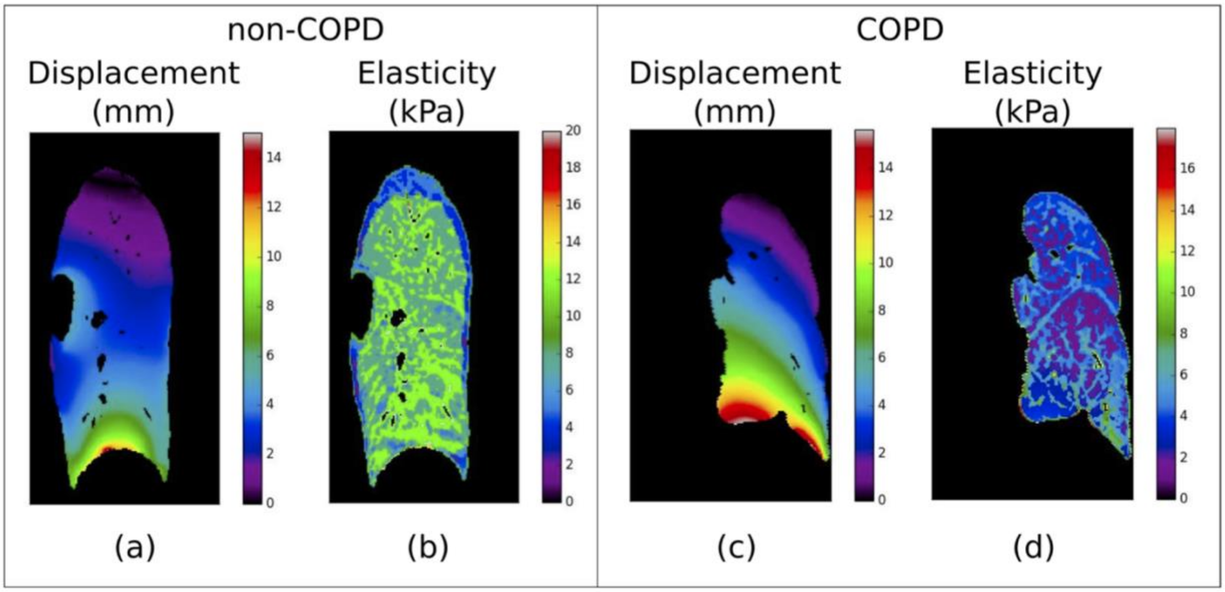

Figure 7-1: 2D slices showing ground-truth displacement (a & c) and reconstructed elasticity distributions (b & d) for normal (a & b) and COPD (c & d) patients respectively.

The patients shown here were chosen in such a way that their maximum ground-truth deformation values were similar. However, the elasticity distributions differ significantly, demonstrating the ability of the proposed method to discriminate normal versus diseased patients. The elasticity of the COPD patient (Figure 7-1(d)) is much lower than that of the non-COPD patient (Figure 7-1(b)), which was expected since COPD is known to affect elastin and collagen in diseased tissue [154], leading to a decrease in strength and elasticity. This supports the hypothesis that the elasticity estimation discussed here can provide useful functional information, which is explored in Experiment 2.

We now present the elasticity distribution as a function of the displacement magnitude as well as the voxel intensity. Table 7-3 denotes the correlation coefficient between both a) displacement and elasticity distributions and b) the intensity and elasticity distributions for each patient.

Table 7-3: Displacement and elasticity correlation along intensity and elasticity correlation results

Patient ID	**Correlation between displacement and elasticity**	**Correlation between intensity and elasticity**
1	0.14	0.76
2	0.02	0.78
3	0.03	0.61
4	0.12	0.87
5	0.02	0.91
7	0.11	0.69
7	0.08	0.83
8	0.04	0.89
9	0.22	0.26
10	0.06	0.80
11	0.02	0.86
12	0.11	0.72
13	0.15	0.85
Average	0.09	0.76

On average, the correlation between elasticity and displacement is low with a Pearson correlation coefficient of 0.09. The low correlation suggests that elasticity is independent of the displacement. Therefore, deriving functional information solely from displacement-based metrics may not be a good representation of the underlying pathophysiology. The correlation between elasticity and intensity was better, with an average coefficient of 0.76. This supports the hypothesis that elasticity is related to intensity and can be used to complement intensity-derived metrics, such as RA_{950}, while still providing additional functional information. This will be further explored in Experiment 3.

7.3.2 Experiment 2: Investigating changes in elasticity distribution for different stages of COPD patients.

Table 7-4 denotes maximum deformation and average elasticity, both for all lung tissue and parenchymal tissue only, for the patients stratified by GOLD score. It can be seen that, although maximum deformation did not have a correlation with the GOLD criteria, average elasticity varied with decreasing lung function. Furthermore, parenchymal average elasticity decreased with decreasing lung function, strongly suggesting that elasticity can provide functional lung information.

Table 7-4: Maximum deformation and average elasticity for GOLD score groups of patients

Patient Averages	Maximum Deformation (mm)	Average Elasticity (kPa)	Average Parenchymal Elasticity (kPa)
All	17.52	6.24	5.87
GOLD 0	10.05	6.55	5.28
GOLD 1	18.30	6.79	7.28
GOLD 2	22.82	6.33	6.06
GOLD 3	19.19	4.32	4.34
GOLD 4	8.92	4.40	4.43

While average elasticity relates to a decrease in lung function, the average is a high-level representation the whole physiology. To evaluate whether the distribution of the elasticity information correlates with lung function, a histogram of the elasticity results for the groups of patients with GOLD status 0 - 4 is shown in Figure 7-2. The peak of elasticity for the patients with normal lung function (GOLD 0 – 1) is significantly further to the right than those patients with COPD (GOLD 2 – 4), which corresponds to the average elasticity values seen in Table 7-3 above. The histograms illustrate that the shift between non-COPD and COPD patients isn't gradual. Specifically, an increase in the GOLD status was characterized by an increase in the number of voxels with an elasticity between 1 and 3 kPa, and a significant decrease in the number of voxels with an elasticity between 4 and 8 kPa. This can be understood by the fact that COPD patients are known to have damaged lung tissue with decreased collagen and elastin content.

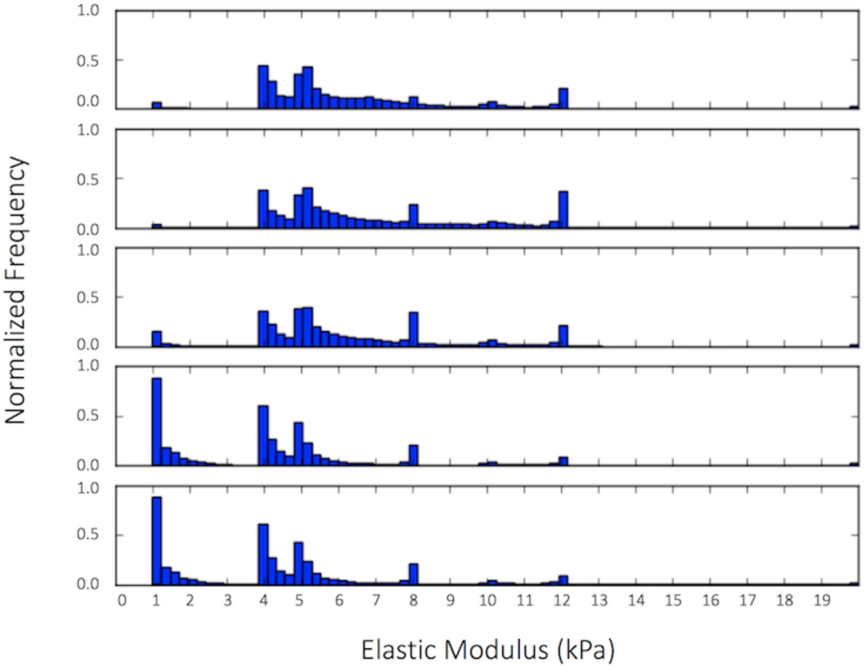

Figure 7-2: Histogram of elasticity values for patients with GOLD scores ranging from 0 (top) to 4 (bottom)

Using this information, we derived a novel elasticity-based imaging biomarker that represents the percentage of parenchymal voxels within 1-3 kPa. Specifically, a new mechanics-based imaging biomarker, YM_{1-3}, represents the percentage of voxels of parenchymal tissue with an elasticity between 1 and 3 kPa. The range of voxels with elasticity between 1 and 3 kPa, will be explored in Experiment 3 below.

7.3.3 Experiment 3: Comparing an elasticity-derived biomarker to RA950.

A visual representation of the RA_{950} imaging biomarker is shown along with the corresponding elastic modulus distributions in Figure 7-3. Figures 7-3 (a-e) show source CT images with HU values less than -950 HU highlighted in red, a visual approximation of RA_{950}. Figures 7-3 (f-j) show the corresponding elasticity distributions for the same slices. Slices are shown for patients with GOLD 0 (a, f) through GOLD 4 (e, j) status. It can be seen that the regions highlighted in red correspond to the lower elasticity regions in purple and dark blue. Furthermore, the prevalence of low intensity regions and the lowered elasticity regions increased with the GOLD status, illustrating that a decrease in the lung function corresponded with a decrease in both intensity and elasticity values.

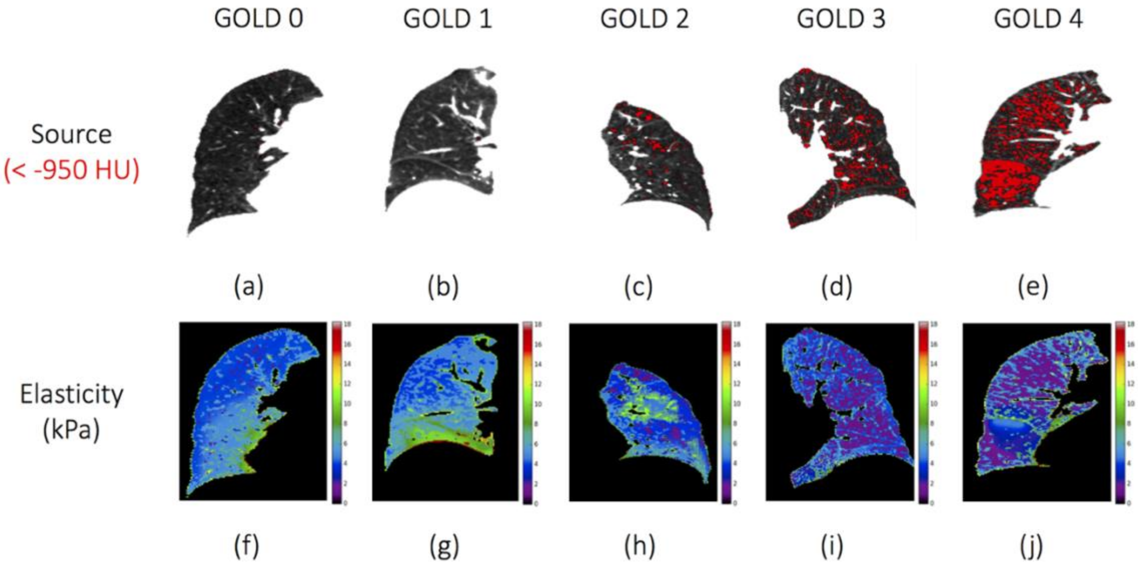

Figure 7-3: Illustration of source CT with HU values less than -950 HU highlighted in red shown for a GOLD 0 (a), GOLD 1 (b), GOLD 2 (c), GOLD 3 (d), and GOLD 4 (e) patient. Elasticity distributions for same patients are shown in (f - j)

The voxels with an elasticity between 1 and 3 kPa are compared to a visual representation of RA_{950} in Figure 7-4. Figure 7-4(a) depicts a source CT image with voxel intensity of less than -950 highlighted in red to illustrate RA_{950}. Figure 7-4(b) shows the reconstructed elasticity distribution, with voxel elasticity between 1 and 3 kPa also highlighted in red. These values were derived from the histogram in Figure 7-2. Many of the highlighted regions overlap between Figures 7-4(a) and 7-4(b), demonstrating the potential of low elasticity values to be indicative of impaired lung function.

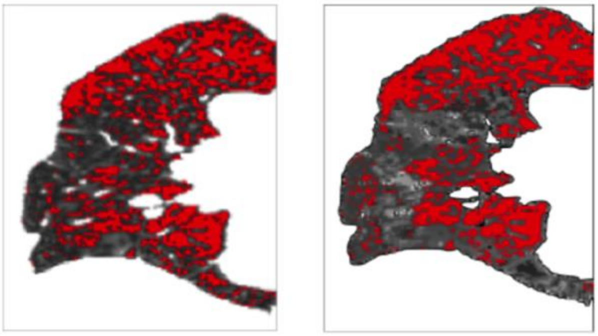

Intensity < -950 HU

(a)

1 kPa < YM < 3 kPa

(b)

Figure 7-4: The conventional RA_{950} imaging metric and an initial elasticity derived imaging metric for the same 2-D slice of a patient left lung.

To further illustrate the diagnostic potential of an elasticity COPD metric, a confusion matrix was used to compare the diagnostic capabilities of $YM_{1\text{-}3}$ versus RA_{950} and is shown for each metric respectively in Figure 7-5 below.

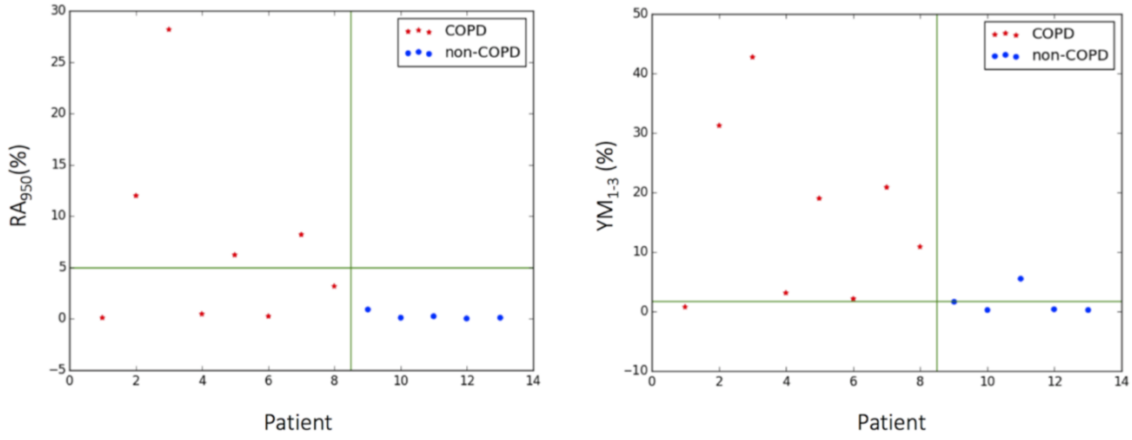

(a)

(b)

Figure 7-5: (a) RA950 for each patient and (b) YM1-3 for each patient. Patients with confirmed COPD are denoted with red stars

Patients with confirmed COPD are denoted with a red asterisk, while patients with normal lung function are denoted with a blue dot. Figure 7-5(a) shows the average RA_{950} value for each patient. We adopted a 5% value of average RA_{950} as a threshold for densitometrically defined emphysema

[162-164]. Figure 7-5(b) shows the average YM_{1-3} for each patient, with the same patient labels as in Figure 7-5(a). A threshold YM_{1-3} of 2% was empirically derived to define emphysema. The upper left quadrant of each figure illustrates the true positives, the right upper quadrant illustrates false positives, the lower left quadrant illustrates false negatives, and the lower right quadrant illustrates true negatives. It can be seen that using a diagnostic criteria derived from RA_{950} results in only 4 true positives, while the remaining COPD patients are misclassified as non-COPD. Conversely, using the elasticity diagnostic criteria, 8 of the 9 COPD patients are correctly classified. All non-COPD patients are correctly classified with RA_{950} while 1 non-COPD patient is misclassified with the elasticity metric.

The statistical measures used to evaluate the two metrics are shown in Table 7-5. The YM_{1-3} metric had a significantly ($p < 0.05$) higher accuracy than RA_{950}. YM_{1-3} was more sensitive as a COPD metric than RA_{950}, but RA_{950} was more specific. Specificity describes the extent to which reported positives represent the condition of interest. YM_{1-3} was less specific than RA_{950} because of the patient who would be falsely identified as COPD-positive, seen in the upper right quadrant of Figure 7-5(b). To evaluate a single metric independent of threshold, the area under the ROC curve (AUROC) was investigated and is also listed in Table 7-5. The AUROC is higher for YM_{1-3} when compared to RA_{950}, which indicated that, for the cases evaluated here, YM_{1-3} classified the patient cases better than the conventional densitometric metric, RA_{950}. This demonstrates that the elasticity is a superior indicator of the underlying lung pathophysiology.

Table 7-5: Statistical measures used to analyze prediction accuracy of the conventional RA_{950} versus YM_{1-3}

Metric	**RA_{950}**	**YM_{1-3}**
Accuracy	0.7142	0.8571
Sensitivity	0.5	0.875
Specificity	1	0.833
AUROC	0.875	0.917

In summary, the aforementioned three experiments demonstrate the ability of lung tissue elasticity to serve as a spatial quantification of disease extent. Furthermore, we demonstrated the ability of the mechanics-based imaging biomarker $YM_{1\text{-}3}$ to guide the diagnosis and staging procedures for COPD patients.

7.4 Discussion

In this chapter, we investigated lung tissue elasticity as a potential imaging biomarker for COPD diagnosis using a set of 13 patients. Accuracy of the elasticity estimation was demonstrated by the high convergence percentages. The elasticity distributions allowed for the depiction of functional lung regions based on lung deformation biomechanics. The mechanics-based biomarker ($YM_{1\text{-}3}$) investigated in this study shows promise for evaluating disease staging and progression, with results similar to and exceeding that of RA_{950} based scoring of COPD.

While the novel mechanics-based metric shows great promise for COPD diagnosis and staging, we would like to highlight two limitations of the current work. First, the input data stems from 4DCT, which is not conventionally used for COPD patients because of its inherently high imaging dose. Currently, SPIROMICS studies have employed an effective imaging dose of 3.2 mSv in their protocols for acquiring the total lung capacity [122]. We anticipate that, with an increasing scope of application for 4DCT in COPD diagnosis and staging, imaging experts will focus on reducing the imaging dose to a level that is within the imaging limits for COPD. For instance, prospective and low dose scanning techniques are being investigated by peers for reducing the 4DCT imaging dose. Once the dose can be reduced for the assessment of COPD, elastography performed using the reduced dose scans (Chapter 5) can be used for a longitudinal assessment of COPD progression and better differentiation of the degree and type of COPD.

Second, the biomechanical model employs a linear elastic approach for the lung elastography. While the linear elastic model is shown to be applicable for COPD lungs during normal breathing, we anticipate that for representing the full range of breathing motion, we will need to employ a hyperelastic process [165]. Furthermore, as MR elastography techniques mature and become more applicable to the lungs, the model-guided elastography will be validated and the YM_{1-3} metric will need to be updated accordingly.

From a radiotherapy perspective, the development of functional tissue-sparing treatment plans guided by the elasticity information will be investigated preliminarily in Chapter 8. A limitation of the patient datasets used in this study is the small sample size that was collected in a radiotherapy setting, so functional information was a byproduct of the radiology reports and no data was available as a healthy control. Future work will focus on collecting and analyzing mainstream COPD data to further evaluate the diagnostic potential. Furthermore, we will investigate the development of a clinical protocol to focus on explicitly validating lung regions affected by COPD with a pulmonary radiologist.

In summary, a novel imaging biomarker was developed using a physics-based biomechanical model and 4DCT-driven lung elastography. A preliminary imaging biomarker for COPD was assessed in comparison to the conventional RA_{950} and performed favorably. The resultant elasticity distributions gained from our methodology can be used to identify functional regions of parenchymal tissue, leading to patient-specific treatment options and guiding pulmonary physicians as to the early management of COPD.

CHAPTER 8: INCORPORATE FUNCTIONAL AND BIOMECHANICAL INFORMATION INTO TREATMENT PLANNING.

Incorporating lung tissue elasticity into function preserving lung SBRT treatment planning

A version of this chapter is being prepared for submission to the British Journal of Radiology

8.1 Introduction

Traditionally the standard of care for lung cancer is surgical resection or radiotherapy [166]. However, these options are often complicated by the presence of co-morbidities, such as COPD or poor respiratory function. Stereotactic body radiotherapy (SBRT) is increasingly accepted as a course of treatment for lung cancer patients who are medically inoperable or declined surgery [167]. SBRT involves precise delivery of ablative doses of radiation over a few fractions.

Radiation pneumonitis (RP) is a common dose limiting toxicity that impacts the treatment of patients with lung cancer. Symptomatic radiation pneumonitis occurs in about 30% of patients irradiated with normal fractionation, and about 9 - 28% of patients treated with SBRT [168]. The high level of radiation exposure during radiotherapy is the primary cause of radiation pneumonitis, but reduced lung function is known to increase the risk of the pulmonary toxicity [7, 169].

Radiotherapy that avoids high-functional lung regions might reduce pulmonary toxicity [4, 170, 171]. The parameters V20 (volume of lung receiving 20 Gy of dose) and mean lung dose (MLD) are commonly used as predictors of radiation pneumonitis [172, 173]. However, dose-volume statistics (such as V20 and MLD) alone are not reliable predictors of radiation-induced change in pulmonary function [3]. Dose-function statistics such as fV20 (volume of functional lung receiving 20 Gy of dose) and fMLD (functional mean lung dose) have been shown to improve toxicity prediction after radiotherapy [6]. Therefore, determining pre-radiotherapy lung function maps in order to minimize radiation damage to the healthy lung is of significant current interest.

To reduce pulmonary toxicity, we hypothesize that it would be clinically beneficial to spare as much functional normal tissue as possible while still ensuring adequate target coverage. This requires knowledge of pulmonary spatial-functional distributions. The derivation of spatial distributions of lung function has been previously proposed using perfusion and ventilation imaging [6-8, 146]. However, the regional physiologic accuracy has not been validated for ventilation imaging, and the use of perfusion imaging is limited by the need for separate imaging sessions or fusion in radiotherapy planning.

Recently, a new biomechanical parameter, the elastic modulus of lung tissue, has been investigated as a way to characterize the functionality of lung tissue [174, 175]. A methodology has been developed to estimate the elastic modulus of lung tissue using 4DCT scans acquired during the radiotherapy workflow (Chapters 3 & 4) [176, 177]. Elasticity information obtained from 4DCT can be used to characterize response to radiotherapy and functionality of lung tissue on a voxel-by-voxel basis [176]. 4DCT-based elastography provides both anatomical and functional information in one scan. Because 4DCT scans are acquired as part of routine care for lung cancer patients, calculating functional information from 4DCT provides spatial functional information without added dosimetric or monetary cost to the patient. This study will investigate the use of elasticity information for retrospectively deriving functional lung contours for SBRT treatment planning purposes. SBRT is uniquely suited to functional avoidance planning because the steeper dose gradients ensure preferential dose deposition outside of functional tissue areas [178].

8.2 Methods

8.2.1 Data

A set of 7 4DCT datasets were retrospectively obtained from patients treated at UCLA from October 2012 to August 2016. The patient datasets were acquired with patient consent and approval from the Institutional Review Board of UCLA (IRB #11-000620-CR-00004). The patient cohort consisted of lung cancer patients undergoing SBRT at UCLA. The average age of the patients was 66, five of the patients were male, and eight were female. The 4DCT scans were acquired before treatment with the same acquisition protocol on Siemens Definition Flash, Siemens Biograph 64, and Siemens Definition AS 64 scanners with 1 mm slice thickness. Artifacts were removed using a novel 5DCT imaging protocol [101]. Pulmonary function tests and patient treatment planning documentation were obtained for all patients. Patient COPD stage was classified by an experience physician based on GOLD 2017 criteria. One patient was classified as stage I COPD, four were classified as stage II, one was classified as stage III, and one was classified as stage IV. All patients were treated at UCLA with SBRT: 5 were treated to a prescription dose of 54 Gy with 3 fractions of 18 Gy, and 2 were treated to a prescription dose of 50 Gy with 4 fractions of 12.5 Gy.

8.2.2 Derivation of functional information

Functional information was derived from spatial distribution of elasticity estimated from the motion observed during 4DCT. A detailed description of the inverse elasticity estimation and underlying parameter optimization has been discussed in [101, 176]. For clarity, we present a brief description of the elasticity estimation process here.

8.2.2.1 Elasticity estimation. A biomechanical model that has been well validated using head and neck, breast, and lung datasets was used as a forward model to solve the inverse elasticity problem

[52, 101]. Lung elasticity was characterized by integrating 4DCT geometry, boundary conditions, and deformation vector fields within a biomechanical framework [118]. Biomechanical property estimates were generated using iterative inverse deformation methods to estimate the linear elasticity that duplicates the image dataset deformations [158]. For each patient, end-inhalation and end-exhalation breathing phases were first registered using an in-house optical-flow deformable image registration (DIR) algorithm and the resultant deformation vector fields (DVFs) were considered ground-truth [94]. The inverse elasticity problem was formulated as a parameter-optimization problem with the objective to determine the elasticity that would minimize the difference between the ground-truth displacement and that computed by the biomechanical model. Solving the inverse elasticity problem was executed by (a) computing the displacement vector field for every voxel of lung tissue for a given elasticity distribution and (b) optimizing the elasticity distribution that best reproduced the ground-truth [70]. The tissue elasticity was iteratively updated and optimized and the resulting displacement was then compared with the ground-truth DIR displacement until convergence [118].

8.2.2.2 Functional contouring. Functional lung tissue was defined to be parenchymal voxels with elasticity between 4 and 8 kPa [177]. Functional lung regions were masked and subsequently contoured. A k-means clustering algorithm was used to derive clusters, and those with a diameter of less than 2 voxels were removed. The masked clusters were then outlined and the contours were added to the radiotherapy structure set and loaded along with the planning CT and original treatment plan into Eclipse v 13.6 treatment planning software (Varian Medical Systems).

8.2.3. Dosimetric evaluation

A key knowledge gap exists in determining whether clinically delivered radiotherapy plans deliver dose to functional lung regions. For these purposes, clinically delivered treatment dose information was acquired, and the dose and elasticity distributions were mapped to each other. The dose volume histograms (DVH) were calculated for the full and functional lung volumes. For each patient, dose volume and dose function metrics, such as MLD, V_5, V_{10}, V_{20} (or the percentage of lung tissue voxels receiving 5, 10, or 20 Gy of dose) and fMLD, fV_5, fV_{10}, and fV_{20} (the percentage of functional voxels receiving 5, 10, or 20 Gy of dose), were calculated and compared.

8.2.4 Retrospective elasticity derived functional avoidance treatment planning

8.2.4.1 Planning. For consistency, both clinical and functional avoidance plans were created for this study. Patients were re-planned both with and without functional avoidance parameters so that the plan differences stemming solely from the functional avoidance technique could be observed. Planning was done using Eclipse External Beam Planning v.13.6 (Varian Medical Systems). Patients were planned to be treated on the Novalis TX with two beam volumetric modulated arc therapy (VMAT). The beam angles were fixed for both the clinical and functional avoidance plans. To be accepted, both plans had to meet the normal tissue and target coverage constraints established according to RTOG 0618 Lung SBRT Dose Volume Objectives for a prescription of 3 x 18 Gy [179] or MD Anderson Lung SBRT Dose Volume Objectives for a prescription of 4 x 12.5 Gy [180]. Functional avoidance treatment plans were designed to selectively avoid irradiating highly-functional lung regions and meet specific dose function constraints while maintaining target coverage and meeting constraints associated with organs at risk (OARs) [113]. The constraints are shown in Table 8-1 below. It should be noted that the constraints for the 4 x 12.5 prescription included more specific volume constraints that were used for planning purposes, but for brevity, have not been included in Table 8-1. The lung dose function constraints were estimated on a case-by-case basis in such a way as to minimize the dose to functional tissue. Samples of lung dose-function constraints are indicated by an asterisk in Table 8-1 below. Both clinical and functional plans were deemed acceptable once they met every guideline the prescription required.

Table 8-1: Dose constraints for SBRT

	RTOG 3 x 18 Gy [179]			**MD Anderson 4 x 12.5 Gy [180]**		
	Volume (%)	Dose (Gy)	Priority	Volume (%)	Dose (Gy)	Priority
PTV	95	54	150	95	50	150
	0	61	100	0	55	100
Cord	0	18	80	0	25	80
Esophagus	0	27	80	0	35	80
Heart	0	30	80	0	45	80
Trachea	0	30	80	0	35	80
Bronchus	0	30	80	0	38	80
Lung	10	20	90	12	20	90
Functional lung*	10	10	120	10	10	120
	20	5	100	20	5	100

8.2.4.2 Plan evaluation. To quantify the impact of functional planning versus anatomical planning, both dose volume and dose function metrics were investigated [181]. Dosimetric parameters will include V_5 – V_{30} and mean lung dose (MLD) and the dose function metrics will include functional V_5 – V_{30} (fV_{5-30}) and functional mean lung dose (fMLD). Mean dose to PTV (normalized to prescription dose), PTV dose homogeneity (maximum dose to PTV/minimum dose to PTV), conformity index (treated volume/PTV), and maximum OAR doses will also be evaluated to determine plan quality.

8.3. Results

8.3.1 Derivation of functional information

As mentioned in §8.2.2 above, functional information was derived from voxel by voxel elasticity distributions for each patient and functional voxels were said to be those with an elasticity value between 4 and 8 kPa, an approximation based on results in the literature [50] and empirically derived from our preliminary results [177]. Table 8-2 lists the COPD stage (classified based on GOLD 2017), average elasticity in kPa, and percentage of lung tissue that is functional for each patient included in this study. It can be seen that the average elasticity is higher for the patients with early (stage I and II) COPD, and that the percentage of functional tissue tends to decrease with increasing COPD stage.

Table 8-2: Functional information for early and late stage COPD patients, including average elasticity in kPa, and percentage of functional lung tissue

COPD Stage	Average Elasticity (kPa)	Functional Tissue (%)
Early (GOLD 1 – 2)	6.58	13.21
Late (GOLD 3 – 4)	4.235	10.67

3.2 Dosimetric evaluation

Figure 8-1 shows a dose map of the original clinical plan for a 2D slice of a patient with early stage (GOLD stage II) COPD. The functional lung tissue is contoured in orange. The functional tissue is located close to the target, resulting in significant functional tissue dose. Figure 8-2 shows the dose volume histogram (DVH) for full lung and functional lung volumes, along with PTV and ITV target volumes, for the same patient. The functional lung receives slightly more dose percentagewise than the full lung volume.

Table 8-3 shows the V_{20}, fV_{20}, MLD and fMLD metrics for all patients with early and late stage COPD. While V_{20} and MLD differed between disease stages, fV_{20} and fMLD differed significantly more. This suggests that early stage COPD patients might be better suited for functional tissue-sparing treatment plans. However, since dose is accumulated in functional tissue in both early and late stage patients, it is necessary to see if functional avoidance treatment planning can be accomplished for all stages of disease.

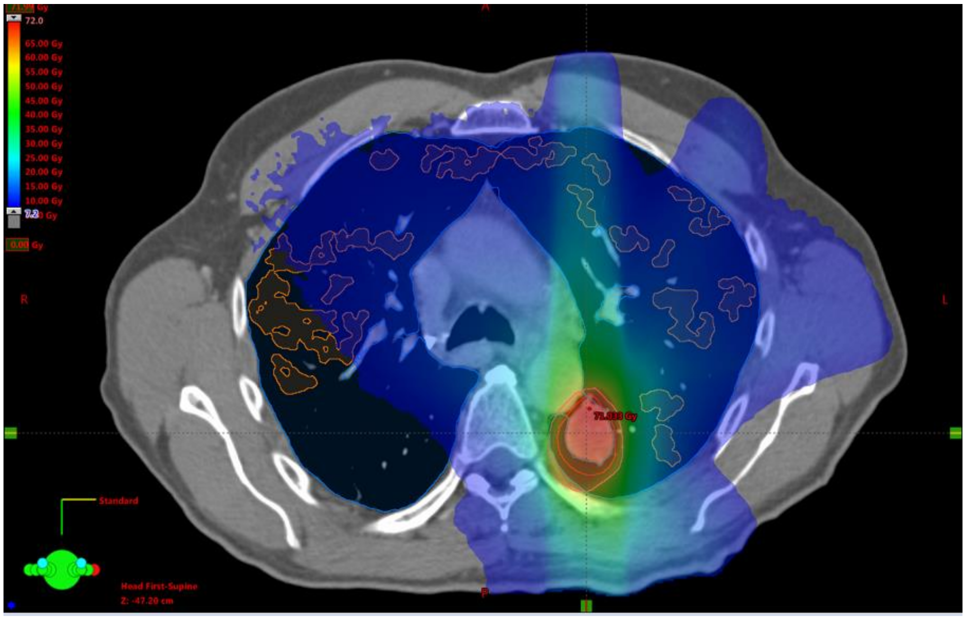

Figure 8-1: Dose wash of patient shown along with contours for functional lung as defined using elasticity

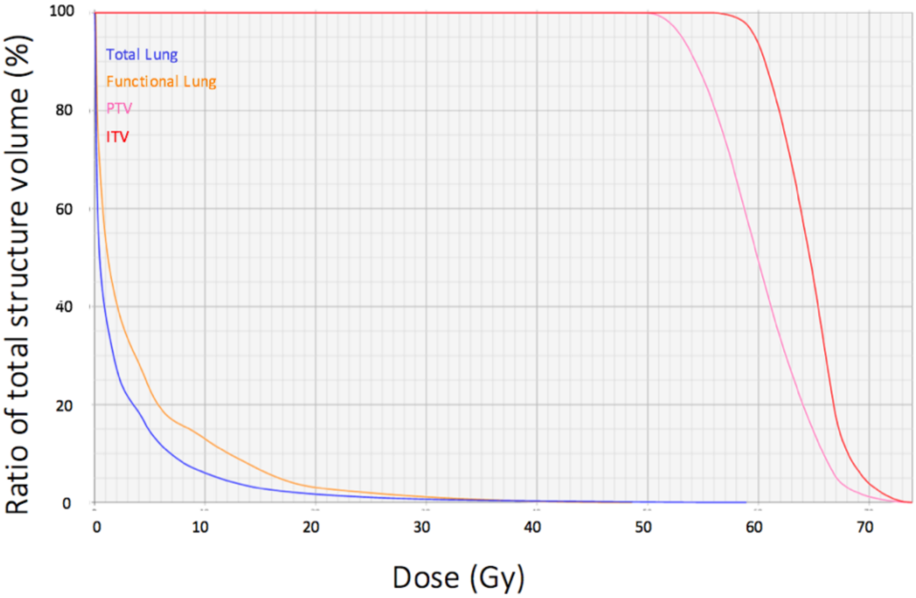

Figure 8-2: Dose volume histogram (DVH) for patient full lung and functional lung volumes, ITV, and PTV

Table 8-3: V_{20}, MLD, fMLD, and fV_{20} metrics from clinically-delivered plans for all patients with early and late stage COPD

Patient COPD stage	V_{20} (%)	fV_{20} (%)	MLD (Gy)	fMLD (Gy)
Early Stage	9.67	10.77	7.40	8.42
Late stage	3.24	0.92	3.14	1.53

3.3 Functional avoidance treatment planning

8.3.3.1 Planning. New clinical and functional avoidance treatment plans were created for each patient using according the guidelines shown in §8.2.4.1 above. In every case, the functional plans met the normal tissue constraints as well as or better than the clinical plans.

An example of both clinical and functional treatment plans for a patient with early stage COPD is shown in Figure 8-3 below. The clinical plan, shown in Figure 8-3(a), treats the PTV (pink contour) without regard to the location of the functional lung tissue (orange contour). The functional plan, shown in Figure 8-3(b), treats the PTV with the same coverage while successfully avoiding most of the functional lung tissue.

An example of both the clinical and functional treatment plans for a patient with late stage COPD is shown in Figure 8-4. As seen in Figure 8-3, the clinical plan, shown in Figure 8-4(a), treats the PTV (pink contour) without regard to the location of the functional lung tissue (orange contour) while the functional plan, shown in Figure 8-4(b), treats the PTV with the same coverage while successfully avoiding the functional lung tissue. However, because this patient is in the later stages of COPD, the amount of functional tissue is significantly reduced as compared to the patient seen in Figure 8-3.

These figures indicate the functional lung tissue can be successfully avoided if taken into consideration in the treatment planning stage for both early and late stage COPD patients.

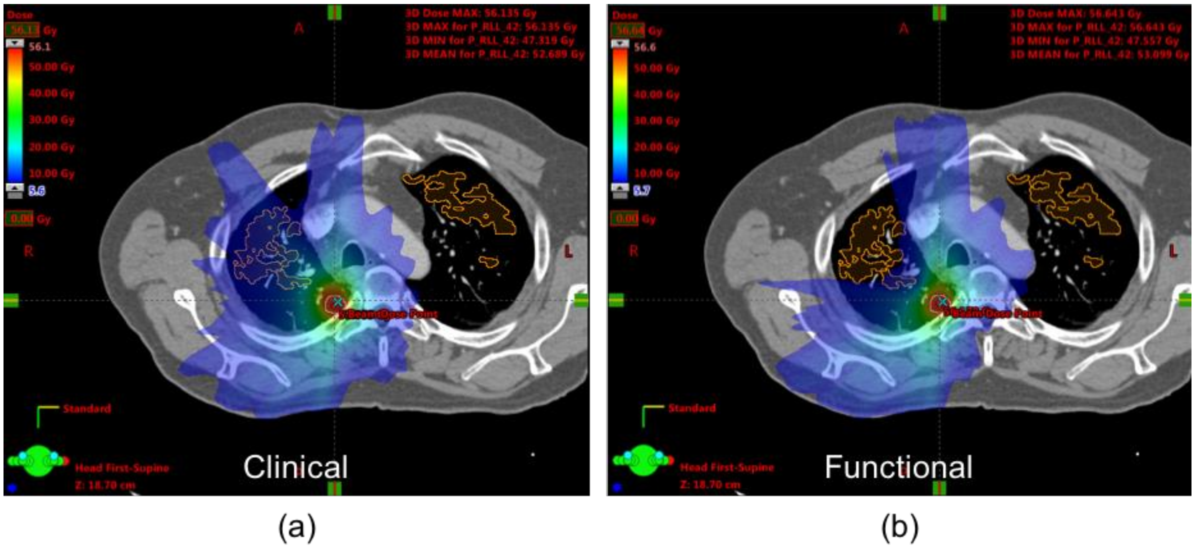

Figure 8-3: Dose wash comparison for clinical (a) and functional (b) treatment plans for early stage COPD patient

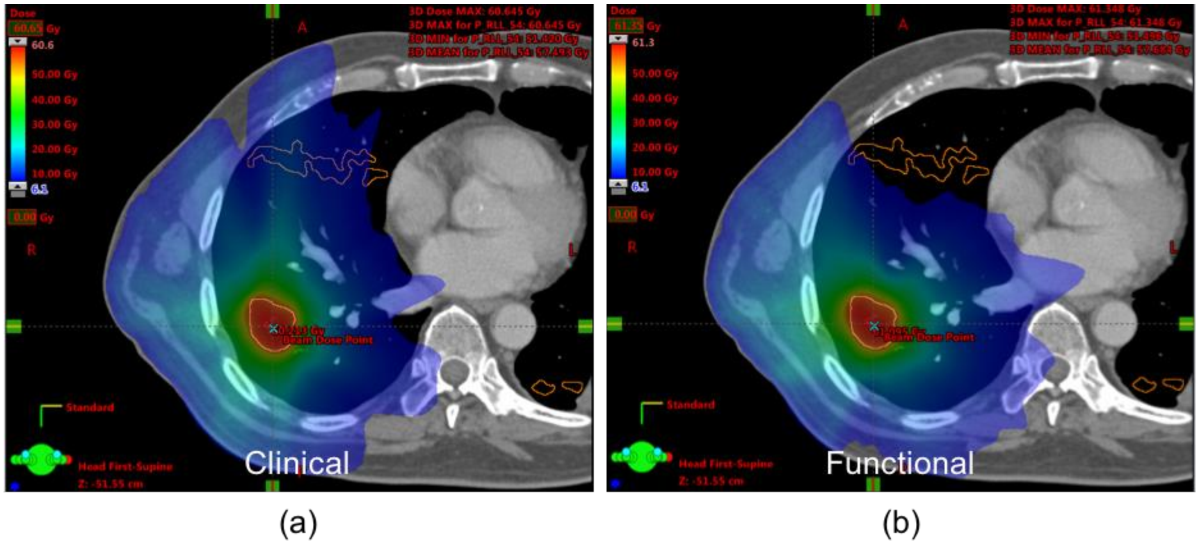

Figure 8-4: Dose wash comparison for clinical (a) and functional (b) treatment plans for late stage COPD patient

8.3.3.2 Plan evaluation. Both the clinical and functional avoidance plans were evaluated according to the criteria mentioned in §8.2.4.2 above. First, DVH's were looked at as a comparison for the total lung and functional lung for the clinical and functional plans. Figure 8-5 shows the DVH's for an early stage and a late stage COPD patient.

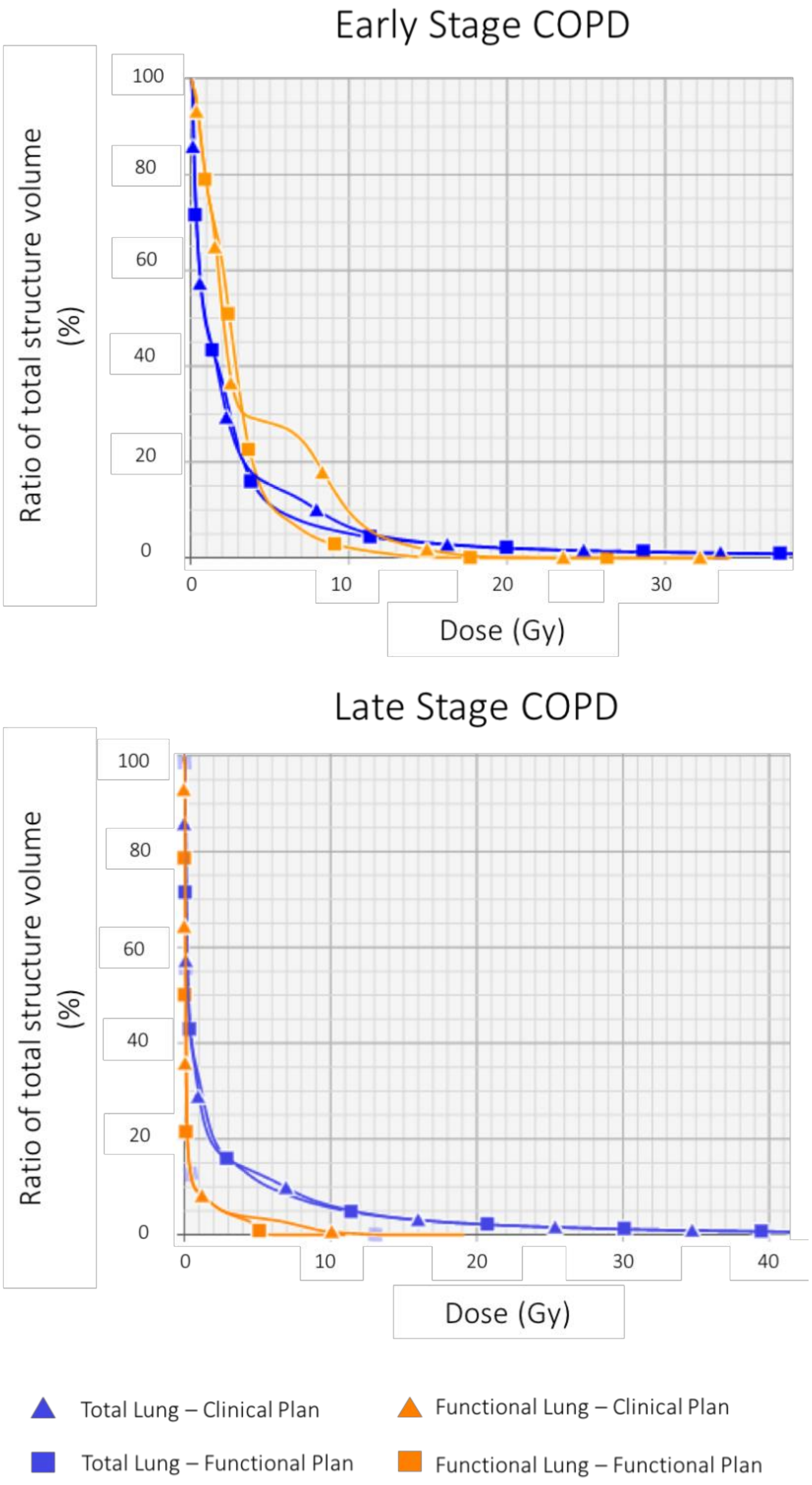

Figure 8-5: DVH comparison between clinical and functional plans for early stage COPD and late stage COPD patient. The total lung is represented in blue, functional lung in orange. The clinical plan is represented by triangular markers, while the functional plan is represented with squares.

For the early stage patient, it can be seen that while the total lung is slightly spared in the functional plan as compared to the clinical plan, the functional lung is spared considerably. For the late stage COPD patient, there is only slight sparing of both the functional and total lung tissue. It should be noted that the ITV and PTV coverage was very similar between the two plans. This illustrates that functional avoidance planning may not make as much of a difference for late stage COPD patients – however functional avoidance plans for late stage patients are still feasible and produce quality, if less substantial, improvements.

Dose volume and dose function metrics for both clinical and functional plans are shown in Table 8-4 for all patients. The metrics were grouped by COPD stage so that clinical and functional metrics can be easily compared. It can be seen that, in general, both dose volume and dose function metrics improved in the functional avoidance plans, regardless of patient disease stage. Dose function metrics improved more significantly as compared to dose volume metrics.

Table 8-4: Dose volume and dose function metrics for both clinical and functional plans for all patients

Patient Plan	**V_{20} (%)**	**V_{10} (%)**	**V_5 (%)**	**MLD (Gy)**	**fV_{20} (%)**	**fV_{10} (%)**	**fV_5 (%)**	**fMLD (Gy)**
1 Clinical	6.79	16.89	24.01	5.19	1.21	2.48	4.02	1.27
1 Functional	6.25	16.44	23.96	5.05	0.31	2.17	3.78	1.13
2 Clinical	1.11	3.36	8.21	1.63	1.71	6.64	15.19	2.54
2 Functional	0.79	2.81	7.24	1.52	1.17	5.43	13.18	2.35
3 Clinical	5.36	12.77	18.11	4.04	0.52	0.93	1.47	0.71
3 Functional	5.42	12.59	17.92	4.03	0.49	0.93	1.49	0.69
4 Clinical	2.22	6.04	12.88	2.29	0.00	0.58	3.52	0.70
4 Functional	2.22	5.62	11.23	2.26	0.00	0.00	1.16	0.52
5 Clinical	2.01	6.61	15.31	2.95	0.11	9.83	28.11	3.87
5 Functional	2.07	5.09	11.06	2.71	0.00	2.08	11.12	2.84
6 Clinical	3.90	10.76	17.24	3.63	5.03	26.23	38.37	6.43
6 Functional	3.81	10.27	17.41	3.60	2.66	13.91	27.97	4.66
7 Clinical	4.48	11.91	23.93	9.69	2.33	12.13	30.38	6.99
7 Functional	4.67	11.39	22.40	9.64	1.78	10.70	25.00	6.42

Table 8-5: Plan quality metrics for both clinical and functional plans for all patients

Patient Plan	PTV Dose Homogeneity	Mean Dose to PTV	Conformity Index
1 Clinical	2.91	1.11	1.03
1 Functional	3.24	1.11	1.00
2 Clinical	1.27	1.07	1.00
2 Functional	1.40	1.09	1.00
3 Clinical	1.29	1.07	0.98
3 Functional	1.30	1.06	0.97
4 Clinical	1.18	1.06	1.00
4 Functional	1.19	1.07	1.00
5 Clinical	1.19	1.05	0.98
5 Functional	1.19	1.05	0.98
6 Clinical	1.30	1.07	0.99
6 Functional	1.30	1.06	1.01
7 Clinical	1.31	1.08	0.99
7 Functional	1.52	1.08	1.00

Plan quality was evaluated by looking at maximum OAR dose, PTV dose homogeneity, normalized mean dose to PTV, and conformity index. Maximum OAR dose did not exceed clinical limits for both clinical and functional plans of all patients. Furthermore, maximum OAR dose, while increased slightly in some functional sparing cases, was not significantly different between clinical and functional sparing plans. Table 8-5 lists the dose homogeneity, normalized mean dose to PTV, and conformity index results for both clinical and functional plans for all patients. It can be seen that all three metrics did not change significantly between clinical and functional plans, indicating that plan quality was preserved even in functional avoidance situations.

8.4 Discussion

Elasticity information derived from 4DCT was used retrospectively to create contours of functional lung tissue for 7 lung SBRT patients with various stages of COPD. In reviewing the clinical treatment plans, it was seen that significant dose accumulation occurred in functional lung regions, especially for early stage patients. This indicated the potential for dosimetric sparing of functional lung tissue.

In our study, clinical plans were recreated for each patient, along with functional avoidance treatment plans. Functional lung avoidance was achieved by creating clinically acceptable SBRT plans that met all OAR constraints and an additional functional avoidance constraint while preserving target dose coverage, homogeneity and conformity. Both functional and total lung dosimetry decreased when the functional lung tissue was taken into consideration as compared to the general clinical plans.

Functional avoidance SBRT plans were created for all patients with both early and late stage COPD. Functional avoidance plans were more effective for early stage COPD patients, as more functional tissue was available for sparing. However, functional lung avoidance was still achieved for late stage COPD patients. Because late stage patients have very little functional tissue, it might be clinically beneficial to spare as much as possible in order to preserve quality of life. While future prospective studies will be necessary to assess this conclusion, we believe functional lung avoidance will be useful for all lung SBRT patients, regardless of COPD status.

We foresee three possible limitations to this study. First, the patient population utilized in this retrospective study was quite small, limiting the statistical significance of the results. Future work will need to retrospectively expand the data size before moving towards prospective studies. Secondly, while tissue elasticity derived from 4DCT has been correlated to function, it has not been associated to more widely utilized functional imaging methods. Furthermore, the elasticity thresholding used to stratify the functional tissue also needs to be validated with more established methodologies. Finally, although lung function can be reduced irreversibly by radiation therapy, the tumor can also be responsible for reduced lung function. A potential limitation is that lung volumes that may have received functionally-modified, (perhaps slightly amplified) dose may regain function after treatment. Our results do indicate that using functioanl avoidance techniques for SBRT, both the overall lung dose and the functional lung dose can be reduced. Prospective clinical trials will be necessary to determine whether treatment results, such as survival and complications, are improved using functional avoidance treatment planning.

In conclusion, functional contours were derived from 4DCT-based elasticity estimation for 7 lung SBRT patients. It was determined that the delivered plans resulted in significant dose to functional lung tissue for early stage COPD patients. A retrospective study was performed that re-planned the clinical plans for each patient. Functional avoidance plans using the elasticity-guided functional contours were also developed that had similar target coverage, met the normal tissue constraints, and resulted in less dose to functional lung tissue. Based on these results, with the knowledge of lung tissue elasticity and function, it is possible to develop functional tissue sparing SBRT plans that could result in improved patient quality of life after radiotherapy treatment.

CHAPTER 9: CONCLUSIONS

Summary of Work

The projects discussed in this dissertation present solutions for obtaining functional information using images and deformation information acquired within the radiotherapy workflow for breast, lung, and liver anatomies. Algorithms were developed to accurately estimate elasticity information from gravity-induced and breathing-induced deformation seen with CT image pairs and 4DMR. For the lung, the elasticity information estimated in these projects was successfully related to lung function and used to develop functional avoidance lung radiotherapy treatment plans. These works ultimately provide a therapeutic tool that can be used to reduce functional tissue toxicity for the lung, liver, and breast anatomies.

Chapter 2 describes the development of a GPU-based inverse elasticity estimation algorithm for gravity-induced breast deformations between supine and prone postures. The inverse analysis consisted of a gradient-based binary search optimization scheme coupled with a fast-simulated annealing algorithm that updated the spatial elasticity distribution until convergence occurred. This algorithm was systematically investigated using virtual breast phantoms. Our analysis showed a 97 ± 4 % accuracy in the elasticity estimation of virtual homogenous breast tissue with embedded tumor.

In chapter 3, the elasticity estimation algorithm was refactored to account for the breathing-induced motion of the lung anatomy using virtual lung phantoms and simulated breathing deformation values. A novel locally heterogeneous convergence magnification technique was applied in order to gain elasticity information from the subtle deformation of the interior voxels of the lungs. Our analysis showed an average of 92 ± 5% of voxels converged within 1 kPa of the ground-truth elasticity and within 0.5 mm of ground-truth deformation.

In chapter 4, the lung elasticity estimation algorithm was extended to 15 patient 5DCT datasets. Patient-specific ground-truth deformation values between end-inhalation and end-exhalation breathing were obtained for each voxel of lung tissue using optical flow deformable image registration. Our analysis showed that an average of 90 ± 5% of voxels converged within a prescribed error metric of 10% of maximum deformation. A validation dataset of mid-exhalation breathing phase deformation data converged with 87 ± 11% of voxels within 1 mm of ground-truth deformation. These results indicate the quantitative accuracy of the elasticity estimation process.

Chapter 5 determined the feasibility of performing elastography using lower dose scans. For these purposes, simulated tube current-time products of 30 mAs, 25 mAs, and 20 mAs were generated for 8 patients. The elastography results of the lower mAs scans were not significantly different than the original results, illustrating that mAs (and thus imaging dose) can be reduced by as much as 50% while still producing CT images that are useful for elastography purposes.

In Chapter 6, the elasticity estimated algorithm was extended to 4DMR scans of the liver. This was a natural extension, as the liver motion stems from the breathing-induced motion of the diaphragm and elastography of the liver anatomy using (Viewray) 0.35 T MR Scanners has not yet been developed and validated. The 95 ± 8% convergence of the elastography technique presented here indicates the potential for integrating liver elastography directly within the radiotherapy workflow.

While the methodology provided accurate, organ-specific elasticity distribution estimations for the lung and liver anatomies, the connection between elasticity and organ function remained abstract. Chapter 7 related the pulmonary elasticity distribution to the function of the lung tissue for 13 patients with COPD diagnoses. A preliminary imaging biomarker for COPD was assessed in comparison to the densitometry metric RA_{950} and performed favorably.

In chapter 8, the elasticity distributions were used to identify functional regions of parenchymal tissue for 7 lung SBRT patients. Clinically-delivered plans resulted in significant dose to functional lung tissue for early stage COPD patients. Functional avoidance plans were developed using the elasticity-guided functional tissue contours that met normal tissue and target coverage constraints similarly to re-planned clinical treatment plans, while delivering less dose to functional lung tissue. These results suggest that, with the knowledge of lung tissue elasticity, it is possible to develop functional tissue sparing SBRT that could result in a decrease in lung toxicity after radiotherapy treatment.

While the methodologies presented here have been fully validated using simulations and retrospective patient studies, a few obstacles remain on the road to clinical implementation. Future directions that could overcome the obstacles for each of the projects are presented in the next section.

Future Directions

In order to expand the elasticity estimation methodology to the radiotherapy clinic, three major overarching challenges need to be addressed for the lung, liver, and breast anatomies. First, due to the large breast tissue deformation between the prone and supine position and the complex mechanics of diseased lung and liver tissue, the linear elastic constitutive laws utilized in this study may need to be extended to the hyperelastic regime. The impact of different strain rates on elasticity assumptions and estimations will also need to be investigated. The current imaging protocols may need to be modified in order to better describe hyperelastic tissue behavior; for example, the incorporation of additional CT scans, fast helical CT scans, or MR elastography techniques could provide more useful deformation information. Secondly, due to the time constraints that are commonplace in clinical radiotherapy practice, the methodology will need to be implemented in a multi-GPU framework. GPU clusters could be employed to enable the estimation process to be completed within acceptable computation times. The implementation of the methods presented here on a GPU cluster will continue to ensure that the elasticity information can be available within a reasonable radiotherapy timeline. And finally, the works presented here focused on developing and implementing the elastography methodology on pristine datasets – i.e. simulations and 5DCT datasets. The influence of common radiotherapy imaging artifacts, such as those seen in 4DCT, needs to be more fully investigated.

Specifically for the breast anatomy, a deformable image registration technique needs to be developed that provides accurate ground-truth data and a one-to-one correspondence between breast tissue in the prone and supine positions. For the liver, MRE data should be obtained as a validation dataset for 4DMR liver elastography techniques. More patient data needs to be collected for further studying the elastography process. Longitudinal studies could be utilized to investigate elasticity changes seen during radiation-induced liver injury during SBRT. For the lung, future work should investigate using deformation data from multiple breathing stages to estimate elasticity distributions more quickly. *In vivo* tissue experiments and US/MR elastography techniques could be investigated for further verification and validation purposes.

To integrate the functional elasticity information into the treatment planning workflow, a retrospective study with a larger patient population will need to be conducted. The elastic threshold of functional lung tissue needs to be determined via more thorough numerical analyses. A clinical protocol should be developed that focuses on explicitly validating lung regions affected by pulmonary disease by a pulmonary radiologist. More scan time points will need to be obtained, and changes in elasticity over time need to be correlated with radiotherapy and disease progression. Elastography and ventilation imaging methods could be integrated to more fully describe lung function. Eventually, elastography guided functional lung planning could be integrated into an adaptive radiotherapy workflow to facilitate the sparing of functional lung tissue.

When expanding the lung elastography methodology beyond the radiotherapy clinic, total lung capacity and functional residual capacity scans can be acquired for COPD patients to further evaluate the diagnostic potential. The resultant elasticity distributions gained from our methodology could be used to determine degree of hyperinflation and air trapping in COPD patients, to longitudinally assess the degree and progression of disease in COPD patient, and to differentiate between tissue affected with bronchitis and emphysema, leading to patient-specific treatment options.

APPENDIX A

Noisy data injection

The 4DCT scan consisted of a series of individual 3D CT scans at different time points. Noise was injected at each time point independently and on each slice independently, neglecting the cone angle of the system and assuming it is similar to a fan-beam geometry.

Each slice was forward projected to estimate the attenuation of each ray, and we included the effect of a bowtie filter that was added following the attenuation profile described in [182], which was for a different system. We assumed that the scanner used a rebin-to-parallel reconstruction scheme to preserve noise uniformity and hence sampled rays in a parallel beam fashion.

The number of photons incident on the detector was calculated by estimating that 1.8 * 106 photons/mm^2-mAs arrived at the detector in the absence of attenuation for a typical spectrum at 120 kVp [183]. The number of photons was then multiplied by an efficiency factor E that incorporates effects such as geometric efficiency, added noise from scatter or Swank factor. E was selected by comparison to experimental measurements, explained later. This noise-addition sinogram was then filtered by a smoothing function $s(x)$ to match the noise power spectrum. This noise-addition sinogram was then reconstructed and added to the original image to synthesize the reduced dose CT scan. An important limitation of this study is that the DICOM files record only an average mAs, whereas commercial scanners today used tube current modulation. Hence, our simulations implicitly assume constant tube current. In order to provide a conservative estimate of possible dose reduction, we assumed that the original scans were noiseless.

The efficiency factor E and smoothing function $s(x)$ were tuned to reconstructions of a water cylinder scanned at the same protocol as the clinical series. The water cylinder image was binarized (thresholded to either -1000 or 0 HU) to create a simulated noiseless water cylinder, and noise was injected into the binarized water cylinder to simulate the noise in the experimental measurements. The 1D noise power spectrum was calculated for comparison. The calculation of the noise power spectrum (NPS) has been described in greater detail elsewhere [184, 185] but briefly, 7 adjacent slices were averaged to alleviate through-plane correlations, a series of square ROIs with side length 31 mm and each positioned 30 mm from the center of the water cylinder were defined, and their Fourier transforms were taken after mean subtraction to create the NPS. These NPS measurements were averaged and binned in the radial direction to produce 1D NPS. To match the simulated NPS with experimental NPS, we selected an efficiency factor of E = 59% and a Gaussian smoothing filter with standard deviation of 0.43 channels.

Figure A1 shows the experimental versus simulated noise in a water cylinder, and figure A2 shows the estimated noise power spectra. Agreement of the noise power spectra is moderate at low frequencies, presumably due to the presence of structured noise. The spatial distribution of the noise as seen in figure A1 is somewhat different, possibly because we used a generic bowtie filter profile that may not match this scanner.

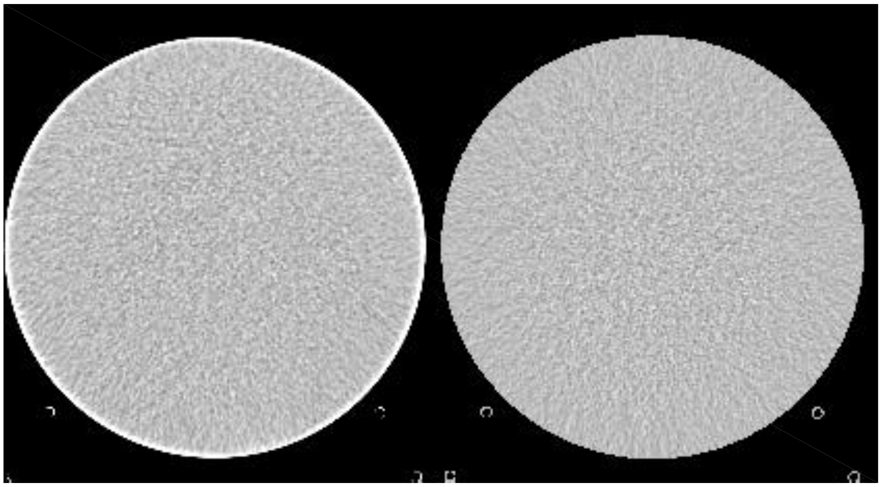

Figure A1: Left) Experimental reconstruction of water cylinder. [27] Simulated injection of noise. Average of 7 slices. WW = 100 HU.

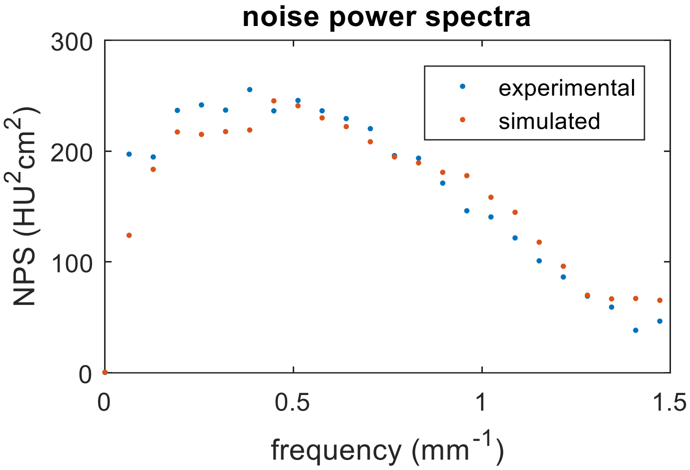

Figure A2: Comparison of noise power spectra from simulated and experimental data.

REFERENCES

1. Moding, E.J., M.B. Kastan, and D.G. Kirsch, *Strategies for optimizing the response of cancer and normal tissues to radiation.* Nat Rev Drug Discov, 2013. **12**(7): p. 526-42.
2. Niemierko, A. and M. Goitein, *Modeling of Normal Tissue-Response to Radiation - the Critical Volume Model.* International Journal of Radiation Oncology Biology Physics, 1993. **25**(1): p. 135-145.
3. Partridge, M., et al., *Imaging of normal lung, liver and parotid gland function for radiotherapy.* Acta Oncol, 2010. **49**(7): p. 997-1011.
4. Vinogradskiy, Y., et al., *Use of 4-Dimensional Computed Tomography-Based Ventilation Imaging to Correlate Lung Dose and Function With Clinical Outcomes.* International Journal of Radiation Oncology Biology Physics, 2013. **86**(2): p. 366-371.
5. Chae, E.J., et al., *Xenon ventilation CT with a dual-energy technique of dual-source CT: initial experience.* Radiology, 2008. **248**(2): p. 615-24.
6. Farr, K.P., et al., *Inclusion of functional information from perfusion SPECT improves predictive value of dose-volume parameters in lung toxicity outcome after radiotherapy for non-small cell lung cancer: A prospective study.* Radiother Oncol, 2015. **117**(1): p. 9-16.
7. Yamamoto, T., et al., *Impact of four-dimensional computed tomography pulmonary ventilation imaging-based functional avoidance for lung cancer radiotherapy.* Int J Radiat Oncol Biol Phys, 2011. **79**(1): p. 279-88.
8. Yamamoto, T., et al., *Pulmonary ventilation imaging based on 4-dimensional computed tomography: comparison with pulmonary function tests and SPECT ventilation images.* Int J Radiat Oncol Biol Phys, 2014. **90**(2): p. 414-22.
9. Bernardin, L., E.A. O'Flynn, and N.M. Desouza, *Functional imaging biomarkers for assessing response to treatment in liver and lung metastases.* Cancer Imaging, 2013. **13**(4): p. 482-94.
10. Lin, W., et al., *Respiratory motion-compensated radial dynamic contrast-enhanced (DCE)-MRI of chest and abdominal lesions.* Magn Reson Med, 2008. **60**(5): p. 1135-46.
11. Fang, M., et al., *Collagen as a double-edged sword in tumor progression.* Tumour Biol, 2014. **35**(4): p. 2871-82.
12. Dvorak, H.F., J. Flier, and H. Frank, *Tumors - Wounds That Do Not Heal - Similarities between Tumor Stroma Generation and Wound-Healing.* New England Journal of Medicine, 1986. **315**(26): p. 1650-1659.
13. Zhang, Y., et al., *Characteristics of normal stromal components and their correlation with cancer occurrence in human prostate.* Oncol Rep, 2003. **10**(1): p. 207-11.
14. Riching, K.M., et al., *3D collagen alignment limits protrusions to enhance breast cancer cell persistence.* Biophys J, 2014. **107**(11): p. 2546-58.
15. Tuxhorn, J.A., et al., *Reactive stroma in human prostate cancer: induction of myofibroblast phenotype and extracellular matrix remodeling.* Clin Cancer Res, 2002. **8**(9): p. 2912-23.
16. Pellegrini, M., et al., *Effects of superimposed tissue weight on regional compliance of injured lungs.* Respir Physiol Neurobiol, 2016. **228**: p. 16-24.

17. Suki, B. and J.H. Bates, *Extracellular matrix mechanics in lung parenchymal diseases.* Respir Physiol Neurobiol, 2008. **163**(1-3): p. 33-43.
18. Xu, Y., et al., *Strain elastography imaging for early detection and prediction of tumor response to concurrent chemo-radiotherapy in locally advanced cervical cancer: feasibility study.* BMC Cancer, 2017. **17**(1): p. 427.
19. Risholm, P., et al., *Probabilistic Elastography: Estimating Lung Elasticity.* Information Processing in Medical Imaging, 2011. **6801**: p. 699-710.
20. Doyley, M.M., *Model-based elastography: a survey of approaches to the inverse elasticity problem.* Phys Med Biol, 2012. **57**(3): p. R35-73.
21. Krouskop, T.A., et al., *Elastic moduli of breast and prostate tissues under compression.* Ultrason Imaging, 1998. **20**(4): p. 260-74.
22. Rivaz, H., et al., *Tracked regularized ultrasound elastography for targeting breast radiotherapy.* Med Image Comput Comput Assist Interv, 2009. **12**(Pt 1): p. 507-15.
23. Evans, A., et al., *Quantitative shear wave ultrasound elastography: initial experience in solid breast masses.* Breast Cancer Res, 2010. **12**(6): p. R104.
24. Wang, Z.L., et al., *Relationship between elasticity and collagen fiber content in breast disease: a preliminary report.* Ultrasonics, 2015. **57**: p. 44-9.
25. Garra, B.S., et al., *Elastography of breast lesions: initial clinical results.* Radiology, 1997. **202**(1): p. 79-86.
26. Goddi, A., M. Bonardi, and S. Alessi, *Breast elastography: A literature review.* J Ultrasound, 2012. **15**(3): p. 192-8.
27. Rivaz, H., et al., *Tracked Regularized Ultrasound Elastography for Targeting Breast Radiotherapy.* Medical Image Computing and Computer-Assisted Intervention - Miccai 2009, Pt I, Proceedings, 2009. **5761**: p. 507-515.
28. Sperandeo, M., et al., *Lung transthoracic ultrasound elastography imaging and guided biopsies of subpleural cancer: a preliminary report.* Acta Radiol, 2015. **56**(7): p. 798-805.
29. Negahdar, M., et al., *Noninvasive pulmonary nodule elastometry by CT and deformable image registration.* Radiother Oncol, 2015. **115**(1): p. 35-40.
30. Mariappan, Y.K., et al., *MR Elastography of Human Lung Parenchyma: Technical Development, Theoretical Modeling and In Vivo Validation.* Journal of Magnetic Resonance Imaging, 2011. **33**(6): p. 1351-1361.
31. Crecea, V., A. Ahmad, and S.A. Boppart, *Magnetomotive optical coherence elastography for microrheology of biological tissues.* Journal of Biomedical Optics, 2013. **18**(12).
32. Titz, B. and R. Jeraj, *An imaging-based tumour growth and treatment response model: investigating the effect of tumour oxygenation on radiation therapy response.* Phys Med Biol, 2008. **53**(17): p. 4471-88.
33. South, C.P., M. Partridge, and P.M. Evans, *A theoretical framework for prescribing radiotherapy dose distributions using patient-specific biological information.* Med Phys, 2008. **35**(10): p. 4599-611.
34. O'Shea, T., et al., *Review of ultrasound image guidance in external beam radiotherapy part II: intra-fraction motion management and novel applications.* Phys Med Biol, 2016. **61**(8): p. R90-137.
35. McGee, K.P., R.D. Hubmayr, and R.L. Ehman, *MR elastography of the lung with hyperpolarized 3He.* Magn Reson Med, 2008. **59**(1): p. 14-8.
36. Kurzrock, R. and M. Markman, *Targeted cancer therapy*. Current clinical oncology. 2008, Totowa, N.J.: Humana Press. xii, 445 p.

37. Paparo, F., et al., *Real-time elastography in the assessment of liver fibrosis: a review of qualitative and semi-quantitative methods for elastogram analysis.* Ultrasound Med Biol, 2014. **40**(9): p. 1923-33.
38. Li, C., et al., *Diagnostic Accuracy of Real-Time Shear Wave Elastography for Staging of Liver Fibrosis: A Meta-Analysis.* Med Sci Monit, 2016. **22**: p. 1349-59.
39. Ichikawa, S., et al., *Magnetic resonance elastography for prediction of radiation-induced liver disease after stereotactic body radiation therapy.* Hepatology, 2017. **66**(2): p. 664-665.
40. Yin, M., et al., *Hepatic MR Elastography: Clinical Performance in a Series of 1377 Consecutive Examinations.* Radiology, 2016. **278**(1): p. 114-24.
41. McGarry, M.D., et al., *Multiresolution MR elastography using nonlinear inversion.* Med Phys, 2012. **39**(10): p. 6388-96.
42. Honarvar, M., et al., *Sparsity regularization in dynamic elastography.* Phys Med Biol, 2012. **57**(19): p. 5909-27.
43. Wu, G., J. Lian, and D. Shen, *Improving image-guided radiation therapy of lung cancer by reconstructing 4D-CT from a single free-breathing 3D-CT on the treatment day.* Med Phys, 2012. **39**(12): p. 7694-709.
44. Venkatesh, S.K., M. Yin, and R.L. Ehman, *Magnetic resonance elastography of liver: technique, analysis, and clinical applications.* J Magn Reson Imaging, 2013. **37**(3): p. 544-55.
45. Fatunase, T., et al., *Assessment of the residual error in soft tissue setup in patients undergoing partial breast irradiation: results of a prospective study using cone-beam computed tomography.* Int J Radiat Oncol Biol Phys, 2008. **70**(4): p. 1025-34.
46. Kirby, A.M., et al., *Prone versus supine positioning for whole and partial-breast radiotherapy: a comparison of non-target tissue dosimetry.* Radiother Oncol, 2010. **96**(2): p. 178-84.
47. Lawrence, T.S., et al., *The Use of 3-D-Dose Volume Analysis to Predict Radiation Hepatitis.* International Journal of Radiation Oncology Biology Physics, 1992. **23**(4): p. 781-788.
48. Doyley, M.M., et al., *Comparative evaluation of strain-based and model-based modulus elastography.* Ultrasound Med Biol, 2005. **31**(6): p. 787-802.
49. Doyley, M.M., P.M. Meaney, and J.C. Bamber, *Evaluation of an iterative reconstruction method for quantitative elastography.* Phys Med Biol, 2000. **45**(6): p. 1521-40.
50. Suki, B., D. Stamenovic, and R. Hubmayr, *Lung parenchymal mechanics.* Compr Physiol, 2011. **1**(3): p. 1317-51.
51. Liu, F., et al., *Feedback amplification of fibrosis through matrix stiffening and COX-2 suppression.* J Cell Biol, 2010. **190**(4): p. 693-706.
52. Neylon, J., et al., *A GPU based high-resolution multilevel biomechanical head and neck model for validating deformable image registration.* Med Phys, 2015. **42**(1): p. 232-43.
53. Timmerman, R., et al., *Stereotactic body radiation therapy for inoperable early stage lung cancer.* JAMA, 2010. **303**(11): p. 1070-6.
54. Association, A.L. *Lung Health and Diseases*. 2016 [cited 2016 03-23]; Available from: http://www.lung.org/lung-health-and-diseases.
55. Westover, K.D., et al., *Precision Hypofractionated Radiation Therapy in Poor Performing Patients With Non-Small Cell Lung Cancer: Phase 1 Dose Escalation Trial.* Int J Radiat Oncol Biol Phys, 2015. **93**(1): p. 72-81.

56. Chen, H., et al., *Quality of Life After Stereotactic Ablative Radiotherapy for Early-Stage Lung Cancer: A Systematic Review.* Clin Lung Cancer, 2015.
57. Kennedy, K.M., et al., *Quantitative micro-elastography: imaging of tissue elasticity using compression optical coherence elastography.* Sci Rep, 2015. **5**: p. 15538.
58. Lumb, A.B. and J.F. Nunn, *Nunn's applied respiratory physiology*. 6th ed. 2005, Edinburgh ; Philadelphia: Elsevier Butterworth Heinemann. xiii, 501 p.
59. Villard, P.F., et al., *Simulation of lung behaviour with finite elements : Influence of bio-mechanical parameters.* Third International Conference on Medical Information Visualisation - BioMedical Visualisation (MediVis 2005), Proceedings, 2005: p. 9-14.
60. Hasse, K., et al., *Systematic feasibility analysis of a quantitative elasticity estimation for breast anatomy using supine/prone patient postures.* Med Phys, 2016. **43**(3): p. 1299-1311.
61. Santhanam, A.P., et al., *Modeling real-time 3-d lung deformations for medical visualization.* IEEE Trans Inf Technol Biomed, 2008. **12**(2): p. 257-70.
62. Al-Mayah, A., J. Moseley, and K.K. Brock, *Contact surface and material nonlinearity modeling of human lungs.* Phys Med Biol, 2008. **53**(1): p. 305-17.
63. Liu, F. and D.J. Tschumperlin, *Micro-mechanical characterization of lung tissue using atomic force microscopy.* J Vis Exp, 2011(54).
64. Karami, E.G., S. ; Lee, T; Samini, A, *A biomechanical approach for in vivo lung tumor motion prediction during external beam radiation therapy.* SPIE Proceedings, 2015. **9415**(Medical Imaging 2015: Image-Guided Procedures, Robotic Interventions, and Modeling).
65. Diciotti, S., et al., *Development of digital phantoms based on a finite element model to simulate low-attenuation areas in CT imaging for pulmonary emphysema quantification.* Int J Comput Assist Radiol Surg, 2016.
66. Ilegbusi, O.J., B. Seyfi, and R. Salvin, *Patient-specific model of lung deformation using spatially dependent constitutive parameters.* Mathematical and Computer Modelling of Dynamical Systems, 2014. **20**(6): p. 546-556.
67. Karami, E., et al., *A Biomechanical approach for in vivo Lung Tumor Motion Prediction during External Beam Radiation Therapy.* Medical Imaging 2015: Image-Guided Procedures, Robotic Interventions, and Modeling, 2015. **9415**.
68. Werner, R., et al., *Patient-specific finite element modeling of respiratory lung motion using 4D CT image data.* Med Phys, 2009. **36**(5): p. 1500-11.
69. Werner, R., et al., *Modeling respiratory lung motion - a biophysical approach using finite element methods.* Medical Imaging 2008: Physiology, Function, and Structure from Medical Images, 2008. **6916**.
70. Kallel, F. and M. Bertrand, *Tissue elasticity reconstruction using linear perturbation method.* IEEE Trans Med Imaging, 1996. **15**(3): p. 299-313.
71. Fu, D., et al., *Non-invasive quantitative reconstruction of tissue elasticity using an iterative forward approach.* Phys Med Biol, 2000. **45**(6): p. 1495-509.
72. Booth, A.J., et al., *Acellular normal and fibrotic human lung matrices as a culture system for in vitro investigation.* Am J Respir Crit Care Med, 2012. **186**(9): p. 866-76.
73. Schnur, D.S. and N. Zabaras, *An Inverse Method for Determining Elastic-Material Properties and a Material Interface.* International Journal for Numerical Methods in Engineering, 1992. **33**(10): p. 2039-2057.

74. Goenezen, S., P. Barbone, and A.A. Oberai, *Solution of the nonlinear elasticity imaging inverse problem: The incompressible case.* Computer Methods in Applied Mechanics and Engineering, 2011. **200**(13-16): p. 1406-1420.
75. Miga, M.I., *A new approach to elastography using mutual information and finite elements.* Phys Med Biol, 2003. **48**(4): p. 467-80.
76. Bonnet, M. and A. Constantinescu, *Inverse problems in elasticity.* Inverse Problems, 2005. **21**(2): p. R1-R50.
77. Ma, J.A., I. Temizer, and P. Wriggers, *Random homogenization analysis in linear elasticity based on analytical bounds and estimates.* International Journal of Solids and Structures, 2011. **48**(2): p. 280-291.
78. Guchhait S, B.B., *Anisotropic linear elastic parameter estimation using error in the constitutive equation functional.* Proc. R. Soc., 2016. **A 472**(20160213).
79. Santhanam, A.P., et al., *An inverse hyper-spherical harmonics-based formulation for reconstructing 3D volumetric lung deformations.* Comptes Rendus Mecanique, 2010. **338**(7-8): p. 461-473.
80. Hinz, B., *Mechanical aspects of lung fibrosis: a spotlight on the myofibroblast.* Proc Am Thorac Soc, 2012. **9**(3): p. 137-47.
81. Latifi, K., et al., *Effects of quantum noise in 4D-CT on deformable image registration and derived ventilation data.* Phys Med Biol, 2013. **58**(21): p. 7661-72.
82. Durham, A.L. and I.M. Adcock, *The relationship between COPD and lung cancer.* Lung Cancer, 2015. **90**(2): p. 121-7.
83. de-Torres, J.P., et al., *Lung cancer in patients with chronic obstructive pulmonary disease. Development and validation of the COPD Lung Cancer Screening Score.* Am J Respir Crit Care Med, 2015. **191**(3): p. 285-91.
84. Ebihara, T., et al., *Changes in extracellular matrix and tissue viscoelasticity in bleomycin-induced lung fibrosis. Temporal aspects.* Am J Respir Crit Care Med, 2000. **162**(4 Pt 1): p. 1569-76.
85. Shifren, A. and R.P. Mecham, *The stumbling block in lung repair of emphysema: elastic fiber assembly.* Proc Am Thorac Soc, 2006. **3**(5): p. 428-33.
86. Nishio, M., et al., *Emphysema quantification by combining percentage and size distribution of low-attenuation lung regions.* AJR Am J Roentgenol, 2014. **202**(5): p. W453-8.
87. MacMahon, H., et al., *Guidelines for management of small pulmonary nodules detected on CT scans: a statement from the Fleischner Society.* Radiology, 2005. **237**(2): p. 395-400.
88. Faffe, D.S. and W.A. Zin, *Lung parenchymal mechanics in health and disease.* Physiol Rev, 2009. **89**(3): p. 759-75.
89. Santhanam, A.P., F.G. Hamza-Lup, and J.P. Rolland, *Simulating 3-D lung dynamics using a programmable graphics processing unit.* IEEE Trans Inf Technol Biomed, 2007. **11**(5): p. 497-506.
90. Suki, B., et al., *Biomechanics of the lung parenchyma: critical roles of collagen and mechanical forces.* J Appl Physiol (1985), 2005. **98**(5): p. 1892-9.
91. Mikulski, M.A., et al., *Agreement between fixed-ratio and lower limit of normal spirometry interpretation protocols decreases with age: is there a need for a new GOLD standard?* J Occup Environ Med, 2013. **55**(7): p. 802-8.

92. Brown, R.H., *Registration-based metrics of lung function to describe COPD: the ultimate question of life, the universe, and everything.* Acad Radiol, 2013. **20**(5): p. 525-6.

93. Fredman, A.J., J.L. Frolik, and B.S. Garra, *Lung strain profiles using computed tomography elastography.* Conf Proc IEEE Eng Med Biol Soc, 2004. **2**: p. 1545-8.

94. Min, Y.G., et al., *4D-CT Lung registration using anatomy-based multi-level multi-resolution optical flow analysis and thin-plate splines.* International Journal of Computer Assisted Radiology and Surgery, 2014. **9**(5): p. 875-889.

95. Low, D.A., et al., *A novel CT acquisition and analysis technique for breathing motion modeling.* Phys Med Biol, 2013. **58**(11): p. L31-6.

96. Thomas, D., et al., *A novel fast helical 4D-CT acquisition technique to generate low-noise sorting artifact-free images at user-selected breathing phases.* Int J Radiat Oncol Biol Phys, 2014. **89**(1): p. 191-8.

97. Low, D.A., et al., *Novel breathing motion model for radiotherapy.* Int J Radiat Oncol Biol Phys, 2005. **63**(3): p. 921-9.

98. Ung, Y.C., et al., *Defining the appropriate PET intensity threshold and CT threshold for target delineation in early stage non-small cell lung cancer: A radiological and pathological correlation study.* International Journal of Radiation Oncology Biology Physics, 2008. **72**(1): p. S113-S113.

99. White, B.M., et al., *Accuracy of Routine Treatment Planning 4-Dimensional and Deep-Inspiration Breath-Hold Computed Tomography Delineation of the Left Anterior Descending Artery in Radiation Therapy.* International Journal of Radiation Oncology Biology Physics, 2015. **91**(4): p. 825-831.

100. Dou, T.H., et al., *Fast simulated annealing and adaptive Monte Carlo sampling based parameter optimization for dense optical-flow deformable image registration of 4DCT lung anatomy.* Medical Imaging 2016: Image-Guided Procedures, Robotic Interventions, and Modeling, 2016. **9786**.

101. Hasse, K., J. Neylon, and A.P. Santhanam, *Feasibility and Quantitative Analysis of a Biomechanical Model-guided Lung Elastography for Radiotherapy.* Biomedical Physics and Engineering Express, 2017. **3**(2): p. 025006.

102. Kemerink, G.J., et al., *On segmentation of lung parenchyma in quantitative computed tomography of the lung.* Med Phys, 1998. **25**(12): p. 2432-9.

103. Elaiyaraja, G. and N. Kumaratharan, *An enhanced algorithm for removal of noise in CT scan image and 3D abdomen color video sequence through trimmed based filter.* Biomedical Research-India, 2017. **28**(2): p. 512-518.

104. Qing, K., et al., *Rapid acquisition of helium-3 and proton three-dimensional image sets of the human lung in a single breath-hold using compressed sensing.* Magn Reson Med, 2015. **74**(4): p. 1110-5.

105. Bognar, G., *Image Quality Measurement for Low-Dose Human Lung CT Scans.* 2015 38th International Conference on Telecommunications and Signal Processing (Tsp), 2015: p. 587-591.

106. Wang, Z., et al., *Image quality assessment: from error visibility to structural similarity.* IEEE Trans Image Process, 2004. **13**(4): p. 600-12.

107. Zhao, F., Q.M. Huang, and W. Gao, *Image matching by normalized cross-correlation.* 2006 Ieee International Conference on Acoustics, Speech and Signal Processing, Vols 1-13, 2006: p. 1977-1980.

108. Avants, B.B., et al., *Symmetric diffeomorphic image registration with cross-correlation: Evaluating automated labeling of elderly and neurodegenerative brain.* Medical Image Analysis, 2008. **12**(1): p. 26-41.
109. Viola, P. and W.M. Wells, *Alignment by maximization of mutual information.* International Journal of Computer Vision, 1997. **24**(2): p. 137-154.
110. Modat, M., et al., *Diffeomorphic Demons using Normalised Mutual Information, Evaluation on Multi-Modal Brain MR Images.* Medical Imaging 2010: Image Processing, 2010. **7623**.
111. Foundation, P.S., *Python 2.7*. 2017: https://www.python.org/.
112. Papandrinopoulou, D., V. Tzouda, and G. Tsoukalas, *Lung compliance and chronic obstructive pulmonary disease.* Pulm Med, 2012. **2012**: p. 542769.
113. Yamamoto, T., et al., *The first patient treatment of computed tomography ventilation functional image-guided radiotherapy for lung cancer.* Radiother Oncol, 2016. **118**(2): p. 227-31.
114. Kida, S., et al., *CT ventilation functional image-based IMRT treatment plans are comparable to SPECT ventilation functional image-based plans.* Radiother Oncol, 2016. **118**(3): p. 521-7.
115. Kimura, T., et al., *Functional image-guided radiotherapy planning in respiratory-gated intensity-modulated radiotherapy for lung cancer patients with chronic obstructive pulmonary disease.* Int J Radiat Oncol Biol Phys, 2012. **82**(4): p. e663-70.
116. National Center for Chronic Disease Prevention and Health Promotion, D.o.P.H. *Chronic Obstructive Pulmonary Disease (COPD)*. 2017; Available from: https://www.cdc.gov/copd/index.html.
117. Ophir, J., et al., *Elastography: Imaging the elastic properties of soft tissues with ultrasound.* J Med Ultrason (2001), 2002. **29**(4): p. 155.
118. Hasse, K., et al., *Estimation and validation of patient-specific high-resolution lung elasticity derived from 4DCT.* Med Phys, 2017.
119. Thomas, D.H., et al., *Is there an ideal set of prospective scan acquisition phases for fast-helical based 4D-CT?* Physics in Medicine and Biology, 2016. **61**(23): p. N632-N641.
120. O'Connell, D., et al., *A prospective gating method to acquire a diverse set of free-breathing CT images for model-based 4DCT.* Phys Med Biol, 2018. **63**(4): p. 04NT03.
121. Mettler, F.A., Jr., et al., *Effective doses in radiology and diagnostic nuclear medicine: a catalog.* Radiology, 2008. **248**(1): p. 254-63.
122. Yin, Y., et al., *Quantitative CT In Spiromics: Lobar Evaluation Via Image Warping Of Tlc Masks Onto Rv Images.* American Journal of Respiratory and Critical Care Medicine, 2014. **189**.
123. Kubo, T., et al., *Radiation dose reduction in chest CT: a review.* AJR Am J Roentgenol, 2008. **190**(2): p. 335-43.
124. Li, X., et al., *Pediatric MDCT: towards assessing the diagnostic influence of dose reduction on the detection of small lung nodules.* Acad Radiol, 2009. **16**(7): p. 872-80.
125. Mayo, J.R., et al., *Simulated dose reduction in conventional chest CT: validation study.* Radiology, 1997. **202**(2): p. 453-7.
126. Jun, B.G., et al., *Clinical significance of radiation-induced liver disease after stereotactic body radiation therapy for hepatocellular carcinoma.* Korean J Intern Med, 2017.

127. Jung, J., et al., *Radiation-induced liver disease after stereotactic body radiotherapy for small hepatocellular carcinoma: clinical and dose-volumetric parameters.* Radiat Oncol, 2013. **8**: p. 249.
128. Affo, S., L.X. Yu, and R.F. Schwabe, *The Role of Cancer-Associated Fibroblasts and Fibrosis in Liver Cancer.* Annu Rev Pathol, 2017. **12**: p. 153-186.
129. Feng, M., et al., *Individualized Adaptive Stereotactic Body Radiotherapy for Liver Tumors in Patients at High Risk for Liver Damage: A Phase 2 Clinical Trial.* JAMA Oncol, 2017.
130. Kim, M.N., et al., *Increased risk of hepatocellular carcinoma in chronic hepatitis B patients with transient elastography-defined subclinical cirrhosis.* Hepatology, 2015. **61**(6): p. 1851-1859.
131. Luna, A., et al., *A.Overview of Functional Imaging Techniques for Liver Malignancies in Current Clinical Practice or in a Very Near Future*, in *Functional Imaging in Oncology*. 2014, Springer: Berlin, Heidelberg.
132. Li, B., et al., *Use of magnetic resonance elastography for assessing liver functional reserve: A clinical study.* World Journal of Gastroenterology, 2015. **21**(24): p. 7522-7528.
133. Sandrasegaran, K., *Functional MR imaging of the abdomen.* Radiol Clin North Am, 2014. **52**(4): p. 883-903.
134. Pepin, K.M., et al., *MR elastography derived shear stiffness--a new imaging biomarker for the assessment of early tumor response to chemotherapy.* Magn Reson Med, 2014. **71**(5): p. 1834-40.
135. Venkatesh, S.K., et al., *Non-invasive detection of liver fibrosis: MR imaging features vs. MR elastography.* Abdom Imaging, 2015. **40**(4): p. 766-75.
136. Mutic, S. and J.F. Dempsey, *The ViewRay system: magnetic resonance-guided and controlled radiotherapy.* Semin Radiat Oncol, 2014. **24**(3): p. 196-9.
137. Wojcieszynski, A.P., et al., *Gadoxetate for direct tumor therapy and tracking with real-time MRI-guided stereotactic body radiation therapy of the liver.* Radiother Oncol, 2016. **118**(2): p. 416-8.
138. Wu, Q.J., et al., *The impact of respiratory motion and treatment technique on stereotactic body radiation therapy for liver cancer.* Med Phys, 2008. **35**(4): p. 1440-51.
139. Nava, A., et al., *In vivo mechanical characterization of human liver.* Med Image Anal, 2008. **12**(2): p. 203-16.
140. Velec, M., et al., *Impact and Implementation Guidelines for Liver SBRT Delivery with Deformable Registration and Dose Accumulation.* International Journal of Radiation Oncology Biology Physics, 2011. **81**(2): p. S766-S767.
141. Penney, G.P., et al., *A comparison of similarity measures for use in 2-D-3-D medical image registration.* Ieee Transactions on Medical Imaging, 1998. **17**(4): p. 586-595.
142. Schefter, T.E., et al., *A phase I trial of stereotactic body radiation therapy (SBRT) for liver metastases.* Int J Radiat Oncol Biol Phys, 2005. **62**(5): p. 1371-8.
143. Zeng, J.Y., et al., *Dynamic Changes in Liver Stiffness Measured by Transient Elastography Predict Clinical Outcomes Among Patients With Chronic Hepatitis B.* Journal of Ultrasound in Medicine, 2017. **36**(2): p. 261-268.
144. Singh, S., et al., *Diagnostic performance of magnetic resonance elastography in staging liver fibrosis: a systematic review and meta-analysis of individual participant data.* Clin Gastroenterol Hepatol, 2015. **13**(3): p. 440-451 e6.

145. Asia Pacific, C.R.G., *Global Initiative for Chronic Obstructive Lung Disease strategy for the diagnosis, management and prevention of chronic obstructive pulmonary disease: an Asia-Pacific perspective.* Respirology, 2005. **10**(1): p. 9-17.
146. Jogi, J., et al., *Ventilation/perfusion SPECT in chronic obstructive pulmonary disease: an evaluation by reference to symptoms, spirometric lung function and emphysema, as assessed with HRCT.* Eur J Nucl Med Mol Imaging, 2011. **38**(7): p. 1344-52.
147. Barker, B.L. and C.E. Brightling, *Phenotyping the heterogeneity of chronic obstructive pulmonary disease.* Clin Sci (Lond), 2013. **124**(6): p. 371-87.
148. Bhatt, S.P., et al., *CT-derived Biomechanical Metrics Improve Agreement Between Spirometry and Emphysema.* Academic Radiology, 2016. **23**(10): p. 1255-1263.
149. Duman, I.E., et al., *Parenchymal density changes in acute pulmonary embolism: Can quantitative CT be a diagnostic tool? A preliminary study.* Clinical Imaging, 2017. **41**: p. 157-163.
150. Kirby, M., et al., *COPD: Do Imaging Measurements of Emphysema and Airway Disease Explain Symptoms and Exercise Capacity?* Radiology, 2015. **277**(3): p. 872-880.
151. Wielputz, M.O., et al., *Variation of Densitometry on Computed Tomography in COPD - Influence of Different Software Tools.* Plos One, 2014. **9**(11).
152. Cotes, J.E., D.J. Chinn, and M.R. Miller, *Lung function : physiology, measurement and application in medicine*. 6th ed. 2006, Malden, Mass. ; Oxford: Blackwell Pub. xi, 636 p.
153. Ionescu, C., E. Derom, and R. De Keyser, *Assessment of respiratory mechanical properties with constant-phase models in healthy and COPD lungs.* Comput Methods Programs Biomed, 2010. **97**(1): p. 78-85.
154. Macnee, W., *Pathogenesis of chronic obstructive pulmonary disease.* Clin Chest Med, 2007. **28**(3): p. 479-513, v.
155. Marinelli, J.P., et al., *Quantitative assessment of lung stiffness in patients with interstitial lung disease using MR elastography.* J Magn Reson Imaging, 2017.
156. Pepin, K.M., R.L. Ehman, and K.P. McGee, *Magnetic resonance elastography (MRE) in cancer: Technique, analysis, and applications.* Prog Nucl Magn Reson Spectrosc, 2015. **90-91**: p. 32-48.
157. Weiss, E., et al., *Tumor and normal tissue motion in the thorax during respiration: Analysis of volumetric and positional variations using 4D CT.* Int J Radiat Oncol Biol Phys, 2007. **67**(1): p. 296-307.
158. Gao, L., et al., *Imaging of the elastic properties of tissue--a review.* Ultrasound Med Biol, 1996. **22**(8): p. 959-77.
159. Hering, T., *[Update of the GOLD-recommendations - new strategy in diagnostics and therapy of COPD].* MMW Fortschr Med, 2017. **159**(5): p. 53-54.
160. Wang, J., F. Li, and Q. Li, *Automated segmentation of lungs with severe interstitial lung disease in CT.* Med Phys, 2009. **36**(10): p. 4592-9.
161. Papaioannou, M., et al., *COPD assessment test: a simple tool to evaluate disease severity and response to treatment.* COPD, 2014. **11**(5): p. 489-95.
162. Camiciottoli, G., et al., *Prevalence and correlates of pulmonary emphysema in smokers and former smokers. A densitometric study of participants in the ITALUNG trial.* Eur Radiol, 2009. **19**(1): p. 58-66.
163. Gevenois, P.A., et al., *Pulmonary emphysema: quantitative CT during expiration.* Radiology, 1996. **199**(3): p. 825-9.

164. Kauczor, H.U., et al., *CT attenuation of paired HRCT scans obtained at full inspiratory/expiratory position: comparison with pulmonary function tests.* Eur Radiol, 2002. **12**(11): p. 2757-63.
165. Agusti, A.G., *Systemic effects of chronic obstructive pulmonary disease.* Proc Am Thorac Soc, 2005. **2**(4): p. 367-70; discussion 371-2.
166. Siegel, R.L., K.D. Miller, and A. Jemal, *Cancer statistics, 2016.* CA Cancer J Clin, 2016. **66**(1): p. 7-30.
167. Inoue, T., H. Shiomi, and R.J. Oh, *Stereotactic body radiotherapy for Stage I lung cancer with chronic obstructive pulmonary disease: special reference to survival and radiation-induced pneumonitis.* J Radiat Res, 2015. **56**(4): p. 727-34.
168. Proklou A., D.E., Pediaditis E., Kondili E., *Radiation Therapy: Impact on Lung Function and Acute Respiratory Failure*, in *Mechanical Ventilation in Critically Ill Cancer Patients*, P.S. Esquinas A., SOUBANI A., Editor. 2018, Springer.
169. Zhuang, H., et al., *Preliminary analysis of the risk factors for radiation pneumonitis in patients with non-small-cell lung cancer treated with concurrent erlotinib and thoracic radiotherapy.* Onco Targets Ther, 2014. **7**: p. 807-13.
170. Kimura, T., et al., *Combined Ventilation and Perfusion Imaging Correlates With the Dosimetric Parameters of Radiation Pneumonitis in Radiation Therapy Planning for Lung Cancer.* Int J Radiat Oncol Biol Phys, 2015. **93**(4): p. 778-87.
171. Faught, A.M., et al., *Evaluating the Toxicity Reduction With Computed Tomographic Ventilation Functional Avoidance Radiation Therapy.* Int J Radiat Oncol Biol Phys, 2017. **99**(2): p. 325-333.
172. Yamashita, H., et al., *Radiation pneumonitis after stereotactic radiation therapy for lung cancer.* World J Radiol, 2014. **6**(9): p. 708-15.
173. Guckenberger, M., et al., *Dose-response relationship for radiation-induced pneumonitis after pulmonary stereotactic body radiotherapy.* Radiother Oncol, 2010. **97**(1): p. 65-70.
174. Brashier, B. and S. Salvi, *Measuring lung function using sound waves: role of the forced oscillation technique and impulse oscillometry system.* Breathe, 2015. **11**(1): p. 57-65.
175. Setlakwe, E.L., et al., *Airway collagen and elastic fiber content correlates with lung function in equine heaves.* Am J Physiol Lung Cell Mol Physiol, 2014. **307**(3): p. L252-60.
176. Hasse, K., et al., *Estimation and validation of patient-specific high-resolution lung elasticity derived from 4DCT.* Med Phys, 2018. **45**(2): p. 666-677.
177. Hasse, K., et al., *Towards characterizing patient-specific elasticity for imaging assessment of functional lung regions*

. Manuscript submitted for publication.

178. Vinogradskiy, Y., et al., *Regional Lung Function Profiles of Stage I and III Lung Cancer Patients: An Evaluation for Functional Avoidance Radiation Therapy.* International Journal of Radiation Oncology Biology Physics, 2016. **95**(4): p. 1273-1280.
179. Group, R.T.O. *RTOG 0618 Protocol Information*. 2014 [cited 2018.
180. Chang, J.Y., et al., *Stereotactic Ablative Radiotherapy for Centrally Located Early Stage Non-Small-Cell Lung Cancer What We Have Learned.* Journal of Thoracic Oncology, 2015. **10**(4): p. 577-585.
181. Brennan, D., et al., *Clinical validation of 4-dimensional computed tomography ventilation with pulmonary function test data.* Int J Radiat Oncol Biol Phys, 2015. **92**(2): p. 423-9.
182. McKenney, S.E., et al., *Experimental validation of a method characterizing bow tie filters in CT scanners using a real-time dose probe.* Med Phys, 2011. **38**(3): p. 1406-15.

183. Punnoose, J., et al., *Technical Note: spektr 3.0-A computational tool for x-ray spectrum modeling and analysis.* Med Phys, 2016. **43**(8): p. 4711.
184. Boedeker, K.L., V.N. Cooper, and M.F. McNitt-Gray, *Application of the noise power spectrum in modern diagnostic MDCT: part I. Measurement of noise power spectra and noise equivalent quanta.* Phys Med Biol, 2007. **52**(14): p. 4027-46.
185. Friedman, S.N., et al., *A simple approach to measure computed tomography (CT) modulation transfer function (MTF) and noise-power spectrum (NPS) using the American College of Radiology (ACR) accreditation phantom.* Med Phys, 2013. **40**(5): p. 051907.